5-2020

LED Selection for Spectral (Multispectral) Imaging

Jenibel N. Paray
np5956@rit.edu

RIT

Program of Color Science

Munsell Color Science Laboratory

College of Science

Rochester, NY

LED SELECTION FOR SPECTRAL (MULTISPECTRAL) IMAGING

By

Jenibel N. Paray

May 2020

A Thesis Submitted in

Partial Fulfillment of the Requirements for the

Degree of Master of Science in Color Science

Signature of Author _____

Accepted by _____

Dr. Mark Fairchild, Graduate Program Director Date

RIT

Program of Color Science

Munsell Color Science Laboratory

College of Science

Rochester, NY

CERTIFICATE OF APPROVAL

MASTER'S DEGREE THESIS

The Master's Degree Thesis of Jenibel N. Paray

Has been examined and approved by the

Committee as satisfactory for the

Thesis required for the

Master's degree in Color Science

Dr. Roy S. Berns, Advisor

Dr. Mark D. Fairchild, Faculty Member

Date

THESIS RELEASE PERMISSION

ROCHESTER INSTITUTE OF TECHNOLOGY

PROGRAM OF COLOR SCIENCE

Title of Thesis:

LED Selection for Spectral (Multispectral) Imaging

I, Jenibel N. Paray, hereby grant permission to Wallace Memorial Library of R.I.T. to reproduce my thesis in whole or in part. Any reproduction will not be for commercial use or profit.

Signature_____

Date

Abstract

Research was performed to design an LED-based spectral imaging system having channels, commonly referred to as a multispectral imaging system. The first part tackled the evaluation of a camera model in predicting the signals of a 10 LED LEDmotive Technologies Spectra Tunelab coupled with a Finger Lakes Instrumentation panchromatic camera. The camera model was shown to be valid and effective in predicting the camera signal taking into account the color transformation noise. The second part involved the computational selection of 10 LEDs in order to determine the optimum combination for a custom Spectra Tunelab. The computational selection used the spectral data provided by the manufacturer for their 37 available LEDs. The LEDs were grouped according to a specified wavelength range. The binning process helped in decreasing the computational cost and time; the possible combinations were reduced to 110,592 from the initial calculated value of 348,330,136 possible combinations. The combinations were further reduced to 1000 according to spectral reflectance Root-Mean-Square-Error (RMSE). The Euclidean and score ranking methods were then used to evaluate color transformation noise, spectral error and colorimetric accuracy. Goodness of Fit Coefficient and Throughput were calculated as well to further evaluate the combinations. A compromise among the values were reached to identify the best possible LED combination. The optimal combination has peak wavelengths at 390 nm, 450 nm, 475 nm, 505 nm, 540 nm, 550 nm, 590 nm, 620 nm, 660 nm, and 745 nm. All the LEDs were narrow band except the LED with its peak wavelength at 550 nm. This particular LED was similar to the human visual system's luminous efficiency function. Its inclusion was important for colorimetric accuracy and small color transformation noise. When evaluating a large color-gamut target made using commonly used commercial pigments and several artist pigments, the following quality metrics were achieved: average ΔE_{00} of 0.12, total Noise, *N* of 3.35, a lightness noise (ΔL) of 1.22, spectral reflectance RMSE of 6.4 $x10^{-3}$, GFC of 0.97 and a total throughput of 646.85.

Acknowledgements

First and foremost, I praise God and his unfathomable power, for blessing me with skills and resources to proceed successfully. This thesis appears in its current form due to the assistance and guidance of several people. I would therefore like to offer my sincere thanks to all of them.

To my adviser, Dr. Roy Berns, for his patience and guidance in this research. It's a great honor to have him as my adviser and professor. His knowledge and expertise in the Color Science industry is beyond anyone I know. It's indeed a great opportunity to be able to work with him before he retired.

To the rest of the professors and staff in the Munsell Color Science Laboratory, Dr. Mark Fairchild, Dr. Susan Farnand, Dr. Michael Murdoch, Dr. Dave Wyble, Dr. Elena Fedorovskaya and Mrs. Valerie Helmink for sharing their knowledge and helping me all throughout the program.

To all my friends and classmates in the lab, Yue, Luke and everyone else who made things a lot easier and a lot more fun.

To the friends I made in Rochester, Courtney, Natasha and Joe whose company and friendship helped me adjust in the US.

To my previous professors in De La Salle University, Dr. Romeric Pobre and Brother Joseph Scheiter, for their constant advise and encouragements.

To all my friends back in the Philippines, Red, Regine, Ric and everyone else for their moral support and lasting friendship.

To my Filipino friends here in the US, Jennifer, Alexis, Jessica, Celeste and Lorie who kept in touch and kept me sane all throughout my graduate studies here.

To Matt, for always being there, for his love and support.

And of course, my long list would not be complete without thanking my family. To my dearest parents, Blaise and Juniel and to my sister, Aletha, my brother-in-law, Leo and my nephews, Julian and Bran for their unwavering love and support.

Table of Contents

List of Figures

Appendix:

List of Tables

Appendix:

Chapter 1: Introduction

Imaging as a function of wavelength is defined as spectral imaging or imaging spectroscopy. Multispectral and hyperspectral imaging are more popular terms although ambiguous. This thesis is concerned with designing an LED-based spectral imaging system with 10 channels. The cultural heritage imaging community would define this as a multispectral system. Accordingly, this term is used throughout the thesis.

The use multispectral imaging systems in cultural heritage conservation had been shown to be effective in art reproduction (Imai, F. H., Rosen, M. R., & Berns, R. S., 2001), pigment identification (Abed, F. M., 2014), pigment mapping (Zhao, Y., Berns, R. S., Taplin, L. A., & Coddington, J. , 2008), digital restoration (Easton, R. L., Christens-Barry, W. A., & Knox, K. T., 2011) etc. Renowned museums such as the Getty Conservation Institute and the Smithsonian Museum Conservation Institute have dedicated imaging departments working on multispectral imaging research for imaging of artworks and artifacts (Wong, L. and Trentelman, K., 2017; Multispectral and Hyperspectral Imaging, n.d.). The Munsell Color Science Laboratory (MCSL) and the Chester F. Carlson Center for Imaging Science Department at Rochester Institute of Technology have established research programs in multispectral imaging. A notable one from MCSL involves the development of the dual RGB system which was used in the pigment mapping of Vincent van Gogh's *The Starry Night* (Zhao, Y., Berns, R. S., Taplin, L. A., & Coddington, J. , 2008). The camera used an RGB sensor and two sequential absorption filters. A second system developed at MCSL used a panchromatic sensor and seven sequential absorption filters (Burns, P. D. and Berns, R. S. , 1996; Burns, Peter, 1997; Berns, 2018; Wang, Y., & Berns, R. S. , 2017; Wang, 2016). (A review of multispectral literature is presented in Chapter 2.)

This thesis describes research to specify a third MCSL multispectral imaging system where colored LEDs replace absorption filters (Berns, R. S., 2019). LED illuminators work best for historic and light sensitive artifacts such as fragile manuscripts or old paintings because they generate light by electronic transitions instead of thermal interactions. This process gives off little to no heat to the illuminated object (Easton, R. L., Christens-Barry, W. A., & Knox, K. T., 2011). LEDs have several advantages over other illuminants such as good energy efficiency, long life span, durability, cold temperature operation, no IR or UV emissions and wide scopes of options available in the market (8 Advantages of LED Lighting, n.d.).

The Norwegian Colour and Visual Computing Laboratory at Norwegian University of Science and Technology had previously researched the development and use of LEDs in multispectral imaging system led by Dr. Raju Shrestha and Dr. Jon Yngve Hardeberg. Their work includes LED based multispectral film scanner for film digitization (Shrestha, R., Hardeberg, J. Y., & Boust, C., 2012), identifying the factors influencing a LED based multispectral imaging system (Shrestha, R., & Hardeberg, J. Y. , 2013; Shrestha, R., & Hardeberg, J. Y. , 2014), LED matrix design for multispectral imaging system (Shrestha, R., & Hardeberg, J. Y., 2013) and the comparison of LED based multispectral imaging system against a filter based multispectral imaging system and a hyperspectral imaging system (Shrestha, R., & Hardeberg, J. Y., 2018). The said works helped in pinpointing the metrics (ΔE_{00}, Goodness of Fit Coefficient and Root mean square error) to be used in evaluating the colorimetric and spectral accuracy in the LED-based multispectral imaging system proposed in this thesis. Furthermore, they showed that the LED-based multispectral imaging system composed of six LEDs performed better than a filter-based multispectral imaging system and was as good as the hyperspectral imaging system (Shrestha, R., & Hardeberg, J. Y., 2018). Of course, the quality and performance of the filter-based spectral imaging system used in (Shrestha, R., & Hardeberg, J. Y., 2018) can be improved by increasing the number of channels and the use of a more refined camera.

The thesis is subdivided into two sections. The first part involved the evaluation of a camera model in predicting the signals of a LED illumination system coupled with a panchromatic camera. The 10 LEDs were chosen by the manufacturing company with the goal of well simulating conventional lighting. The second part dealt with the computational selection of LEDs using the spectral data from the 37 LED lights available from the manufacturer. The computational selection performed an imaging simulation in order to determine the best LED set composed of 10 LEDs. The optimal set can be used to specify a custom Spectra Tunelab source. The Euclidean method and Score ranking method were used in order to determine the best LED combination. Imai et. al (2002) showed that no metric is superior over others and so it was recommended to use a combination of metrics in order to gain the advantage of each metric (Imai, F.H.; Rosen, M.R.; Berns, R.S., 2002). The ideal combination would yield good colorimetric accuracy, good spectral accuracy and low image noise. Future works involves the purchase of the LEDs chosen from the computational selection to build the LED-based multispectral imaging system and comparison of the results from the computational imaging simulation to the actual imaging experimentation.

Chapter 2: Review of Related Literature

2. Multispectral Imaging System

A multispectral imaging system captures data within the specified region of interest across the electromagnetic spectrum. The multispectral image produced is usually created with multiple bands of wavelengths collected using narrow-band LED illumination or colored filters placed between the object and the sensor (Berns, R. S., 2019). Each channel yields spectral information that is uniquely present only in the specified wavelength region. For example, a certain pigment in an artwork cannot be detected in the visible spectrum but can be detected in the infrared region. As such, increasing the number of channels yields more spectral information (Wang, Y., & Berns, R. S. , 2017; Dickinson, C. , 2001). Bear in mind that creating such systems increases cost and complexity. Berns (2005) discussed a trade-off between spectral accuracy, colorimetric accuracy, cost, and hardware and software complexity. Most multispectral imaging systems use monochrome cameras. An ideal multispectral imaging system would have good colorimetric accuracy, good spectral accuracy, and low image noise (Berns, Roy S., 2005).

A schematic representation of a multispectral imaging system and a multispectral image is shown in Figure 1. Figure 1a shows a filter-based multispectral imaging system, showing a filter wheel in front of a camera. In a LED-based multispectral imaging system, the filter-wheel is removed, and LED illuminants are used. Figure 1b shows the multispectral data cube containing multiple channels.

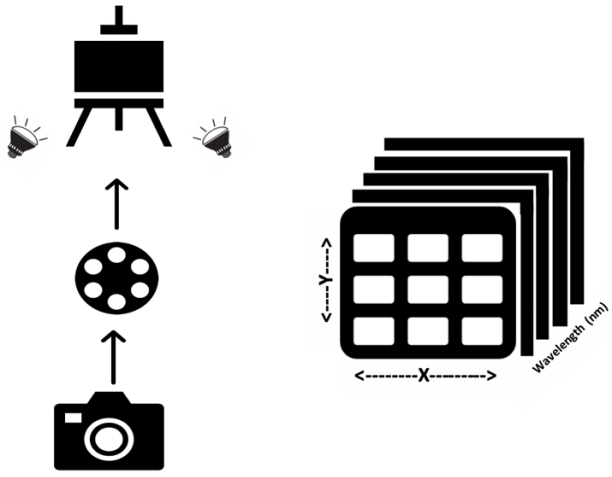

Figure 1. (a) Multispectral imaging system using filters and (b) multispectral image cube.

2.1. Applications in Cultural Heritage Conservation

Multispectral imaging has significant applications in military, medicine, remote sensing and cultural heritage conservation (Coffey, Valerie C., 2012). This thesis focuses on the application of multispectral imaging in cultural heritage conservation. Some application of multispectral imaging in cultural heritage conservation includes pigment identification (Zhao, Y., Berns, R. S., Taplin, L. A., & Coddington, J. , 2008), spectral based color-reproduction of artwork (Berns, R. S., Imai, F. H., Burns, P. D., & Tzeng, D. Y., 1998; Imai, F. H., Rosen, M. R., & Berns, R. S., 2001) and reconstruction of ancient manuscripts (Hansen, D. Michael, 2006). The Munsell Color Science Laboratory and the Chester F. Carlson Center for Imaging Science at Rochester Institute of Technology have established research programs in the development of multispectral imaging in cultural heritage conservation. Past and current on-going research are described below.

2.1.1. The Development of Multispectral Imaging at the Munsell Color Science Laboratory

A spectral-based color reproduction system using multispectral imaging was developed at the Rochester Institute of Technology-Munsell Color Science Laboratory around 1998 by Dr. Roy Berns and Dr. Francisco Imai (Berns, R. S., Imai, F. H., Burns, P. D., & Tzeng, D. Y., 1998). In 2001, the effectiveness of multi-channel visible-spectrum imaging was demonstrated in creating the least metameric reproduction of a van Gogh target with reasonable colorimetric and spectral accuracy. The researchers made use of two approaches in capturing the images. A wide-band capture approach was applied using a conventional camera and Kodak Wratten filters. This showed a less satisfactory result than a narrow-band approach using a liquid crystal tunable filter (LCTF). Imai et. al (2000) published a comparison of two imaging techniques. The wide-band is less time consuming and more applicable to colorants having wide-band spectral features while narrow-band does not require prior knowledge of the colorants used in the artwork and registration and calibration artifacts are not an issue (Imai, F. H., Rosen, M. R., & Berns, R. S., 2001; Imai, F. H., Rosen, M. R., & Berns, R. S., 2000). A collection of pigments researched to be in the actual van Gogh Self-portrait painting was used in the creation of the target. The effectiveness was evaluated by comparing the estimated spectral reflectance derived from the eigenvector analysis against the measured spectral reflectance from a spectrophotometer. The reflectance spectra of the printed reproduction of the van Gogh target was measured and compared to the measured reflectance of

the target in order to evaluate the accuracy of the spectral-based printing system. For colorimetric accuracy, the system showed a ΔE^*_{94} of 5.0 and for spectral accuracy, a 3.1% RMSE (Imai, F. H., Rosen, M. R., & Berns, R. S., 2001).

Another notable example of the application of multispectral imaging in the field of cultural heritage conservation was the pigment mapping of Vincent van Gogh's *The Starry Night*. Zhao et. al (2008) made use of the dual RGB system developed in the Munsell Color Science Laboratory. A Color-Filter-Array (CFA) camera combined with two optimized filters was used to capture the two RGB images assembled to a six-channel spectral image. The two green channels are nearly identical thus only five channels are used for spectral reconstruction. To preserve high colorimetric accuracy, a spectral reconstruction method that combines spectral and colorimetric transformations was used together with the system to retrieve pixel by pixel spectral reflectance factor (Wang, Y., & Berns, R. S. , 2017; Zhao, Y., Berns, R. S., Taplin, L. A., & Coddington, J. , 2008; Berns, R., Taplin, L., & Nezamabadi, M., 2005; Berns, R., Taplin, L., & Nezamabadi, M., 2004). The same calibration target used in Imai et. al (2001) was used in pigment mapping of Vincent van Gogh's *The Starry Night.* A calibration target is needed in order to use the method which in the case of pigment mapping of Vincent van Gogh's The Starry Night was readily available from the past publication (see (Imai, F. H., Rosen, M. R., & Berns, R. S., 2001)). The Matrix R method was used in the pigment mapping as well, it is a type of learning-based reconstruction developed through Wyszecki's hypothesis and Cohen and Kappauf's Matrix R theory (Zhao, Y., & Berns, R. S., 2007). Matrix R theory is a spectral decomposition derived from Wyszecki's hypothesis that a ''fundamental stimulus'' and a ''metameric black'' can be derived from decomposing a "color stimulus" into two spectra (Wyszecki, G. , 1953).

In addition to the Matrix R method, Kubelka-Munk (K-M) theory was applied to map the pigments in van Gogh's *The Starry Night.* K-M theory was used to predict the spectral reflectance of the pigment mixture using the individual measured reflectance of the pigments used to create the mixture (Berns, R. S., 2019; Abed, F. M., 2014; Walowit, E., Mccarthy, C. J., & Berns, R. S. , 1987). Each pixel is matched with the most probable pixel based on the predicated values from the K-M calculations. The map is then created from the accumulated matched pigments.

In summary, the effectiveness of the pigment mapping technique depends on the prior knowledge of the artist's palette. However, the availability of a universal target works as well for

deriving the eigenvectors needed to estimate the spectra (Imai, F. H., & Berns, R. S., 2002). The study was able to map-out seven out of 10 paints from the artist's palette.

Some more current research at MCSL for multispectral imaging in cultural heritage conservation involves digital reproduction of artwork via a computer graphics rendering tool combined with a modified photometric stereo technique (Cox, B. D., & Berns, R. S., 2015), imaging using an affordable single, commercially available mirrorless digital camera (Kuzio, O., & Berns, R. S., 2019) and now the development of an LED-based multispectral imaging, the subject of this thesis.

2.1.2 Multispectral Imaging of Archimedes Palimpsest at Chester F. Carlson Center for Imaging Science

Research regarding multispectral imaging of Archimedes palimpsest at Chester F. Carlson Center for Imaging Science had been on-going since 2000. The goal of the research is to recover Archimedes' original written text that was erased and overwritten with the *Euchologion* (a Christian prayer book). Such a document is known as a palimpsest. In addition to the overwriting done by 13th century Christian monks, forged pictures were also added that hid more of its written texts. Improper handling and storage led to the further degradation of the pages of the palimpsest making its text more undiscernible. The palimpsest provides an insight into Archimedes' works and the progress of mathematics and physics in 3rd century BCE. The Archimedes Palimpsest contains seven treatises of Archimedes. These are, *"On the Equilibrium of Planes", "Spiral Lines", "Measurement of a Circle", "On the Sphere and Cylinder", "On Floating Bodies", "The Method of Mechanical Theorems"* and *"Stomachion",* all of which proves how Archimedes was way ahead of his time (The Archimedes Palimpsest, n.d.; Netz R., and Noel W., 2007.).

Several imaging techniques were tried in order to meet the goal. Initial imaging involved the use of least-squares spectral unmixing, where the components of the images were categorized into overwriting, underwriting, parchment and mold. The images were captured using a 12-bit scientific camera coupled with five glass filters transmitting light from ultraviolet to infrared region with widths of 100 nm. In addition to, three illuminants were used (visible light, shortwave ultraviolet lamps and longwave ultraviolet lamps). This subsequently produced 15 spectral images processed using the least-squares spectral algorithm. This was done to strip off the prayer book and reveal the undertext palimpsest. The technique was successful in stripping off much of the ink

from the prayer book however it also removed some underwriting that were overlaid by the inks from the prayer book leaving gaps making the palimpsest more unreadable (Easton, R., & Knox, K., 2004; Walvoord, D. J., & Easton, R. L., 2008; Easton, R. L., Christens-Barry, W. A., & Knox, K. T., 2011; Knox, K. T., Dickinson, C., Wei, L., Easton Jr, R. L., & Johnston, R. H., 2001; Easton, R. L., Christens-Barry, W. A., & Knox, K. T, 2011).

In order to solve this dilemma, the researchers deemed it more appropriate to just retain the overwriting but have it less visible and fainted in the background by increasing the contrast and appearance of the original underwriting. Images of the pages were captured under varying LED illuminants ranging from short wavelength to long wavelength. The LED illumination system called "Eureka Lights" was composed of one waveband ($\lambda \sim 365nm$) in the UV region, seven in visible region ($\lambda\sim$ 445nm, 470nm, 505nm, 530nm, 570nm, 617nm, and 625nm) and three in infrared region ($\lambda \sim$ 700nm, 735nm, and 870nm). It was seen that the underwriting fades more with an increase in wavelength, thus imaging it under ultraviolet illumination was the best choice. The pseudo-color technique was then applied by assigning specific colors for the four categories (overwriting, underwriting, parchment and mold). The resulting image showed a red text for the underwriting and a neutral gray or black for the unwanted text. This contrast helped the scholars in deciphering the texts in the intact portions of the palimpsest, however the moldy sections and the degraded pages are still problematic (Hansen, D. Michael, 2006; Walvoord, D. J., & Easton, R. L., 2008; Easton, R. L., Christens-Barry, W. A., & Knox, K. T., 2011; Knox, K. T., Dickinson, C., Wei, L., Easton Jr, R. L., & Johnston, R. H., 2001; Knox, K. T., 2008).

For the degraded and moldy portion of the palimpsest, the researches made use of a character recognition method. This method makes use of a training library built from the transcribed portions of the palimpsest. The method yields a list of probable words that matches the character fragment and then are further evaluated by the scholar to see if the word makes coherent sense in the palimpsest (Walvoord, D. J., & Easton, R. L., 2008; Easton, R. L., Christens-Barry, W. A., & Knox, K. T., 2011; Walvoord, D. J. , 2008). In addition to Perry et. al (2018) implemented the use of two-dimensional flattening on damaged and distorted documents (Peery, T. R., & Messinger, D., 2018). The research aimed to develop and enhance the training technique in order to be applied to the damage portions of the palimpsest. The technique aimed to digitally unravel or flatten warped objects such as scrolls damaged by fire, water or other force of nature. The study showed that flattening in sections then assembling these images rather than doing the whole

document yielded better results. Furthermore, although the flat to sharp method required fewer steps, the method yielded less spectral error (Peery, T. R., & Messinger, D., 2018).

Perry et. al (2018) also published a study comparing the currently available multispectral imaging at the Chester F. Carlson Center for Imaging Science to a hyperspectral imaging system (HSI) available at the University of Rochester in terms of noise. Although hyperspectral imaging systems was seen to have spectral/spatial compromise unlike a multispectral imaging system, a lower quality system would still meet the requirement if the application of the system heavily depends on human vision. An example would be the transcribing of a palimpsest which is done within the limits of the human visual system. A finer higher resolution image beyond what is detectable or needed to read the text is unnecessary (Peery, T. R., & Messinger, D., 2018; Peery, Tyler R., 2019). Furthermore, panchromatic sharpening was seen to be effective in recovering the decrease in spatial resolution compared with hyperspectral imaging (Peery, T. R., & Messinger, D. W. , 2019).

In summary, a variation and a combination of imaging techniques is needed for the different portions of the palimpsest. The condition of the palimpsest and the demands of the scholars who transcribed the texts heavily influenced the imaging technique used.

2.2 LED based-Multispectral Imaging System

This thesis aims to develop a LED-based multispectral imaging system. The use of LEDs instead of filters is another way of doing multispectral imaging. In this approach, an image is captured using a monochrome camera for each LED light. These set of *n* images captured under the set of *n* lights is combined to produce the *n*-channel multispectral image (Park, J.I., Lee M.H., Grossberg M.D.Z.D., and Nayar S.K.).

The rise of the manufacturing industries of LED nowadays lead to the increase in options, availability and cost effectiveness (Shrestha, R., & Hardeberg, J. Y., 2013). LED based multispectral imaging research had been shown to have important application in film digitization (Shrestha, R., Hardeberg, J. Y., & Boust, C., 2012), digital color proof in print reproduction (Yamamoto, S., Tsumura, N., Nakaguchi, T., & Miyake, Y., 2007), cultural heritage conservation (Shrestha, R., & Hardeberg, J. Y. , 2013), and medical imaging (Everdell N. L., Styles I. B., Claridge E., Hebden J. C., and Calcagni A. S. , 2009), among others. Light generated from LEDs apply little to no heat, which is vital in the imaging of fragile historical documents or artworks.

The availability of narrow-band LEDs is also good for spectral image processing (Easton, R. L., Christens-Barry, W. A., & Knox, K. T., 2011). The researchers are particularly interested in the application of multispectral imaging in cultural heritage conservation. Previous studies relating to LED-based multispectral imaging are discussed below.

Shrestha and Hardeberg (2014) determined four major factors that affect the performance of multispectral imaging using LEDs: camera type, demosaicing method, the number of LEDs, and noise. LED based multispectral imaging simulations using a monochrome camera and an RGB camera were performed. The simulation made use of two sets of LED lights: the first set was composed of 19 LED that were previously used in the development of a LED based multispectral film scanner (see (Shrestha, R., Hardeberg, J. Y., & Boust, C., 2012)) and the other set was composed of 6 LEDs from JUST Normlicht LED Color Control light booth. The spectral power distribution (SPD)of the two sets of LEDs are shown in Figure 2. The spectral power distributions of the LEDs were uniformly distributed throughout the visible spectrum. Shrestha and Hardeberg simulated six and nine band systems as what were previously found to be the constrained range of the number of LEDs in this system in their previous research (see (Shrestha, R., Hardeberg, J. Y., & Boust, C., 2012)).

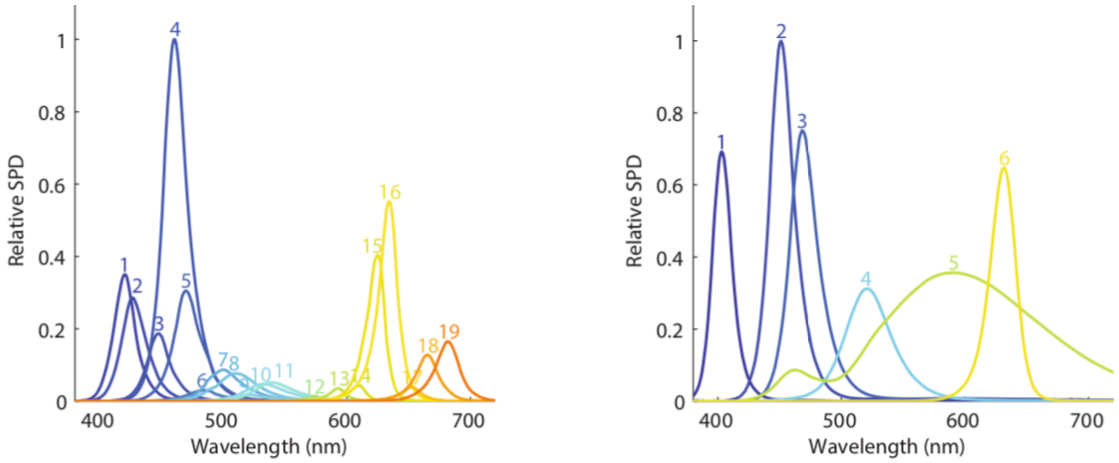

Figure 2. Spectral power distribution of the two sets of LEDs used in Shrestha and Hardeberg (2014).

The results showed that the nine-band system using a monochrome camera performed the best with an RMS error of 0.011 while the two six-band systems using the monochrome camera and the RGB camera performed the same. Noise was investigated as well by introducing a random

gaussian noise of about 0% to 20%. As expected, the amount of noise is directly proportional to the RMS error and also to the increase in the number of LEDs used. Although the RGB camera speeds up the image capturing process, the necessary demosaicing had an impact on the spatial accuracy thus affecting the quality of the images (Shrestha, R., & Hardeberg, J. Y. , 2014; Shrestha, R., & Hardeberg, J. Y., 2013). The use of a monochrome camera combined with a large selection of LEDs covering the range of the electromagnetic spectrum was ultimately recommended (Shrestha, R., & Hardeberg, J. Y. , 2014).

This thesis starts with the computational selection of the LEDs for multispectral imaging. LED selection plays a vital role in constructing and designing a LED-based multispectral imaging system. The number of LEDs corresponds to the number of channels, as such the image quality, spectral accuracy and colorimetric accuracy heavily depends on the number of LEDs and its region of interest in the electromagnetic spectrum. The maximum number of LEDs that can be used in the system is usually restricted by cost and manufacturing limitations (Shrestha, R., Hardeberg, J. Y., & Boust, C., 2012). Previous researches regarding LED selection and filter selection provided valuable insights for the selection process in this research (Shrestha, R., Hardeberg, J. Y., & Boust, C., 2012; Wang, Y., & Berns, R. S. , 2017; Li, S. X., 2018).

Wang et. al (2016) made use of fitting Gaussians method and a traditional subsets selection method in choosing the best filter for wide-band multispectral imaging. Narrow-band was deemed to be unfit for cultural-heritage studio imaging due to its complex image registration, costly customized filters and time-consuming measurements. An imaging simulation was performed using the Schott filter spectral database and the current filters sold by the Andover Corporation. The fitting Gaussian method is a method of choosing seven filters that were the closest to the theoretical Gaussian filters while the traditional selection method involved dividing the LED sets according to their region of interest then running the simulation and sorting according to the computed colorimetric and spectral accuracy. The study showed that fitting Gaussian method was better compared to the traditional selection method utilizing less computational time and better results. The fitting Gaussian method yielded a noise of 1.08, ΔE_{00} of 0.28, RMS of 0.019 in comparison to the selection method who's top 1000 combinations yielded noise of less than 1.60, ΔE_{00} larger than 0.7 and RMS in the range of 0.022-0.024. The researchers then chose the filters via the fitting Gaussian method in building the multispectral imaging system.

Li (2018) had a similar approach to Shrestha et. al (2012) in the use of metrics such as Root mean square error and Goodness of Fit Coefficient (Shrestha, R., Hardeberg, J. Y., & Boust, C., 2012) and made use of the maximum linear independent (MLI) filter selection method. The spectral data of 45 broadband filters (400-700 nm) from Hoya manufacturing was used in the imaging simulation. An optimal filter set is selected via a filter vector analysis. The metrics chosen determined the optimal filter set. The results of the simulation showed that the chosen filter set had five-channels with a uniform peak distribution in its transmittance curves, overlapped transmittance curve with the adjacent filter and a distinct transmittance peak in its first filter.

Based on the study of Imai et. al (2002), there was not a metric that was conclusively superior over others for all purposes. As such it was recommended to use a combination of the metrics in order to gain the advantage of each metric (Imai, F.H.; Rosen, M.R.; Berns, R.S., 2002). The metrics chosen in this thesis are discussed in detail in the following chapters.

Chapter 3: Verifying the Camera Model

Preliminary experiments to verify the camera model and evaluate the currently available LEDs at Munsell Color Science Laboratory (MCSL) are discussed below. The chapter is divided into parts to describe the imaging system composed of 10 LEDs and a monochrome camera and the calculations performed to evaluate the colorimetric and spectral accuracy of the imaging system. The calculation includes the use of the actual camera signal taken from the images and the calculated predicted camera signal.

3.1 Multispectral Imaging Workflow

The workflow for multispectral imaging process is shown in Figure 3. The images captured under each light were flat fielded and registered. (Dark current subtraction was performed automatically in the camera software.) Flat fielding is needed to correct the non-uniformity in the images due to the pixel to pixel gain variation of the sensor, nonuniform lighting and light fall off caused by the lens (Li, S. X., 2018; Kalajian, P. , 2011).

Image registration is needed due to the variation in the camera focus for each LED light. The image registration helped in reducing the difference in magnification and the shift in imaging caused by chromatic aberration. MATLAB's Speeded-Up Robust Features (SURF) registration was used in this thesis (MathWorks, n.d.). SURF is a feature detector algorithm that detects feature-points in an image. These features could be corners, blobs, lines, edges etc. In a study conducted by Tareen and Saleem in 2018 comparing various feature detector algorithms, SURF was seen to detect more features than other algorithms (SIFT, AKAZE, KAZE) (Tareen, S. A. K., & Saleem, Z., 2018). The variation in camera focus in each LED light and the consequent image registration wasn't as big of a challenge in multispectral imaging using LED light compared to multispectral imaging using filters with varying thickness. The Sky X professional software by Software Bisque Inc had automatic focusing function that helped determined the best focus during the imaging. The variation in camera focus value under each LED light ranged from 0-1 %. The chosen reference image was the image taken under the LED whose peak sensitivity was nearest to V(λ). Lastly, the images were evaluated according to image quality, colorimetric accuracy and spectral accuracy.

An illustration of the imaging system is depicted in Figure 4 and the actual set up is shown in Figure 5. The imaging system is composed of a Finger Lakes Instrumentation Microline ML50100 monochrome CCD camera, Rodenstock HR Digaron-S 4.0/100 mm with Copal shutter, and 10 LEDs from LEDmotive Technologies. A more detailed description of the instruments used is provided in the following sections.

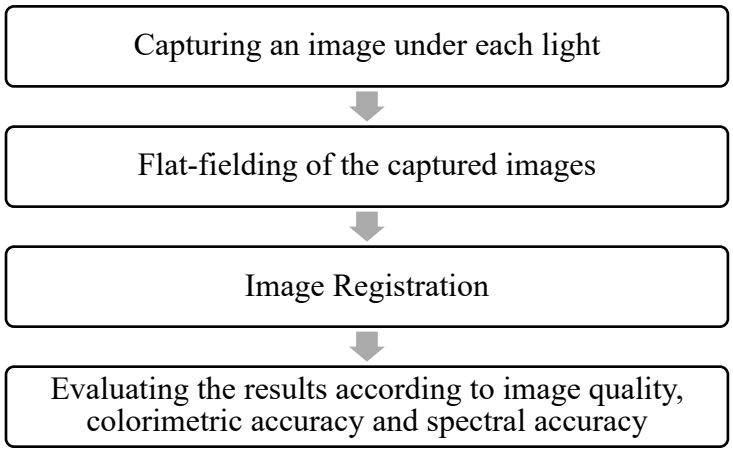

Figure 3. Workflow of multispectral imaging.

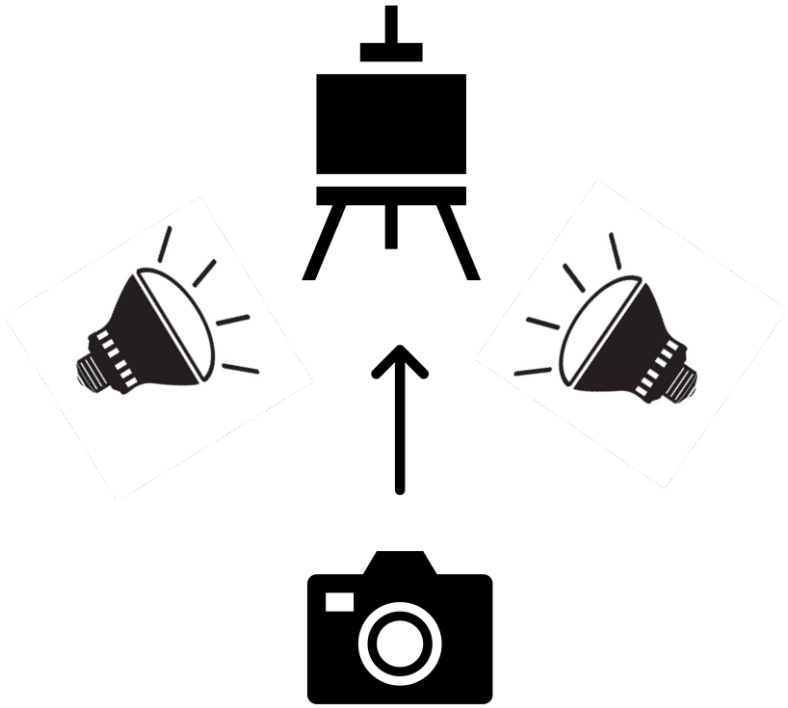

Figure 4. Illustration of the imaging system.

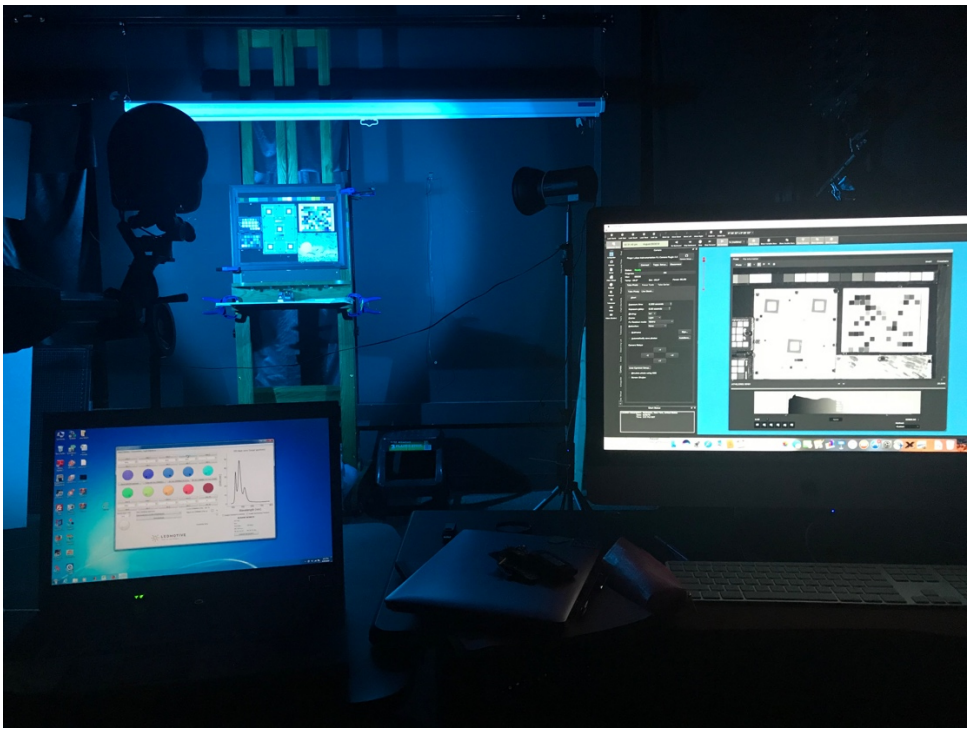

Figure 5. LED-based multispectral imaging at Munsell Color Science Laboratory- Rochester Institute of Technology.

3.2 The Imaging System

The camera sensitivity of a Microline ML50100 monochrome CCD camera manufactured by Finger Lakes Instrumentation with attached lens was measured using a Newport Cornerstone monochromator. The set-up of the camera sensitivity measurement is seen in Figure 6. The measurement was done in a dark room. The Newport Cornerstone monochromator was controlled by MATLAB. The lamp was warmed-up 10 minutes prior to the measurement. The monochromator was adjusted at levels 1-3, (1)330-600 nm, (2)600-800 nm and (3) 800-1100 nm in accordance to the wavelength being measured. The radiance was measured from 400-760 nm with increments of 10 nm using a Photo Research PR-655. The values were then interpolated to produce increments in 1 nm data.

Images at each wavelength were captured taking a great care to make sure the images were not overexposed. Given that the tiff images were too large and takes a large amount of time to load and process, only the values on the chosen certain portion of the image were used in the calculation

(see Figure 7). Furthermore, only the image containing the light is needed, and so selecting a certain portion is an easier and a faster way. There were 204x245 pixels selected. The mean digital counts were then divided by their corresponding radiance. The black background was subtracted automatically by the Sky X professional software.

The Sky X professional software by Software Bisque Inc. was used to control the camera. The software proved to be very useful in providing automatic dark subtraction, camera temperature control and computer-aided focusing.

The camera is a 16-bit 50.1-megapixel camera that operates using a KAF-50100 Image Sensor. The said camera's sensitivity was used in the verification of the camera model and the computational imaging simulation. The camera relative spectral sensitivity of the monochrome camera is shown in Figure 8.

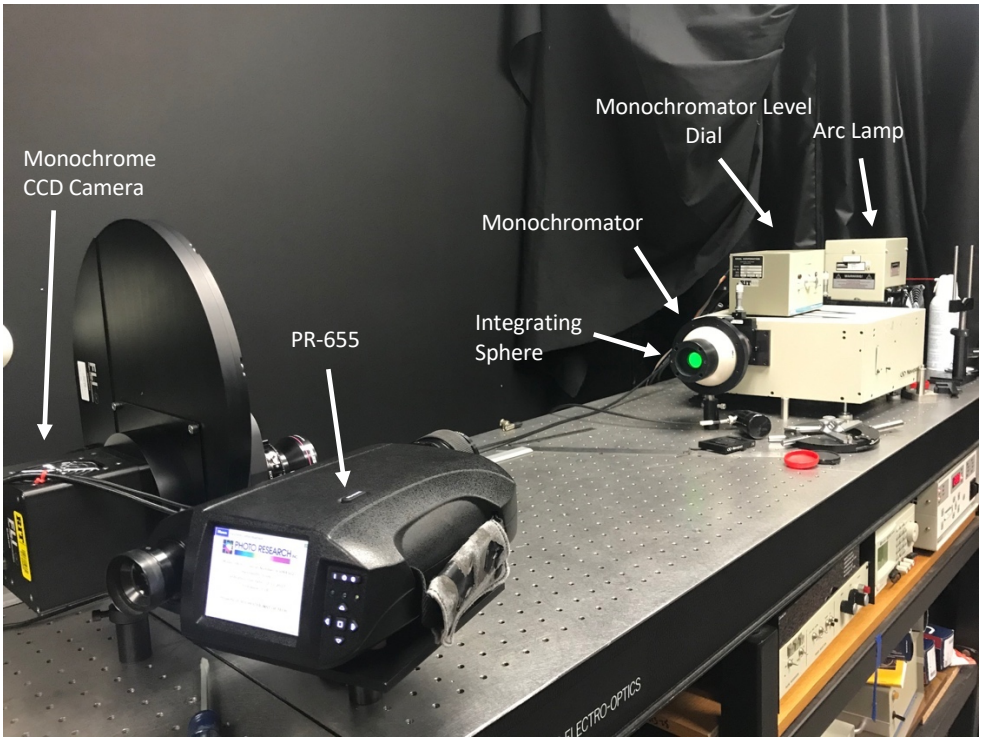

Figure 6. Newport Cornerstone monochromator, Microline ML50100 monochrome CCD camera and Photo Research PR-655 set up. (Disclaimer: The picture was shot in a well-lit room for the sake of clearly showing the set-up; the entirety of the experiment occurred in a dark room).

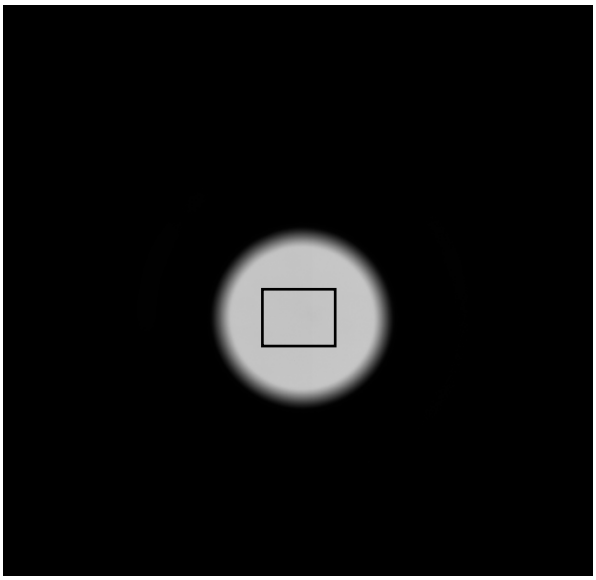

Figure 7. The box in the 540 nm image shows the area for which the values were extracted, 204 by 245 pixels.

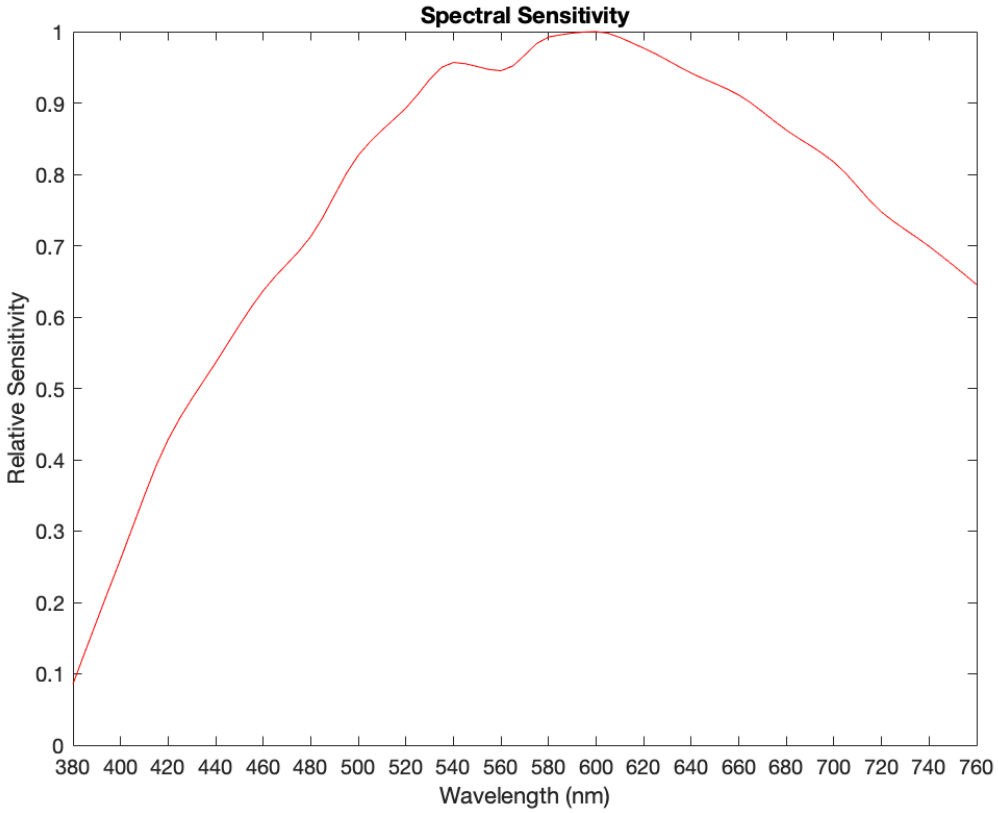

Figure 8. Microline ML50100 camera spectral sensitivity normalized to unity at peak height.

The LED system used in this thesis is made by LEDmotive Technologies (see Figure 9 for the actual model). The spectra tune lab device is composed of 10 LEDs with varying peak

wavelengths from 430-660 nm, specifically 430 nm, 445 nm, 465 nm, 475 nm, 505 nm, 520 nm, 545 nm, 595 nm, 640 nm and 660 nm. The manufacturer's data of the spectral power distribution of the LEDs is shown below in Figure 10. The LEDs were measured again in the lab using Photo Research PR-655, the measured radiance was rescaled and plotted for comparison as shown in Figure 11. The LEDs were embedded within the device and were controlled using the LEDmotive μWAVE software. As of now the software only runs in a Windows OS. The software is capable of delivering either a single monochromatic light or a combination of these lights. The lights require no warm-up time and can be dimmed from 0% - 100% per channel with a resolution depth of 12 bits (4096 steps) (LEDMOTIVE, n.d.). A Godox standard 7" reflector was attached to the front of the light source.

Figure 9. Spectra Tune Lab front and rear view (accessed on March 2020, https://ledmotive.com).

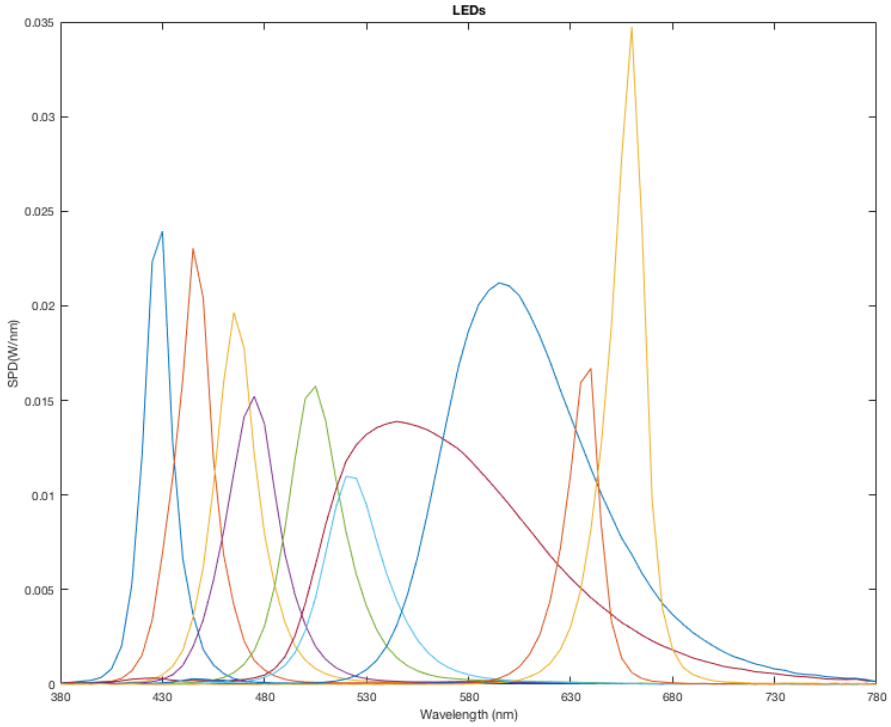

Figure 10. Spectral power distribution of the LEDs from LEDmotive Technologies.

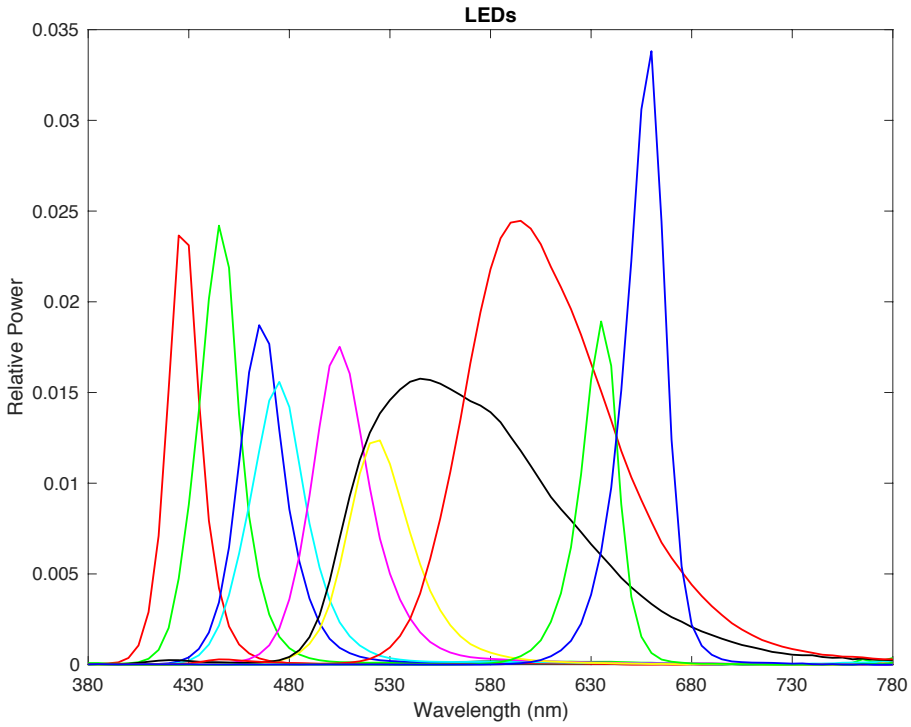

Figure 11. Measured spectral radiance of the LEDs from LEDmotive Technologies.

3.3 The Target

The imaging made use of DT Next Generation Target V2 made by Avian Rochester, L.L.C. It is composed of 130 patches. The target was modified to include pigments such as bone black, lead white, titanium white, ultramarine, cobalt blue and chromium oxide green. The said pigments were popular in artist's palette. For example, lead white is a popular white pigment in old master paintings before it was replaced by titanium white in the 20th century (Fortunato, 2005). Modifying the target to include historical pigments is important in multispectral imaging of paintings. The reflectance of the target was measured using an i1 Pro 2 X-rite spectrophotometer using 45°a/0° geometry as seen in Figure 12.

Figure 12. DT Next Generation Target V2 reflectance measurement.

3.4 Camera Signal

The camera signal represents the measured amount of light from the image, which is the number of electrons captured by the CCD or the number of counts present in the captured image (Clark, R., n.d.). In multispectral imaging, the camera signal is taken as the mean pixel value in the specified area, for which in the case of the Next Generation Target is the area of each patch. As seen in Figure 13 below, around 60% of the patch was used to determine the camera signal. The red asterisk determines the border of the camera signal taken; lines connecting the asterisk forms a rectangle, clearly showing the actual area of the patch.

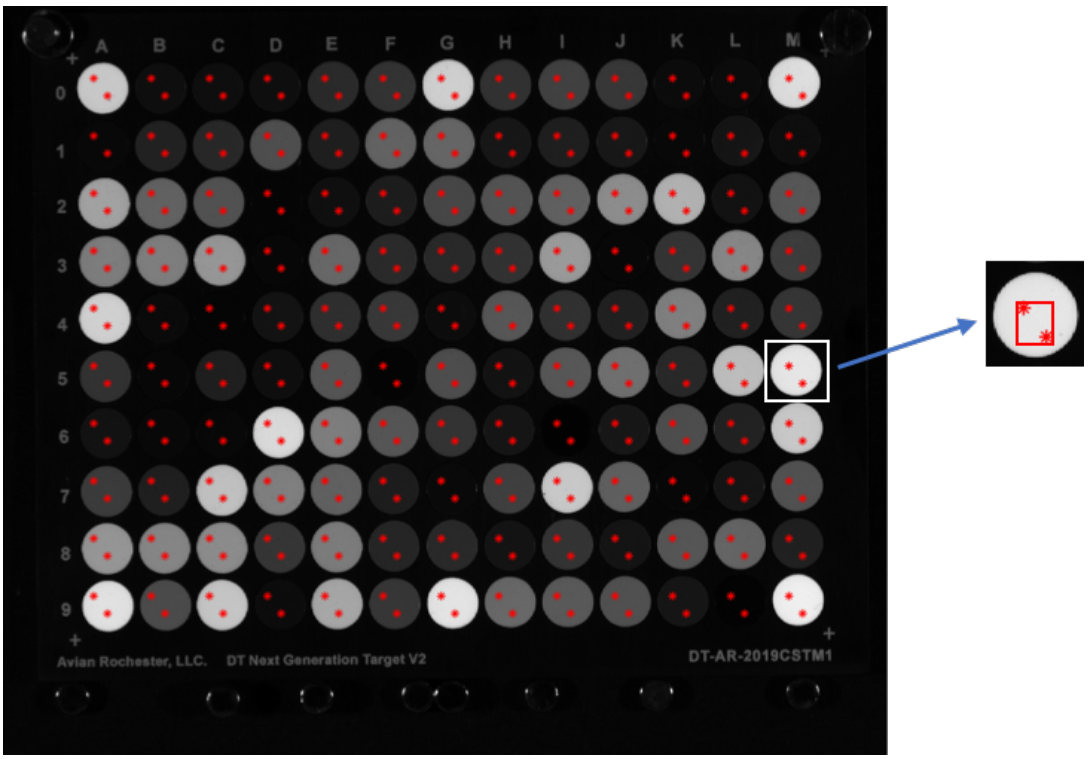

Figure 13. Sample image of a target showing marked areas where camera signals were averaged.

Aside from the data using the captured images, the camera signal was predicted. The camera signal **c** was calculated using the Equation 1 below, where **S** defines the spectral sensitivity of the monochrome camera, **E** represents the LEDs spectral power distribution (SPD) and **R** is the reflectance measurements of the DT Next Generation Target V2.

$$\mathbf{c} = \mathbf{SER} \qquad (1)$$

where

$$\mathbf{S} = \begin{pmatrix} s_{\lambda,1} & \cdots & s_{\lambda,1} \\ \vdots & \cdots & \vdots \\ s_{\lambda,n} & \cdots & s_{\lambda,n} \end{pmatrix},$$

$$\mathbf{E} = \begin{pmatrix} E_{\lambda} & 0 & 0 \\ 0 & \ddots & 0 \\ 0 & 0 & E_{\lambda} \end{pmatrix},$$

$$\mathbf{R} = \begin{pmatrix} R_{\lambda,1} & \cdots & R_{\lambda,i} \\ \vdots & \cdots & \vdots \\ R_{\lambda,1} & \cdots & R_{\lambda,i} \end{pmatrix},$$

The linear relationship of the actual camera signal and the predicted camera signal is shown in Figure 14. Regression analysis showed that the 130 patches follows an excellent linearity with R^2 of 0.99. The linear fit showed a slope of 1.0-1.1 and y-intercepts < 0.01 for the targets (see Table 1 for the calculated slope, R^2 per target and y-intercept). These show that the camera model predicted the camera signals well. The difference between the predicted cameral signal and the actual camera signal from the images are small and unbiased. Unbiased in this context means that the predicted camera signals were found to be in a reasonable range (not too high or too low) around the measured values (Frost, J., n.d.).

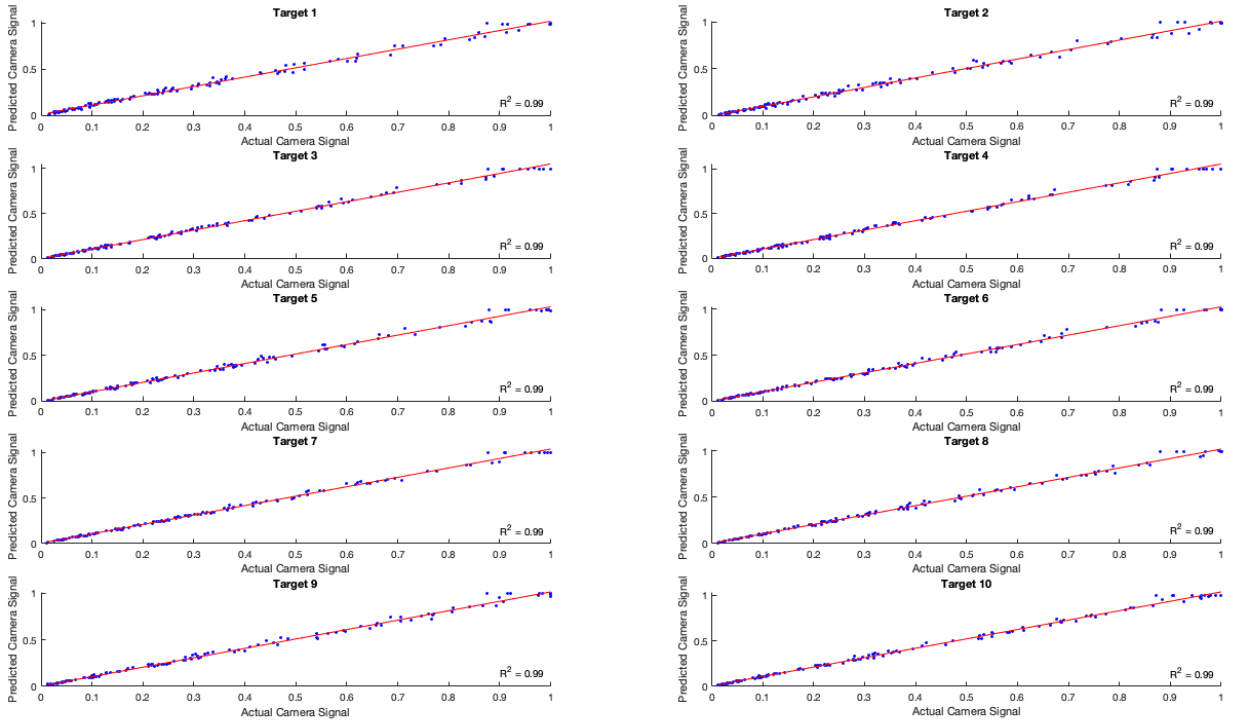

Figure 14. Actual and Predicted Camera Signals.

Table 1. Calculated R^2, slope and y-intercept of the targets.

Target	R^2	Slope	Y-intercept
1	0.99	1.0	1.4×10^{-2}
2	0.99	1.0	-4.5×10^{-4}
3	0.99	1.0	7.5×10^{-4}
4	0.99	1.1	1.0×10^{-3}
5	0.99	1.0	8.0×10^{-4}
6	0.99	1.0	2.6×10^{-3}
7	0.99	1.0	4.5×10^{-3}
8	0.99	1.0	3.6×10^{-3}
9	0.99	1.0	4.3×10^{-3}
10	0.99	1.0	6.2×10^{-3}

The camera signal was then used to predict the spectral reflectance of the patches. Equation 2 below shows the derivation of the spectral reflectance **R** using the spectral transformation matrix $\mathbf{M_S}$ coefficients multiplied to the camera signal **c**. The matrix was derived using Equation 3, as the product of the pseudoinverse (MATLAB *pinv*) of the cameral signal $\mathbf{c}^+$ and the measured spectral reflectance **R** values of the calibration target (Berns, R. S., 2019; Zhao, Y., & Berns, R. S., 2007). Root-mean-square-error (RMSE) was used as the metric for the reflectance spectral accuracy.

.

$$\mathbf{R} = \mathbf{M_S c} \qquad (2)$$

$$\mathbf{M_S} = \mathbf{R c}^+ \qquad (3)$$

The tristimulus values **t** can be computed from the reflectance values **R** using Equation 4 below. The result is the same as the predicted tristimulus values from the camera signal using Equation 5. The **T** represents the color matching functions of the observer, the **S** is the spectral power distribution of the illuminant and **R** is the reflectance values of the target.

$$\mathbf{t} = \mathbf{TSR} \qquad (4)$$

where,

$$\mathbf{S} = \begin{pmatrix} S_\lambda & 0 & 0 \\ 0 & \ddots & 0 \\ 0 & 0 & S_\lambda \end{pmatrix}, \mathbf{T}_{xyz} = \begin{pmatrix} \overline{x}_\lambda & \dots & \overline{x}_\lambda \\ \overline{y}_\lambda & \dots & \overline{y}_\lambda \\ \overline{z}_\lambda & \dots & \overline{z}_\lambda \end{pmatrix}$$

$$\mathbf{t} = \begin{pmatrix} X_1 & \cdots & X_i \\ Y_1 & \cdots & Y_i \\ Z_1 & \cdots & Z_i \end{pmatrix}$$

The camera signal can also be used to predict the tristimulus values of the patches. Equation 5 below shows the derivation of the tristimulus values **t** using the color transformation matrix $\mathbf{M_T}$ coefficients multiplied to the camera signal **c**. The matrix $\mathbf{M_T}$ was derived using Equation 6, as the

product of the pseudoinverse *(pinv)* of the cameral signal $\mathbf{c}^+$ and measured tristimulus values $\mathbf{t}$ of the calibration target (Berns, R. S., 2019; Berns, R., Taplin, L., & Nezamabadi, M., 2005). Estimated tristimulus value are the same using Equations 5 or 6 since the relationship between spectral reflectance and tristimulus values are linear.

$$\mathbf{t} = \mathbf{M}_T\mathbf{c} \qquad (5)$$

$$\mathbf{M}_T = \mathbf{t}\mathbf{c}^+ \qquad (6)$$

CIEDE2000 was used as the metric for colorimetric accuracy with the positional function, S_L, equal to unity (see Equation 7); doing this gives more significance to the lightness noise that is more visible in an image (Berns, R., 2016). Noise represents the uncertainty in the signal (Burns, Peter, 1997). This is usually seen as a variation in lightness or color in the images. Noise is usually brought about by several factors such as exposure shot noise, instrument error due to deterioration of the imaging device or calibration variation, error propagation occurring during the transformation of the image signals, etc. (Burns, P.D., and Berns, R.S., 1997; Burns, P.D., 2002). This thesis discusses the noise due to the color transformation ($\mathbf{M_T}$). Noise can be determined by computing the standard deviation in the chosen area in an image (Noise in photographic images, 2020). It can also be computed using Equation 8 below. Previous researches made by Burns and Berns tackled the color transformation noise produced during multispectral imaging. The use of multivariate error-propagation analysis to color signal transformation proved to be helpful in modelling noise due to color measurement uncertainty in CIELAB path (Burns, P.D., and Berns, R.S., 1997; Burns, P.D., and Berns, R.S., 83-85). Kuniba and Berns followed up with a study on the design of digital camera color filters with high color accuracy and low image noise. The noise parameter, *N*, as shown in Equation 8, was used to evaluate the photon shot noise component among CMY filters and RGB filters. Photon shot noise is the uncertainty in the photon counting at the sensor (Kuniba, H., & Berns, R.S., 2008; Kuniba, H., & Berns, R.S., 2009). A comparison with CMY filters and RGB filters showed that RGB filters performed better in terms of color reproduction and noise despite the CMY's capability to collect more photons. The noise during

the color transformation affected the performance of the CMY filters (Kuniba, H., & Berns, R.S., 2009).

The sum of the rows in the matrix in Equation 8 were rescaled to unity before the calculation. The equation is derived in a gray world idea where captured images assimilate to medium gray. It made use of a gray sample under illuminant E (equal-energy spectrum) and where CIELAB and CIEDE2000 total color differences are the same at L*=50.

$$\Delta E_{00} = \sqrt{\left(\frac{\Delta L'}{k_L S_L}\right)^2 + \left(\frac{\Delta C'}{k_C S_C}\right)^2 + \left(\frac{\Delta H'}{k_H S_H}\right)^2 + R_T\left(\frac{\Delta C'}{k_C S_C}\right)\left(\frac{\Delta H'}{k_H S_H}\right)} \qquad (7)$$

$$N = \sqrt{\left(\Delta L_N^*\right)^2 + \left(\Delta a_N^*\right)^2 + \left(\Delta b_N^*\right)^2} \qquad (8)$$

where,

$$\left(\Delta L_N^*\right)^2 \simeq \left(\frac{116A}{3}\right)^2 \left(a_{2,1}^2 + a_{2,2}^2 + \cdots + a_{2,n}^2\right),$$

$$\left(\Delta a_N^*\right)^2 \simeq \left(\frac{500A}{3}\right)^2 \left[\left(a_{1,1} - a_{2,1}\right)^2 + \left(a_{1,2} - a_{2,2}\right)^2 + \cdots + \left(a_{1,n} - a_{2,n}\right)^2\right],$$

$$\left(\Delta b_N^*\right)^2 \simeq \left(\frac{200A}{3}\right)^2 \left[\left(a_{2,1} - a_{3,1}\right)^2 + \left(a_{2,2} - a_{3,2}\right)^2 + \cdots + \left(a_{2,n} - a_{3,n}\right)^2\right],$$

$$A = \frac{Y^{-2/3}}{Y_n^{1/3}},$$

$$Y = 18.4 \quad (L^* = 50),$$

$$Y_n = 100,$$

The matrix $\mathbf{M_T}$ can be further optimized to improve the average color difference ΔE_{00} (S_L=1). The MATLAB nonlinear optimization function *fminunc* was used to optimize the matrix $\mathbf{M_T}$ and minimize the average color difference ΔE_{00} (S_L=1). The MATLAB function *fminunc* finds the minimum of unconstrained multivariable function (MathWorks, n.d.). The starting pseudoinverse matrix from the actual and predicted camera signal served as the starting values while the offsets starting value was at 0. The *fminunc* yield better matrix coefficients with a lower average color difference ΔE_{00} (S_L=1) of 0.89. Maximum iterations and maximum function

evaluations were set at 30,000 and even at a setting higher than that, the optimized matrix remained the same. For *fminunc,* convergence can occur at a local minimum rather than true minimum, as such the average color difference ΔE_{00} (S_L=1) of 0.89 is probably the minimum value. The optimization also resulted in a lower noise of 8.0 from 8.2, a noticeable decrease in a^* noise and 90th percentile was also seen (see Table 3).

As for the predicted camera signal, the optimization yields the same average color difference ΔE_{00} (S_L=1) of 0.15, the optimized matrix coefficients did not change (at one significant figure). Thus, the average color difference ΔE_{00} (S_L=1) of 0.15 is likely the minimum value. The noise also stayed the same for the optimized matrix coefficients.

The pseudo-inverse initial and optimized matrix coefficients are shown in Table 2. Their corresponding calculated total-color-difference statistics and transformation noise are shown in Table 3.

Table 2. Nonlinear optimization initial and final matrices.

Pseudoinverse matrices	**Matrix Coefficients**
Pseudoinverse initial matrix using actual camera signal	$\begin{pmatrix} 0.28 & -0.75 & 2.3 & -2.0 & 0.64 & -0.74 & 1.2 & -0.14 & 0.17 & -0.07 \\ 0.16 & -0.59 & 1.9 & -1.8 & 0.63 & -0.61 & 1.7 & -0.59 & 0.10 & -0.07 \\ 0.43 & -0.67 & 2.6 & -2.0 & 0.68 & -0.56 & 0.58 & -0.42 & 0.06 & 0.02 \\ 0.0 & 0.0 & 0.0 & 0.0 & 0.0 & 0.0 & 0.0 & 0.0 & 0.0 & 0.0 \end{pmatrix}$
Pseudoinverse initial matrix using predicted camera signal	$\begin{pmatrix} -0.03 & 0.32 & -0.64 & 0.54 & -0.22 & 0.14 & 0.19 & 0.56 & 0.16 & -0.19 \\ -0.04 & 0.19 & -0.47 & 0.38 & -0.10 & -0.02 & 1.22 & -0.24 & 0.09 & -0.14 \\ 0.11 & 0.26 & 0.19 & 0.12 & 0.04 & -0.02 & 0.04 & -0.04 & 0.02 & -0.02 \\ 0.0 & 0.0 & 0.0 & 0.0 & 0.0 & 0.0 & 0.0 & 0.0 & 0.0 & 0.0 \end{pmatrix}$
Pseudoinverse final matrix using actual camera signal	$\begin{pmatrix} 0.27 & -0.70 & 2.3 & -2.0 & 0.55 & -0.74 & 1.4 & -0.18 & 0.21 & -0.13 \\ 0.18 & -0.60 & 2.0 & -1.8 & 0.54 & -0.55 & 1.7 & -0.56 & 0.14 & -0.13 \\ 0.45 & -0.65 & 2.6 & -2.0 & 0.69 & -0.58 & 0.57 & -0.36 & 0.06 & -0.03 \\ 2.5\,x10^{-5} & -1.4\,x10^{-4} & -1.1\,x10^{-4} & 1.0\,x10^{-4} & 8.2\,x10^{-6} & -4.6\,x10^{-4} & -1.2\,x10^{-4} & 9.1\,x10^{-6} & 3.9\,x10^{-4} & -2.6\,x10^{-4} \end{pmatrix}$
Pseudoinverse final matrix using predicted camera signal	$\begin{pmatrix} -0.03 & 0.32 & -0.64 & 0.54 & -0.22 & 0.14 & 0.19 & 0.56 & 0.16 & -0.19 \\ -0.04 & 0.19 & -0.47 & 0.38 & -0.10 & -0.02 & 1.22 & -0.24 & 0.09 & -0.14 \\ 0.11 & 0.26 & 0.19 & 0.12 & 0.04 & -0.02 & 0.04 & -0.04 & 0.02 & -0.02 \\ -2.0\,x10^{-5} & -6.0\,x10^{-5} & -1.7\,x10^{-5} & -4.1\,x10^{-5} & -9.1\,x10^{-10} & -5.2\,x10^{-8} & -1.0\,x10^{-5} & -1.2\,x10^{-5} & -9.7\,x10^{-6} & 1.1\,x10^{-5} \end{pmatrix}$

Table 3. Color matrix transformation optimization results.

Metric	Actual Camera Signal	Predicted Camera Signal
Before Optimization		
Average $\Delta E_{00}(S_L = 1)$	1.0	0.15
90th percentile $\Delta E_{00}(S_L = 1)$	1.9	0.30
ΔL_N^* noise	4.4	1.9
Δa_N^* noise	5.2	8.1
Δb_N^* noise	4.4	3.4
N	8.2	9.0
Following optimization		
Average $\Delta E_{00}(S_L = 1)$	0.89	0.15
90th percentile $\Delta E_{00}(S_L = 1)$	1.4	0.30
ΔL_N^* noise	4.4	1.9
Δa_N^* noise	4.4	8.1
Δb_N^* noise	4.3	3.4
N	8.0	9.0

The difference in the reflectance spectra of the target and the predicted reflectance calculated from the actual camera signal and the predicted camera signal is shown in Figure 15 and Figure 16. The subplots comparing the measured reflectance from the target to the predicted reflectance calculated using the actual camera signal and the predicted camera signal is seen below (Figure 17 and Figure 18). The predicted reflectance calculated using the actual camera signal and predicted camera signal showed a good estimation with differences ranging from -0.15 to +0.45 for actual camera signal and -0.15 to +0.3 for predicted camera signal. The computed RMSE for actual camera signal is 0.03 while the RMSE for predicted camera signal is 0.02. Based on Figure 15 and Figure 16, the predicted camera signal predicted the reflectance spectra better along the visible range (400-700 nm) than the actual camera signal. However, the difference in the calculated

RMSE is likely not significantly different from each other and both did well in predicting reflectance as seen in individual subplots of the patches in Figures 17 and 18.

The actual camera signal even after optimization (ΔE_{00} (S_L=1) of 0.89), resulted in a higher mean color difference than the predicted camera signal ΔE_{00} (S_L=1) of 0.15. This is expected given that the actual imaging is affected by external factors adding noise to the actual imaging process. External factors in the imaging set up causing uncertainty in the image (e.g. environment, human and instrument error) could have affected the actual camera signal thus yielding a poorer color difference statistic.

In terms of noise, actual camera signal yields roughly similar color transformation noise as the predicted camera signal. This proves that the noise equation was able to efficiently predict the noise brought about by color transformation. This is an important result that proves the reliability of the computational imaging simulation. Computational imaging simulations sought to determine the best possible LED combination would be performed and shall be the focus in the next chapter.

The LAB vector plot for the measured and predicted colorimetric data is shown in Figure 19 and Figure 20. The predicted colorimetric data from the actual camera signal is shown in Figure 19 while the predicted colorimetric data from the calculated predicted camera signal is shown in Figure 20. The LAB vector plot for the optimized matrix cooefficients from the actual camera signal was also presented in Figure 21, since the optimized matrix coefficients from the predicted camera signal remained the same, no additional LAB vector plot was shown.

The colored dot defines the coordinates of the measured patch while the arrowhead defines the coordinates of its estimate. As seen in Figures 15-21 the camera model showed a good estimation for the reflectance and colorimetric data.

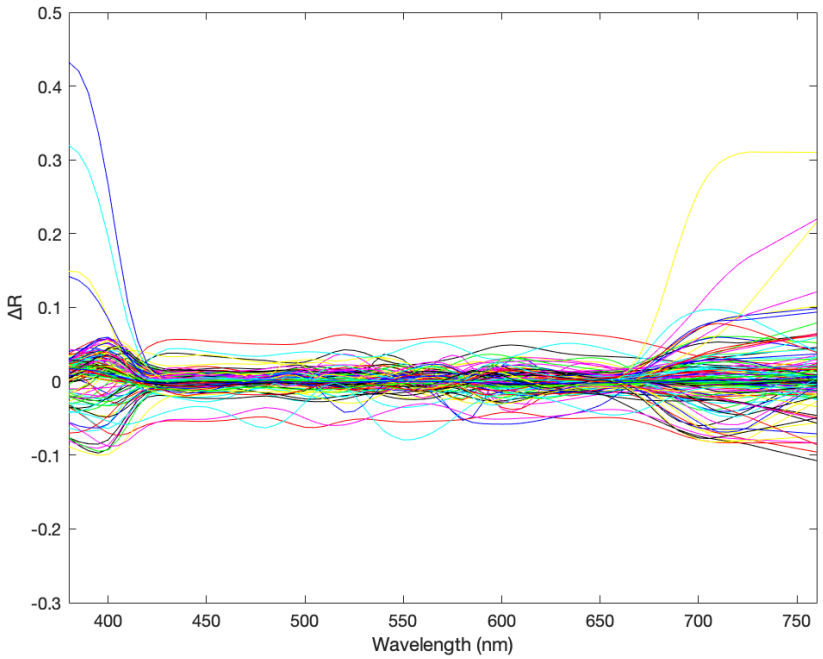

Figure 15. The difference between the measured spectra and the calculated predicted spectra from the actual camera signal.

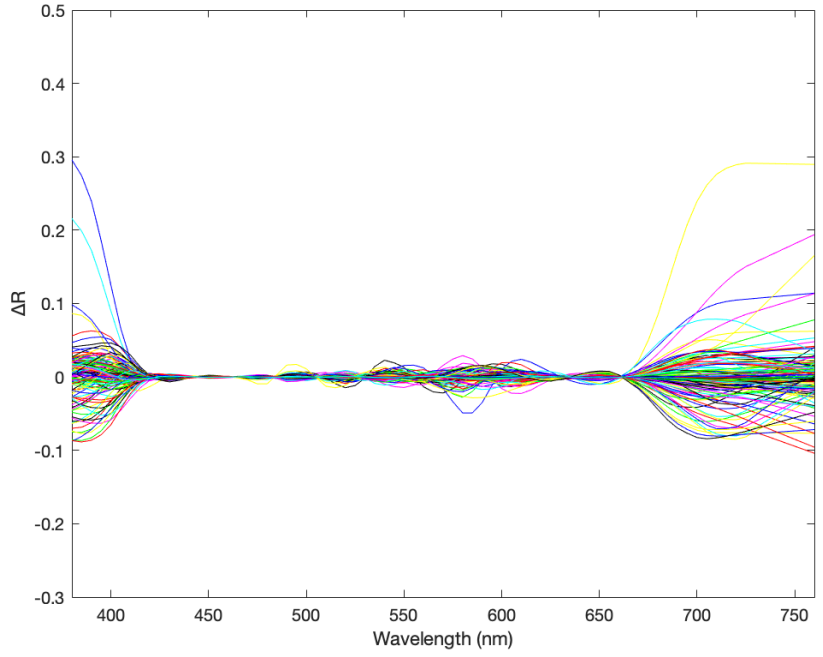

Figure 16. The difference between the measured spectra and the calculated predicted spectra from the predicted camera signal.

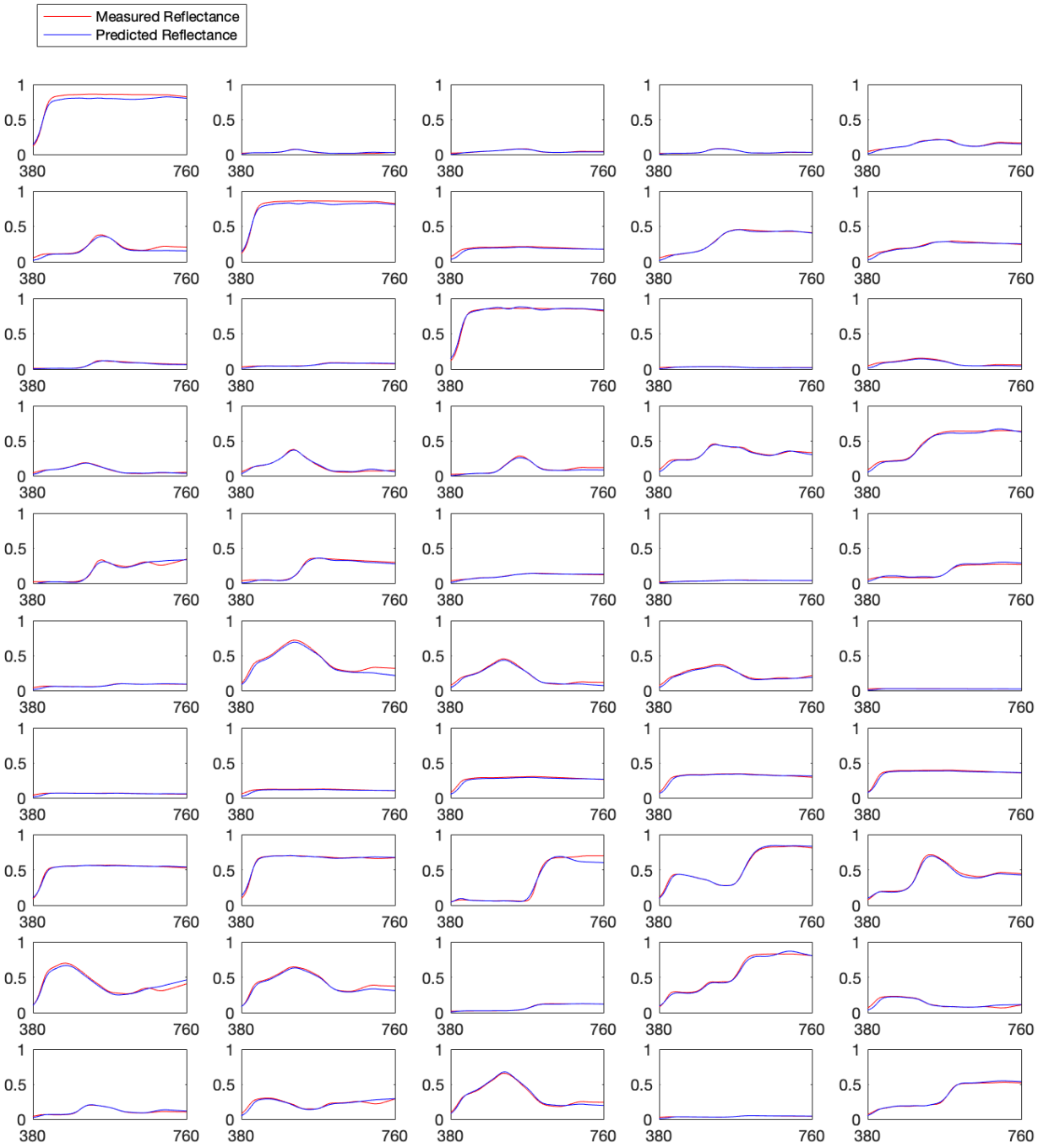
Measured Reflectance
Predicted Reflectance
1
0.5
0
380
760

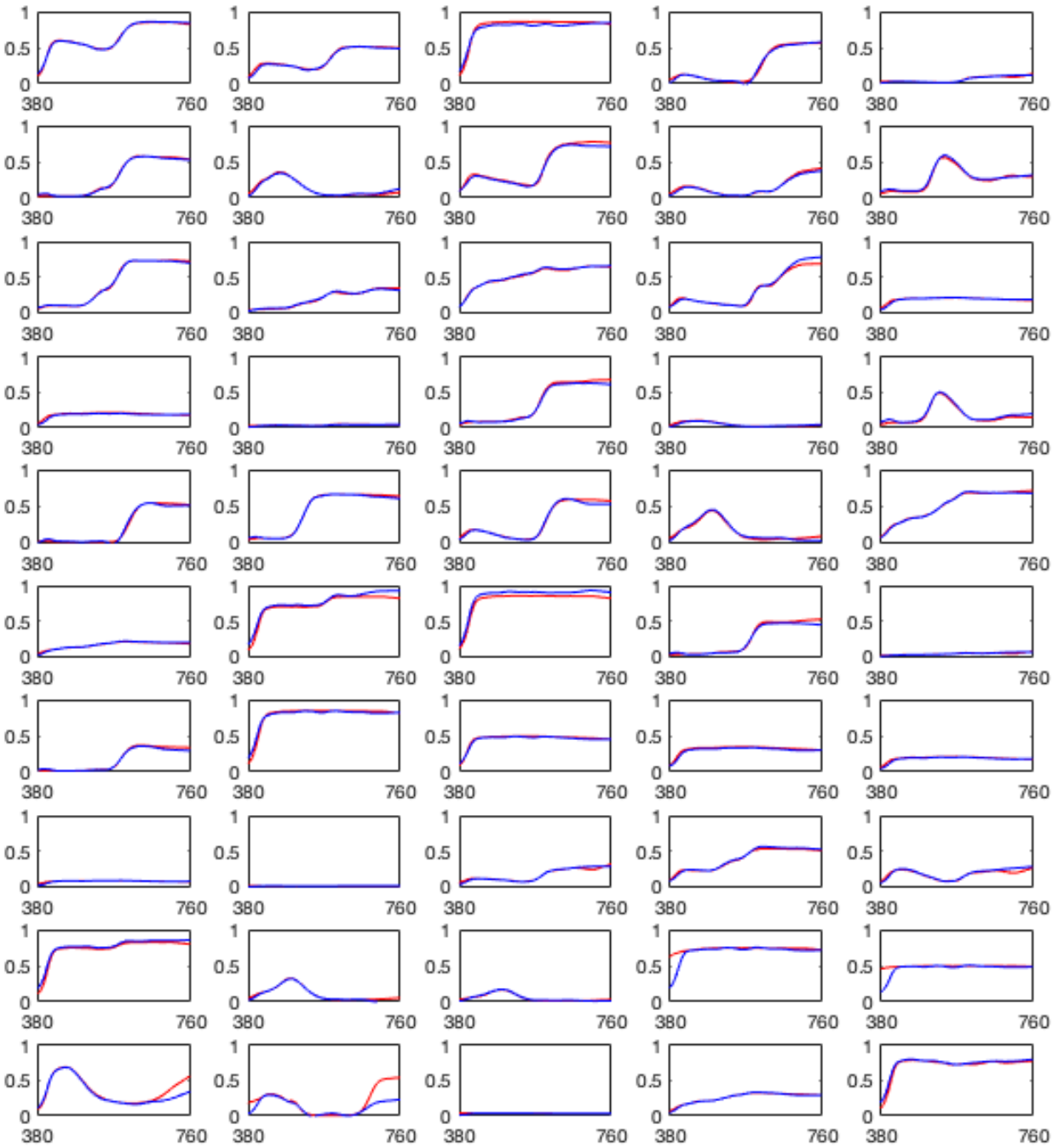
1
0.5
0
380
760

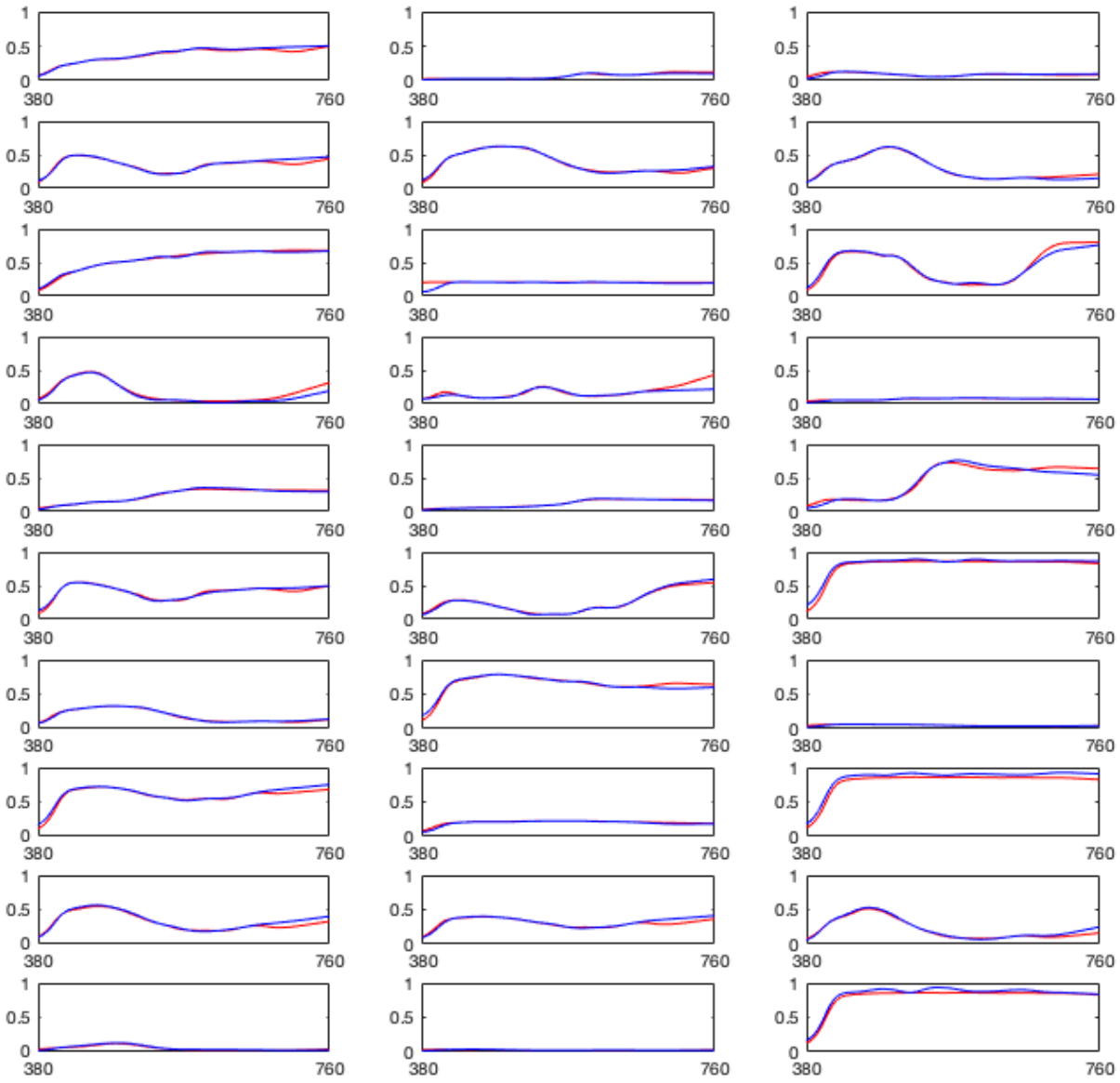

Figure 17. The measured reflectance spectra (red line) compared to the predicted reflectance spectra (blue line) calculated from the actual camera signal.

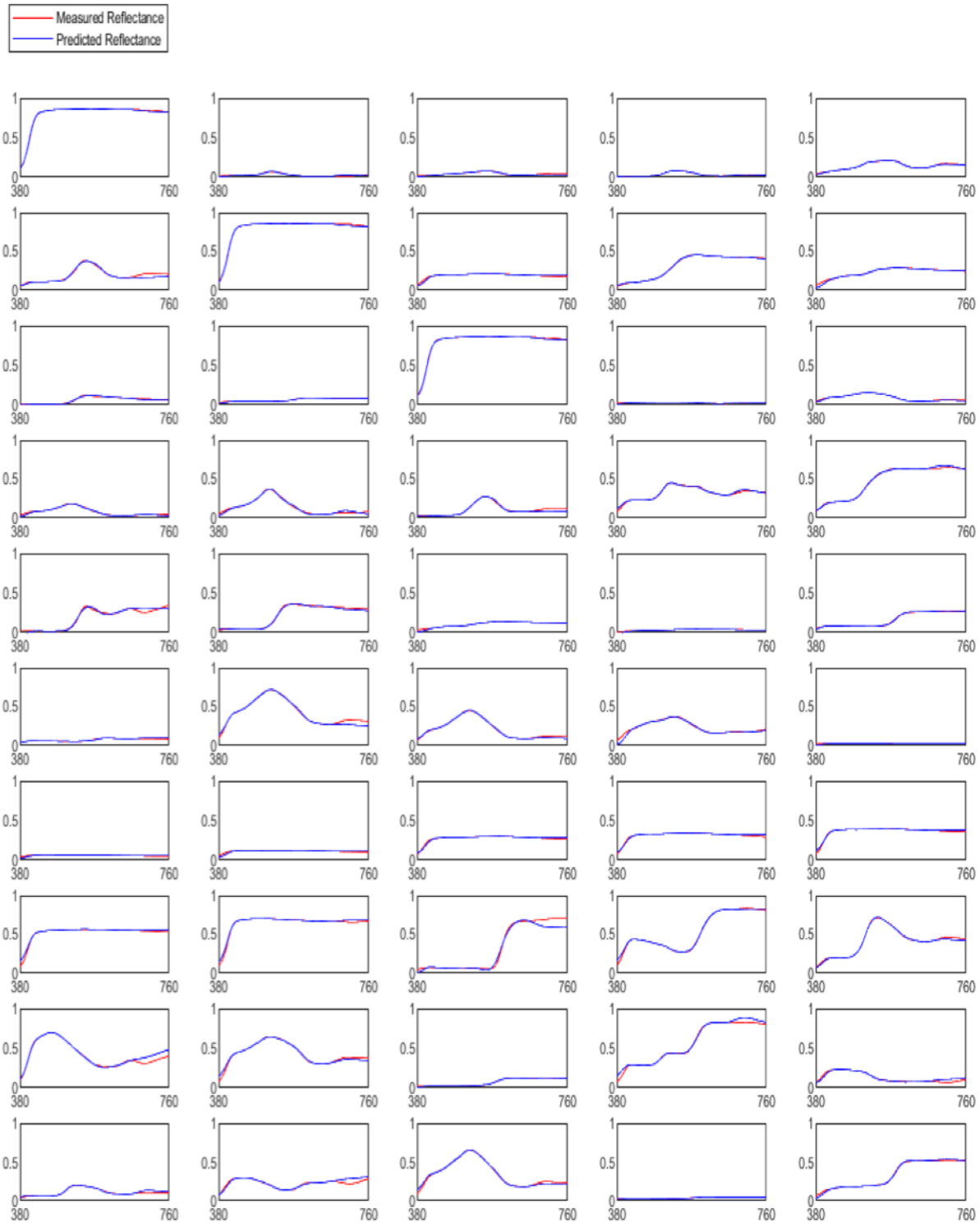
Measured Reflectance
Predicted Reflectance
0
0.5
1
380
760

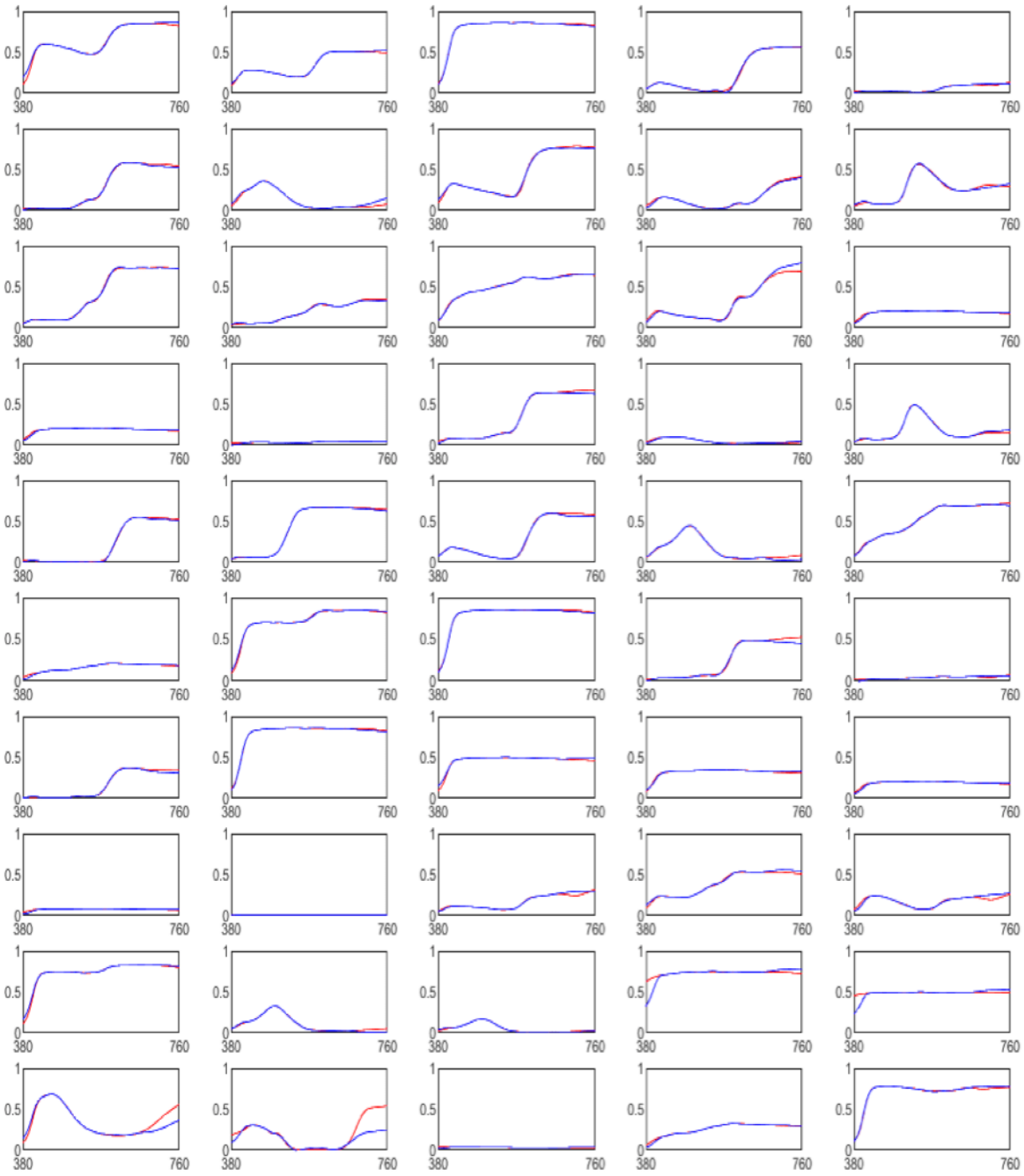
1
0.5
0
380
760

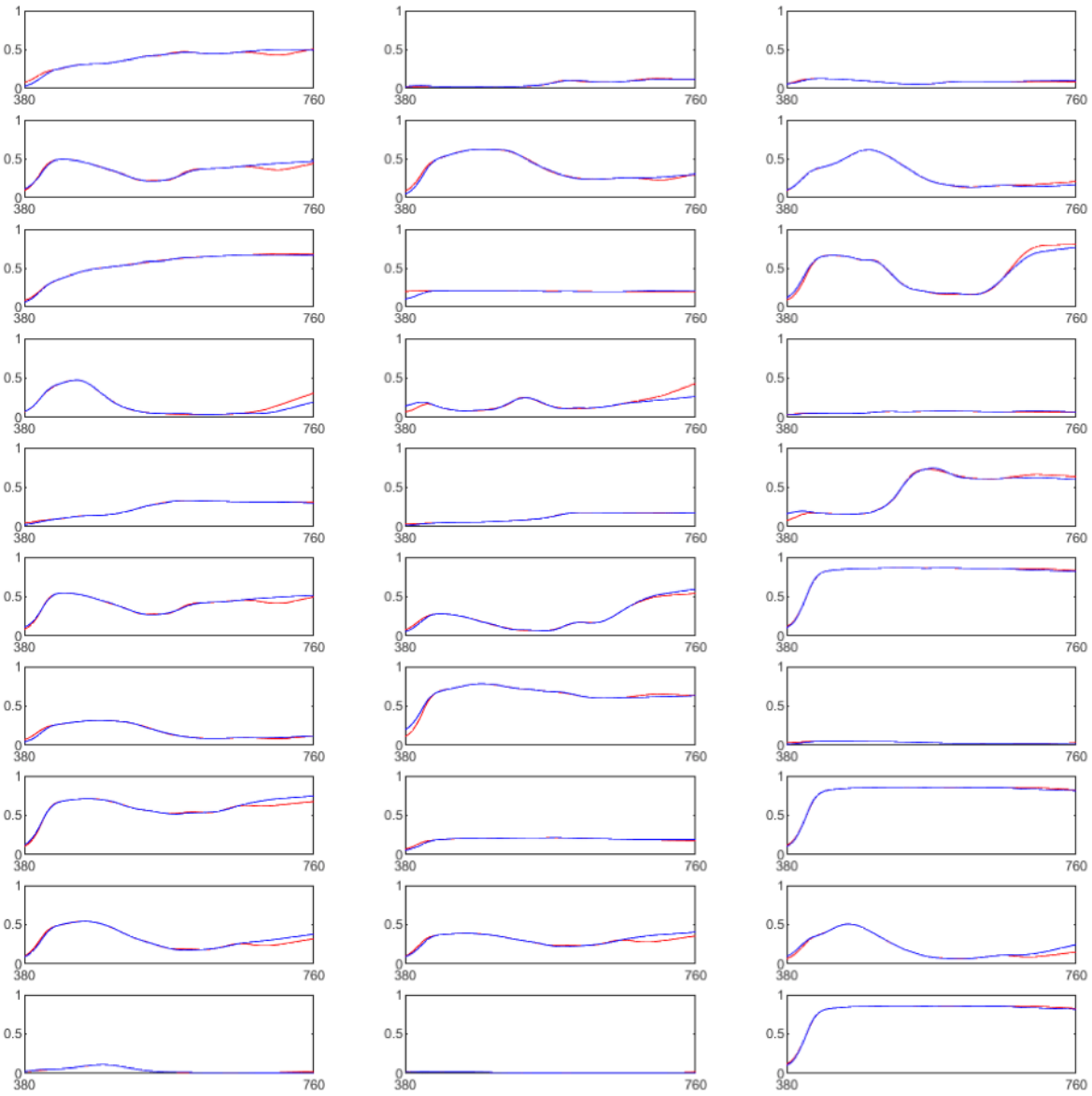

Figure 18. The measured reflectance spectra (red line) compared to the predicted reflectance spectra (blue line) calculated using the predicted camera signal.

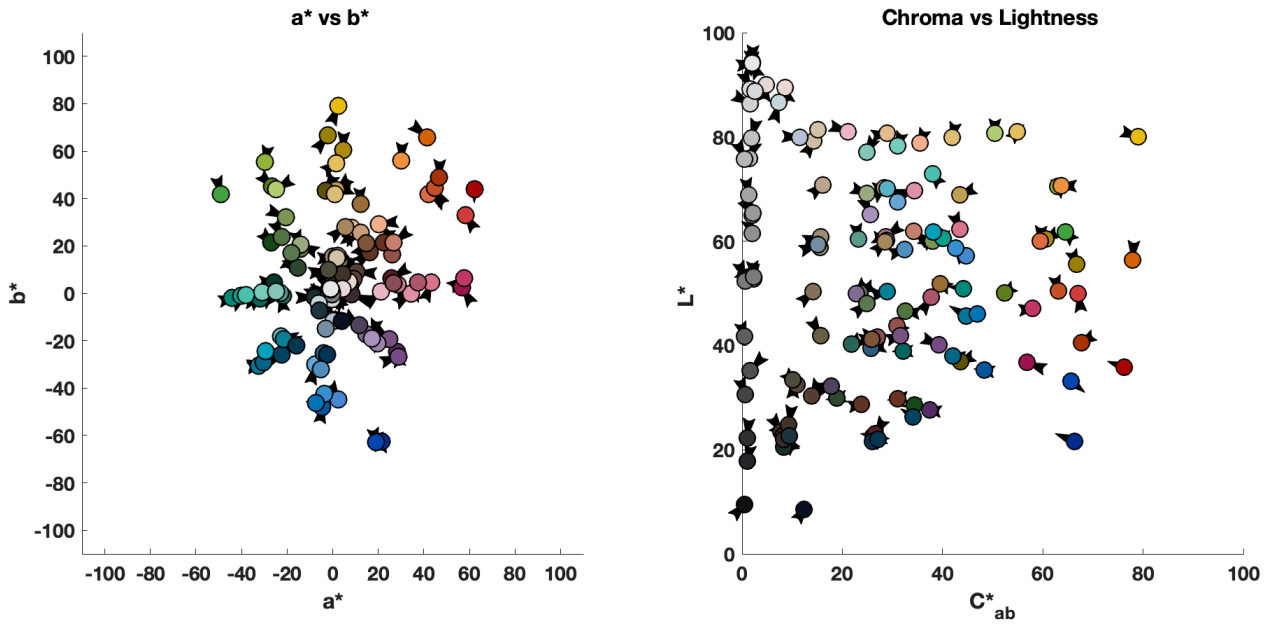

Figure 19. CIELAB a* vs. b* and L* vs. C^*_{ab} vector plots of the measured and predicted colorimetric data calculated from the actual camera signal.

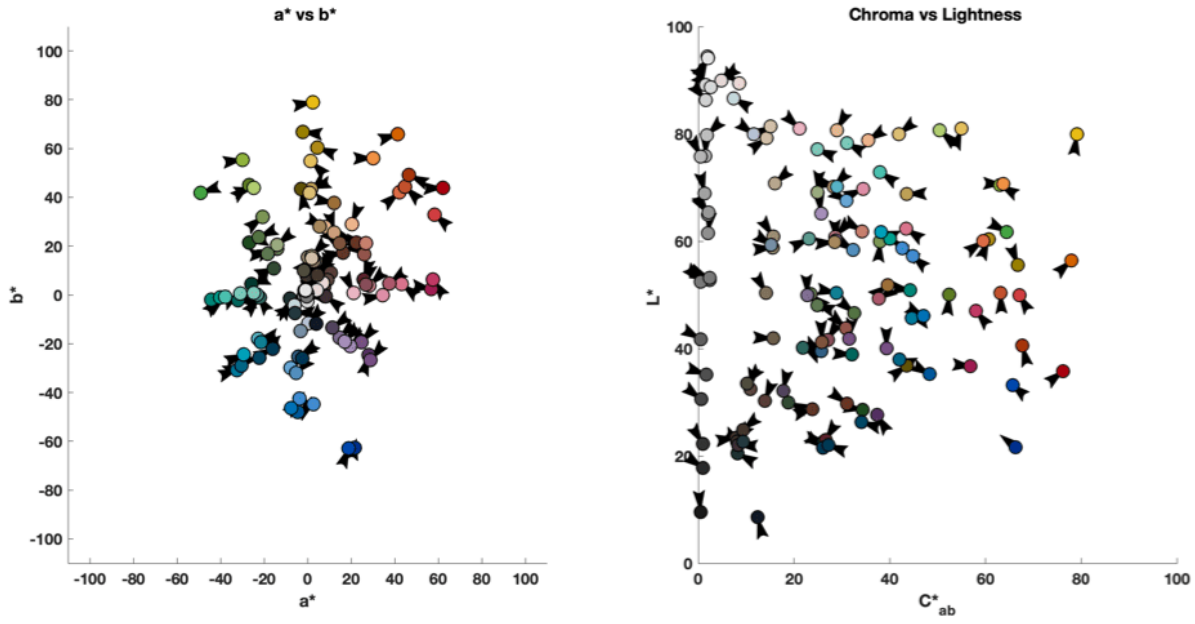

Figure 20. CIELAB a* vs. b* and L* vs. C^*_{ab} vector plots of the measured and predicted colorimetric data calculated from the predicted camera signal.

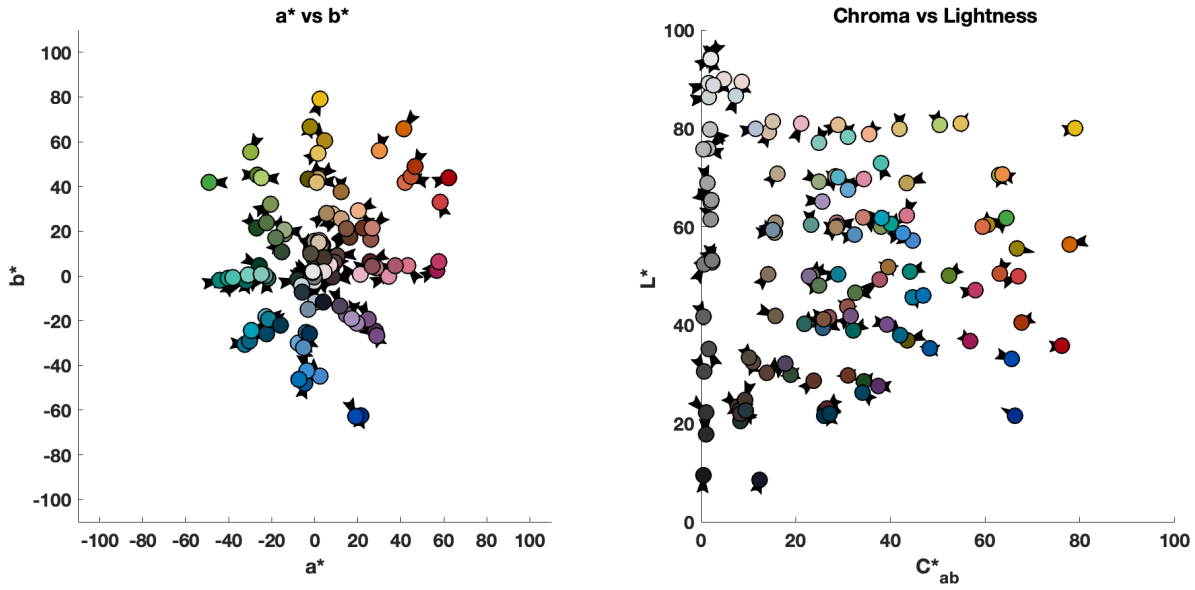

Figure 21. CIELAB a* vs. b* and L* vs. C^*_{ab} vector plots of the measured and predicted colorimetric data calculated from the optimized matrix coefficients of the actual camera signal.

3.5 Conclusions

The purpose of this chapter is to verify the camera model using the currently available LEDs at Munsell Color Science laboratory. The application of LED lights in multispectral imaging is introduced. Initial experiments using the available LEDmotive system composed of 10 LEDs proved to be effective in multispectral imaging. Both metrics (RMSE and ΔE_{00} (S_L=1) used to evaluate spectral and colorimetric data showed high spectral and color accuracy. Noise attributed to color transformation was also reasonably low. The color transformation noise from the actual camera signal and from the predicted camera signal are roughly the same, proving the efficiency of the camera model in predicting noise brought about by color transformation. This here is vital in computational imaging simulation, as such that the behavior of the computational imaging system mimics the actual imaging system and that the camera model performed reasonably well. In addition to, the camera model was successful in predicting the camera signal with almost perfect linearity and an R^2 of 0.99. The actual camera signal resulted in a higher mean color difference than the predicted camera signal. An increase in the area of the patch taken to get the actual camera signal may help in yielding a better color difference statistic. Bear in mind that the actual imaging is subjected to other types of noise. External factors in the imaging set up causing uncertainty in the image (e.g. environment, human and instrument error) could have also affected the actual camera signal.

The MATLAB *fminunc* optimization was able to optimize the average color difference for the actual camera signal but not significantly, perhaps another optimization method could be used to achieve the true minimum instead of the local minimum. A change in starting value could also yield a better optimization result.

All in all, this chapter proved that the camera model is valid and effective in predicting the camera signal taking into account the color transformation noise.

Chapter 4: Optimal LED Selection

This chapter describes the computational LED selection performed in order to define the optimal LED combination for a 10-channel multispectral imaging system. The chapter is divided into parts to describe the processes taken in order to narrow down the combinations and the chosen metrics used to evaluate the colorimetric and spectral accuracy of each LED combination.

4.1 LED (Light Emitting Diode) system

A total of thirty-seven lights (37) were available from LEDmotive Technologies. The manufacturer provided the normalized spectral power distribution for all 37 lights as seen in Figure 22. The lights have the wavelength range of (380 nm-760 nm). The manufacturer is able to manufacture an LED system composed of 10-12 LEDs. In order to reduce the cost, it was ultimately decided to use 10 LEDs. A straightforward method for LED selection would be to simulate all possible LED combinations and then determine the best LED combination under a given metric. Doing this is impractical, it's computationally expensive and time consuming. Computing for all possible combinations using the permutation formula without repetition as seen in Equation 9 yields 348,330,136 combinations, where n is the combination of LEDs taken k at a time. Furthermore, since some of LEDs cluster in a specific range, it would yield uninformative combinations such as a set of all short wavelength LEDs or long wavelength LEDs. The best way to avoid this and to reduce the computational time is to group the LEDs according to their region of interest. The LEDs were divided according to a specified peak range (see Figure 1), doing this reduced the possible combinations to 110,592. The name of the LEDs is assigned as numbers 1-37 from left to right, these numbers served as the guide in identifying the optimum LED later on the experiment. LED numbers 1-9 is bin number 1, LED numbers 10-13 is bin number 2, LED numbers 14-17 is bin number 3, LED numbers 18-21 is bin number 4, LED numbers 22-25 is bin number 5, LED number 26 is bin number 6, LED numbers 27-30 is bin number 7, LED numbers 31-32 is bin number 8, LED numbers 33-34 is bin number 9 and LED numbers 35-37 is bin number 10. LED 26 is in its own bin because the LED's peak is similar to $\mathbf{V}(\lambda)$ which is important in the spectral and colorimetric accuracy of the imaging system. Therefore, putting it in its own bin assures that the LED is chosen for all possible combinations. The LEDs with their corresponding peaks wavelength (nm) are shown in Table 4 below. In order for the imaging to be effective, the

LEDs must cover if not the entire electromagnetic spectrum then at least the range of the visible spectrum.

$$C(n,k) = \frac{n!}{k!\,(n-k)!} \tag{9}$$

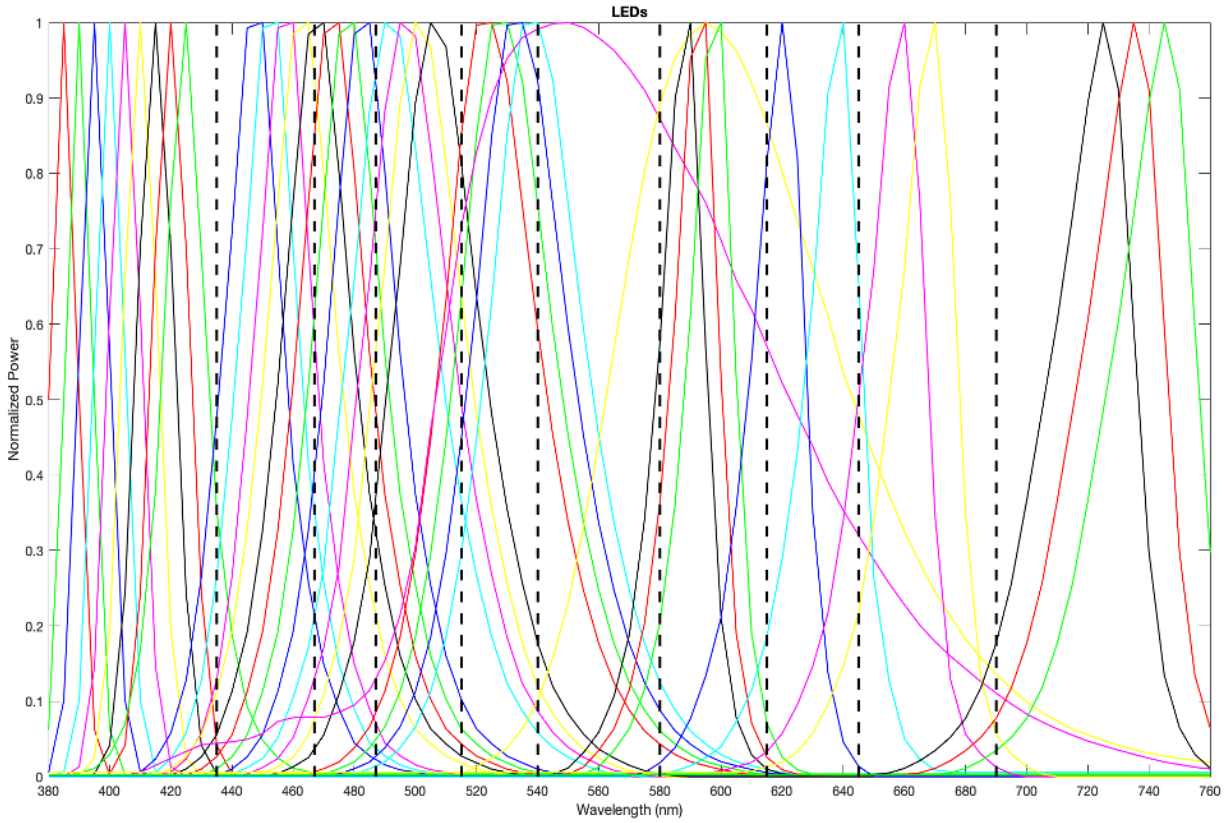

Figure 22. Normalized spectral power distributions of 37 LEDs used in the simulation.

Table 4. Peak wavelengths of the 37 available LEDs.

LED numbers	Peak wavelength (nm)
1	385
2	390
3	395
4	400
5	405
6	410

7	415
8	420
9	425
10	450
11	455
12	460
13	465
14	470
15	475
16	480
17	485
18	490
19	495
20	500
21	505
22	525
23	530
24	535
25	540
26	550
27	595
28	590
29	595
30	600
31	620
32	640
33	660
34	670
35	725
36	735
37	745

4.2 Computational Imaging Simulation

A flow chart of the computational LED selection is shown in Figure 23. The details for each level are discussed in the following paragraphs. The metrics chosen in the selection are ΔE_{00} for colorimetric accuracy, RMSE for spectral accuracy and color transformation noise for image quality. In addition, Throughput (correlated with S/N) and a statistical test such as Goodness-of-fit (GFC) were also applied.

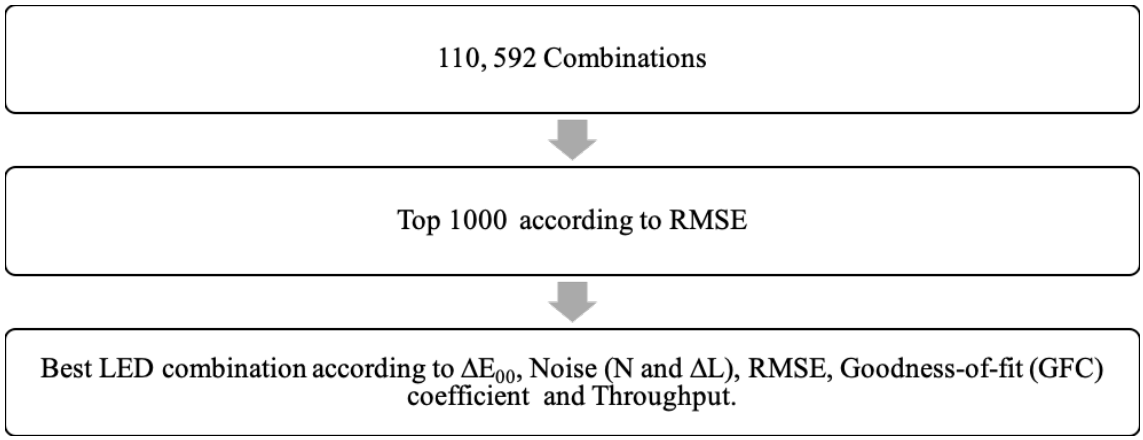

Figure 23. Computational LED Selection simulation flow.

The calculated predicted camera signal (derived from Equation 1 in Chapter 3) was used to calculate the predicted reflectance (see Equation 2 in Chapter 3) and predicted tristimulus values of the patches (see Equation 5 in Chapter 3). Root-mean-square-error (RMSE) was used as the metric for the reflectance spectral accuracy (see Equation 10 below) (Imai, F.H.; Rosen, M.R.; Berns, R.S., 2002). The combinations were ranked and only the top 1000 of the 110,592 combinations showing the lowest RMSE were further analyzed. RMSE was chosen as the first metric to use in narrowing down the results due to the importance of spectral accuracy in a multispectral imaging system. Colorimetric accuracy is important as well; however, excellent spectral accuracy is usually harder to achieve. From here on, the remaining 1000 combinations were evaluated according to ΔE_{00}, RMSE and Noise. CIE DE2000 was used as the metric for colorimetric accuracy with the positional function, SL, equal to unity (Berns, R., 2016). The noise parameter, *N*, (see Equation 8 in Chapter 3) was used to evaluate noise due to the color transformation in the imaging simulation for all the combinations (Kuniba, H., & Berns, R.S., 2009). Two additional metrics were computed to evaluate the combinations, Goodness-of-fit

(GFC) coefficient and Throughput. Goodness-of-fit (GFC) coefficient accounted for how well the predicted reflectance values fits the measured reflectance (Imai, F.H.; Rosen, M.R.; Berns, R.S., 2002). GFC calculation yields values ranging from 0-1, with 1 corresponding to the perfect estimation (Shrestha, R., Hardeberg, J. Y., & Boust, C., 2012). The MATLAB function *goodnessOfFit* was used in the computation for GFC. The function's detailed description and options can be seen here (Mathworks, n.d.). The normalized mean square error (NMSE) was chosen as the cost function as suggested in Li (2018) (Li, S. X., 2018). Throughput on the other hand, is the integration as a function of wavelength of the product of an LED's SPD and the camera's spectral sensitivity per LED combination.

$$RMSE = \sqrt{\frac{1}{n}\sum_{i=1}^{n}[T(\lambda_i) - \tilde{T}(\lambda_i)]^2} \qquad (10)$$

4.3 Results and Discussion

The frequency distribution of the LEDs for the top 1000 combinations is shown in Figure 24. The plot below shows the number of times in the 1000 combinations for which an LED was chosen within its bin. For example (see Figure 22), bin number 10 contains 3 LEDs, LED number 35, 36 and 37. From the graph presented in Figure 24 it can be seen that for the 1000 combinations, LED 35 wasn't chosen at all while LED 36 was chosen 649 times and LED 37 was chosen 351 times. LED 35 wasn't chosen at all because all possible combinations including this LED was eliminated and wasn't able to be on the Top 1000 combinations according to RMSE; it can be said that combinations using this LED did not yield good spectral accuracy. On the other hand, LED number 26, as expected, would be chosen 1000 times given that is the only LED in its bin; therefore it would automatically be chosen for all possible combinations. Dash lines were drawn within the plot to show the binning and wavelength range per bin were displayed as well.

The top 1000 combinations are shown below in Figure 24: noise is plotted in the z axis, average color difference ΔE_{00} (S_L=1) is plotted in the y axis and RMSE is plotted in the x axis. Noise in terms of lightness is also an important component to consider since noise in terms of lightness (ΔL) is visually perceived more than the other components; as such the noise (ΔL) was also plotted in a 3d plot with average color difference ΔE_{00} (S_L=1) and RMSE (see Figure 25). A

2d-plot for ΔE_{00} and RMSE is shown in Figure 27. As seen in the 3d plot in Figures 25 and 26, noise occurs at the lower limit of the noise range of 3.24-12.06, while in terms of noise (ΔL), the values are mostly lying in the middle around 1.4 of the noise (ΔL) range of 1.16-1.96. The average color difference ΔE_{00} (S_L=1) values are distributed along the lower and upper middle of its range of 0.10-0.24 and the RMSE values on the other hand lies heavily on the higher limit of the RMSE range of 6.2 $x10^{-3}$ - $6.5x10^{-3}$. The colorimetric and spectral accuracy range for the top 1000 combinations are all reasonable; as such, the noise component as well as the noise in terms of lightness (ΔL) should be evaluated thoroughly. Furthermore, the Throughput and GFC as additional metrics should help in narrowing down the results.

An ideal combination would show a plot of coordinates (0,0,0) wherein ΔE_{00}, noise and RMSE are all equal to zero. Thus, computing for the Euclidian distance from the origin for the 1000 combinations would help determine the best possible combination that is a compromise between ΔE_{00}, noise/noise (ΔL) and RMSE. The values were first normalized to give an equal weighting for each metric. The results were then ranked.

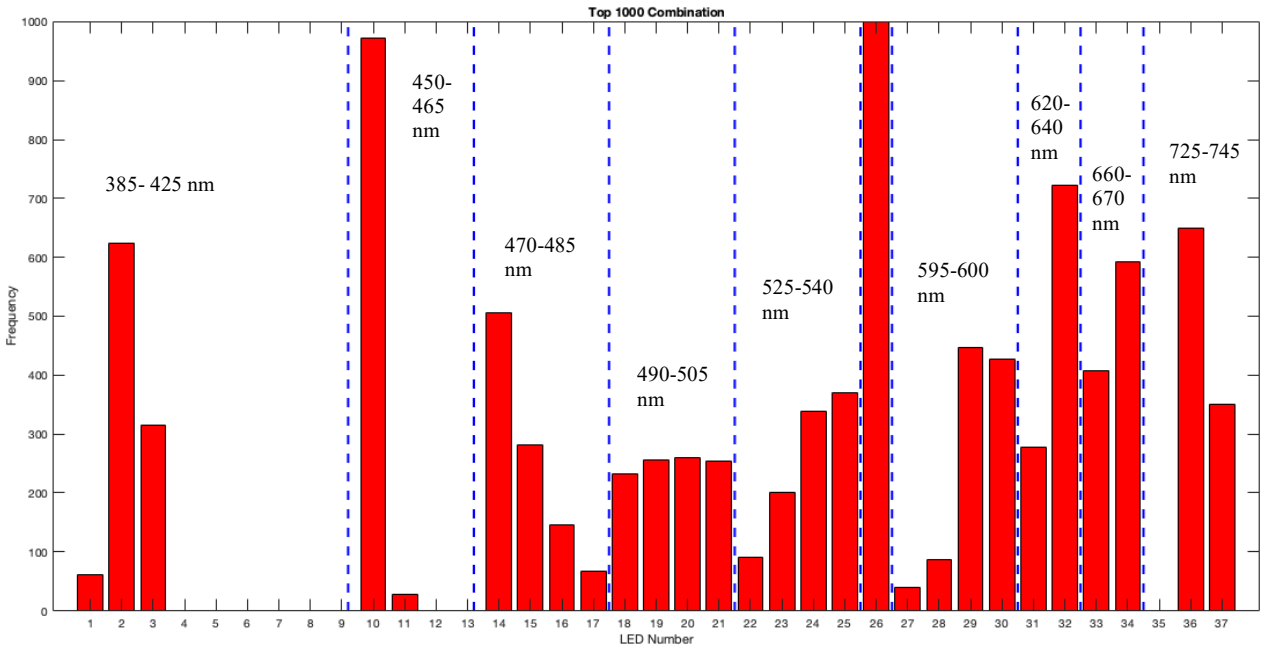

Figure 24. Frequency distribution of the LED lights for the Top 1000 Combinations.

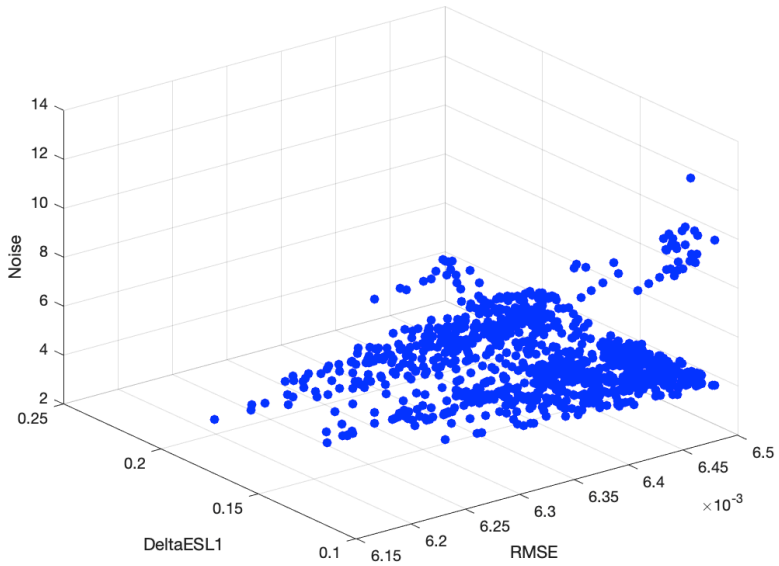

Figure 25. ΔE_{00}, Noise and RMSE of the top 1000 combinations.

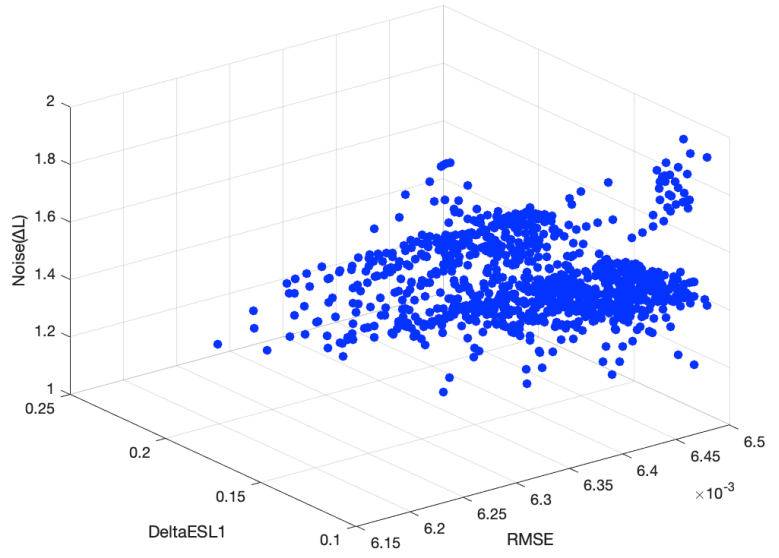

Figure 26. ΔE_{00}, Noise (ΔL) and RMSE of the top 1000 combinations.

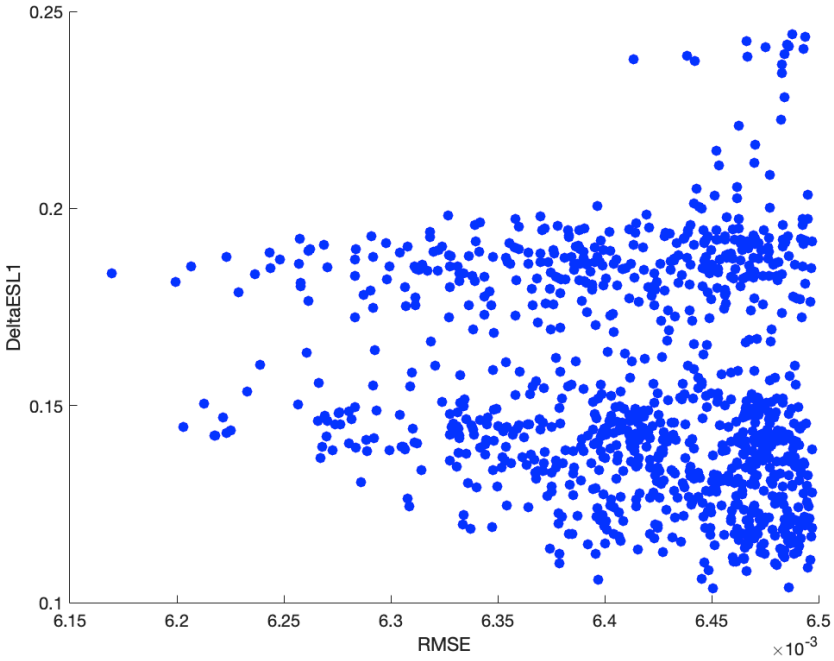

Figure 27. ΔE_{00} and RMSE of the top 1000 combinations.

A score ranking method was also used to look for a compromise between the three metrics. The score ranking method was performed by assigning the rank of the combinations as their score. The scores were then summed up to determine the best combination. The combinations were ranked in ascending order for each metric (ΔE_{00}, noise, noise (ΔL) and RMSE). For example, combination *n* is ranked 7 in ΔE_{00}, ranked 12 in total noise, ranked 10 in noise (ΔL) and ranked 5 in RMSE, it would then get a total of 34 points. The combinations with low total points were the ideal combinations since their ranks for each metric were mostly in the top.

The results for the score ranking method and both the Euclidean 3D plot for noise *N* and noise (ΔL) were then compared. It was found that certain combinations kept appearing in the top combinations for the three methods. These combinations are shown below. The combinations with their calculated metric are shown in Table 5. The signal to noise ratio for the said combinations are shown in Figures 28-31. The LED channels numbers for the top combinations were the same except for bin numbers 3, 7 and 10. Furthermore, none of the top combinations has the combination composed of all the most frequent LEDs within their bin. All top combinations have good colorimetric and spectral accuracy. Noise in terms of total noise, *N* and in terms of lightness (ΔL) were relatively low. Calculated GFC and Throughput were reasonable. As such, any of these

combinations might be considered optimal for building a LED-based multispectral imaging system. However, if only one is to be chosen among the top combinations, perhaps combination number 671 would be a better choice, the said combination ranked higher in most categories, particularly in ΔE_{00} (S_L=1), N (ΔL) and RMSE. Spectral and colorimetric data plots from LED combination number 671 is shown below. The subplots comparing the measured reflectance from the target to the predicted reflectance is shown in Figure 32. The difference in the reflectance spectra of the target and the predicted reflectance is shown in Figure 33. The predicted reflectance from LED combination number 671 showed a good estimation with differences ranging from -0.06 to +0.08. The LAB vector plot for the measured and predicted colorimetric data is shown in Figure 34. The colored dot defines the coordinates of the measured patch while the arrowhead defines the coordinates of its estimate. As seen in Figures 32-34, the LED combination number 671 showed a good estimation for the reflectance and colorimetric data.

Table 5. Top LED combinations.

Combination Number	**LED Channels number**	**ΔE_{00} (S_L=1)**	**Noise, *N***	**Noise (ΔL)**	**RMSE**	**GFC**	**Throughput**
671	2,10,15,21, 25,26,28, 31,33,37	0.12	3.35	1.22	$6.4x10^{-3}$	0.97	646.85
669	2,10,14,21, 25,26,28, 31,33,37	0.13	3.27	1.24	$6.3x10^{-3}$	0.97	645.46
83	2,10,15,21, 25,26,29, 31,33,36	0.12	3.58	1.36	$6.4x10^{-3}$	0.97	650.69
30	2,10,15,21, 25,26,28, 31,33,36	0.12	3.52	1.36	$6.4x10^{-3}$	0.97	649.87

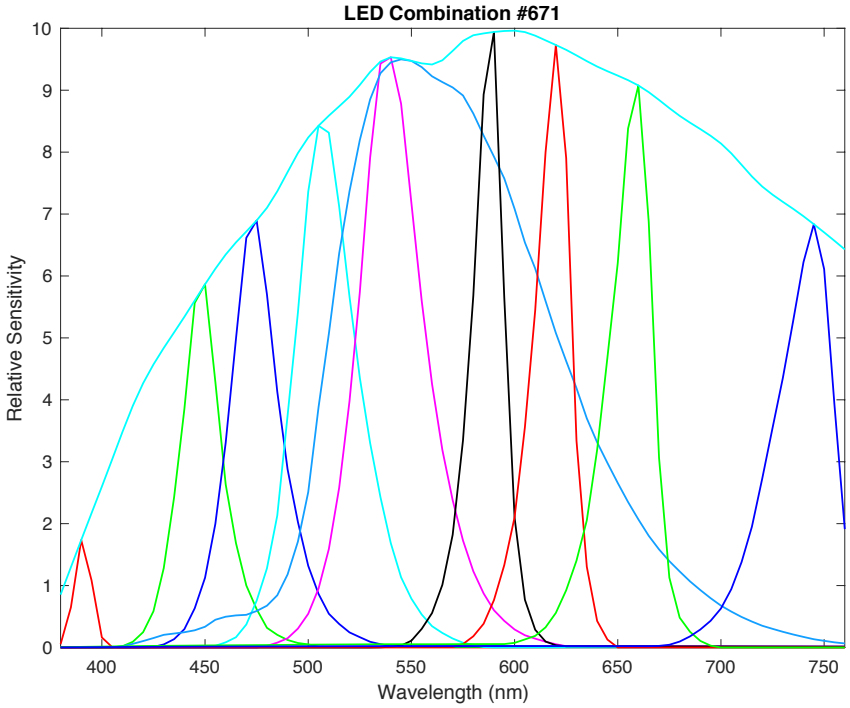

Figure 28. Signal to Noise Ratio for Combination # 671.

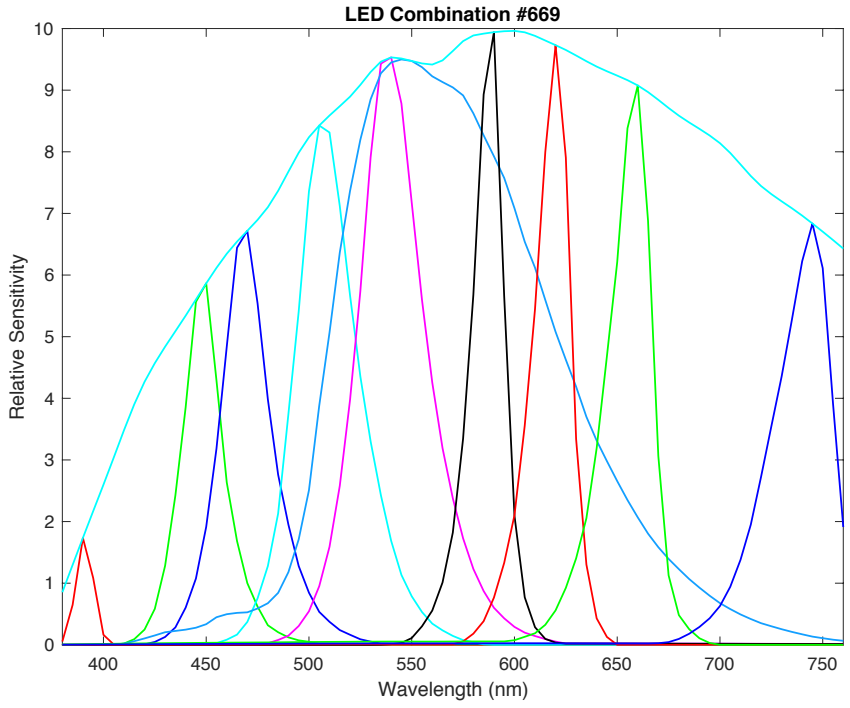

Figure 29. Signal to Noise Ratio for Combination # 669.

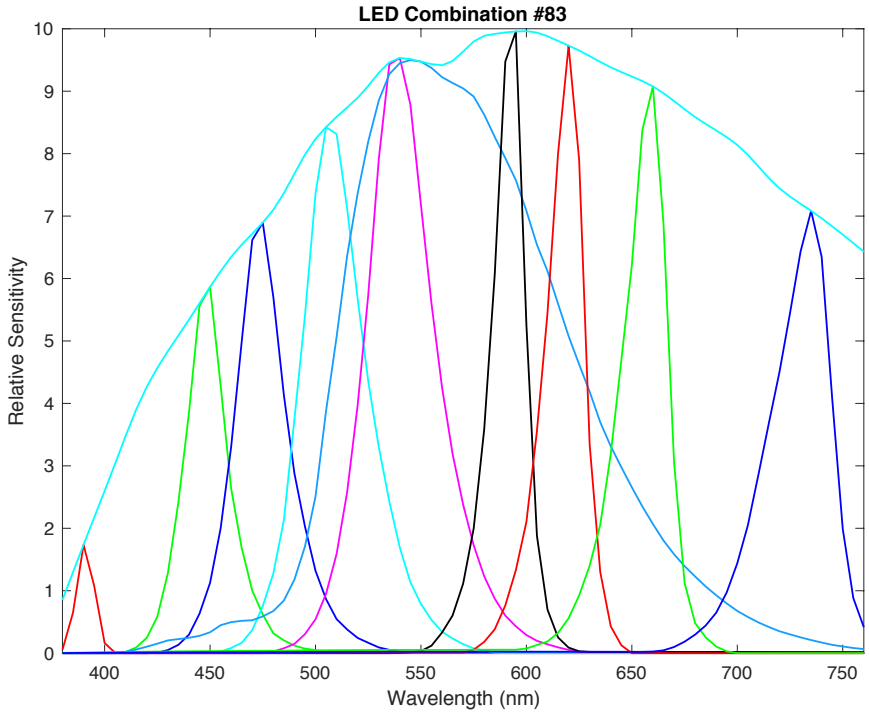

Figure 30. Signal to Noise Ratio for Combination # 83.

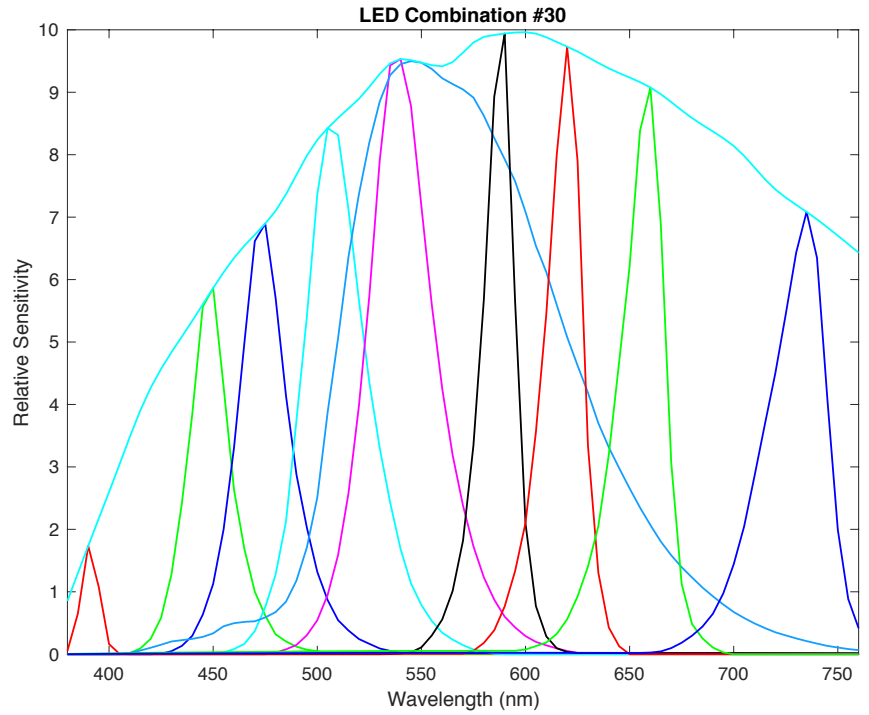

Figure 31. Signal to Noise Ratio for Combination # 30.

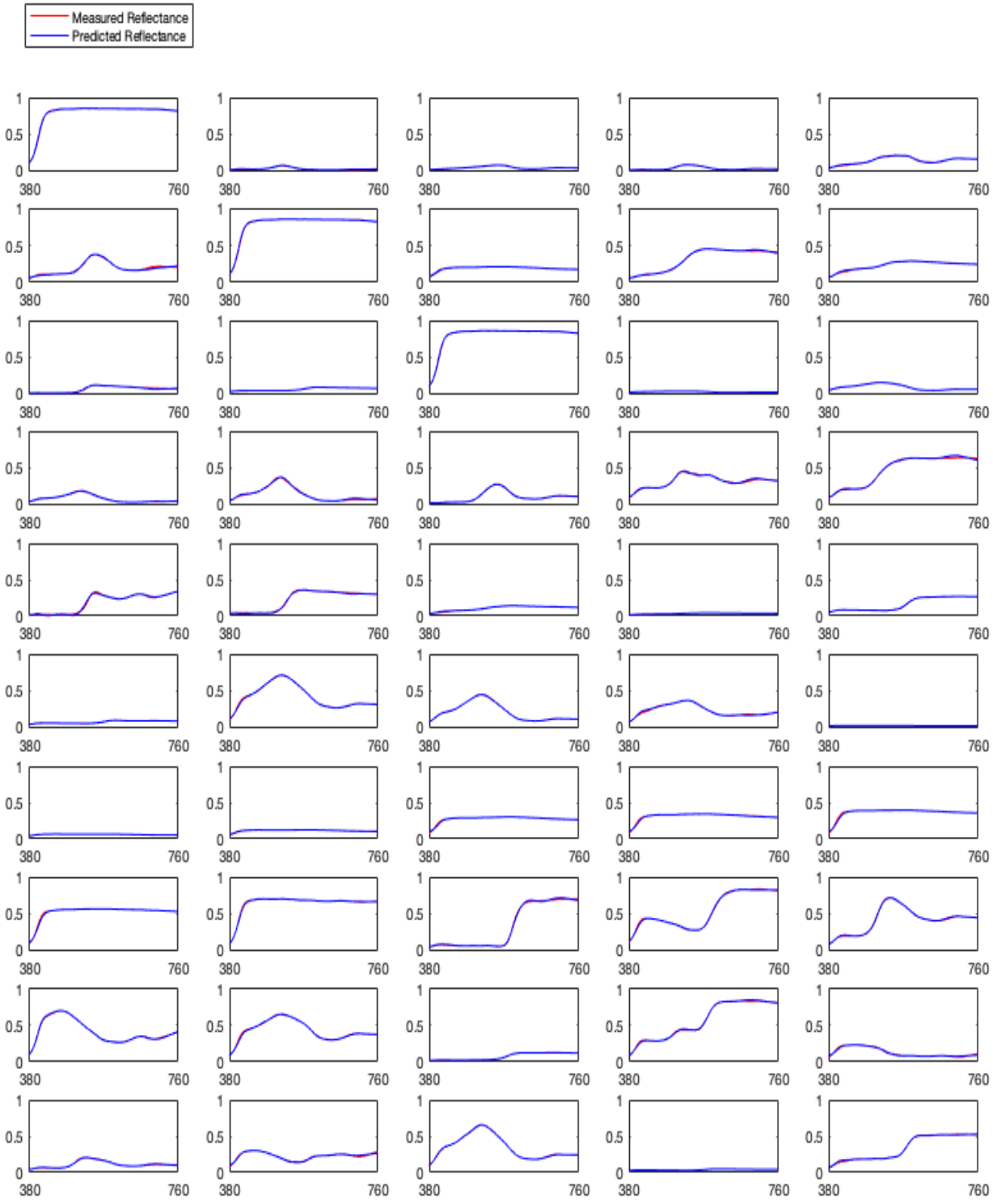
Measured Reflectance
Predicted Reflectance
0
0.5
1
380
760

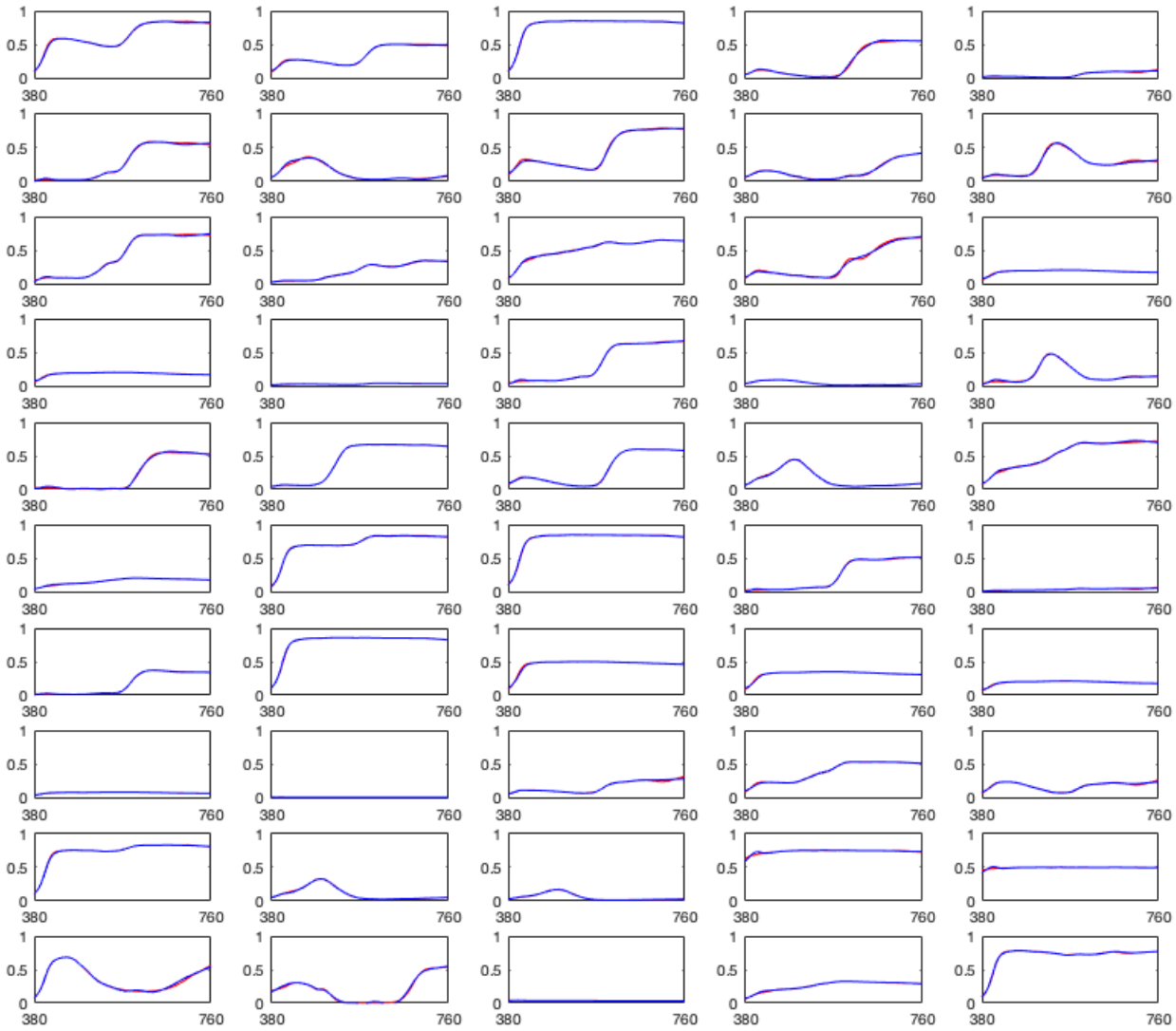
1
0.5
0
380
760

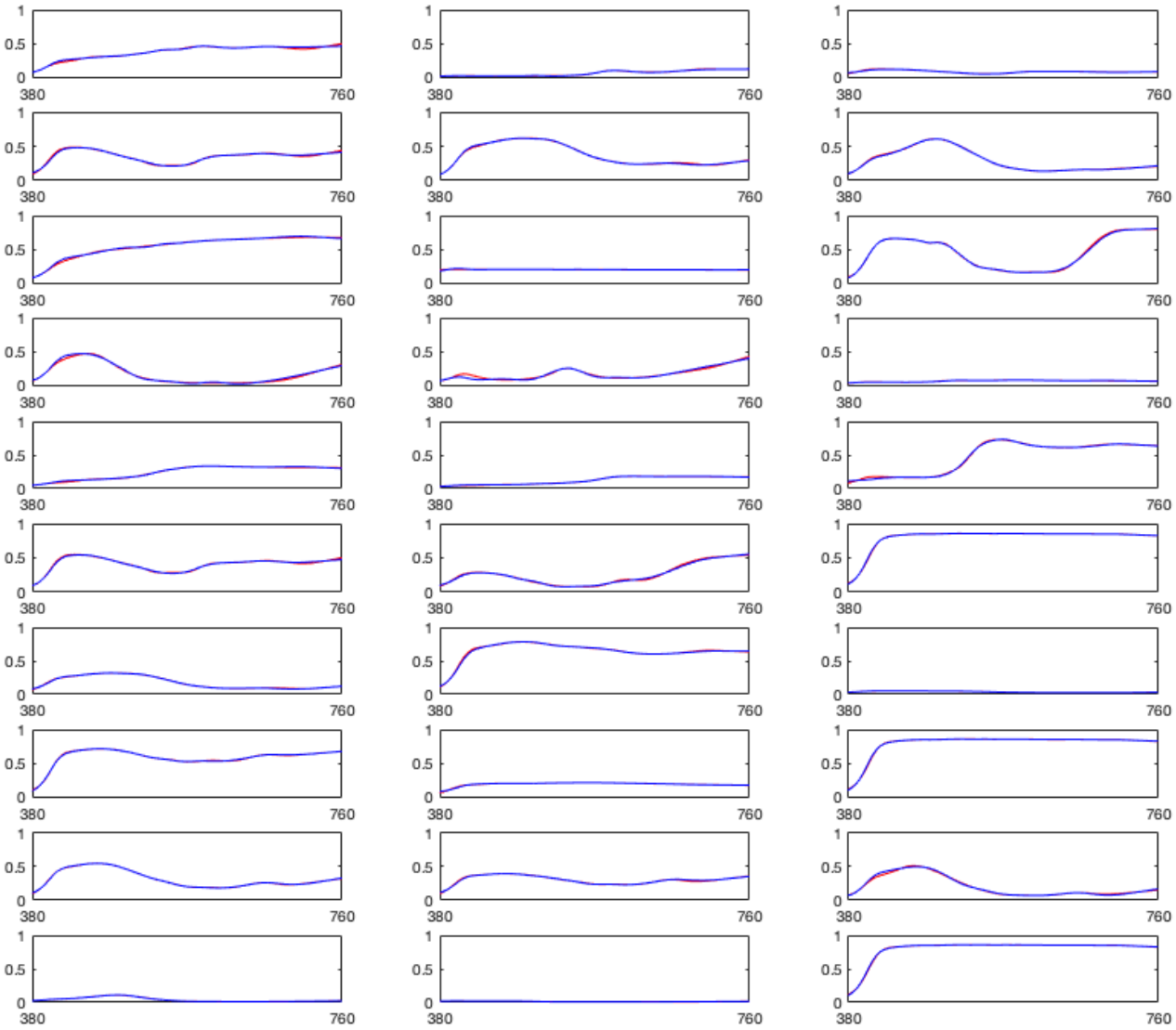

Figure 32. The measured reflectance spectra (red line) compared to the predicted reflectance spectra (blue line) calculated from LED combination number 671.

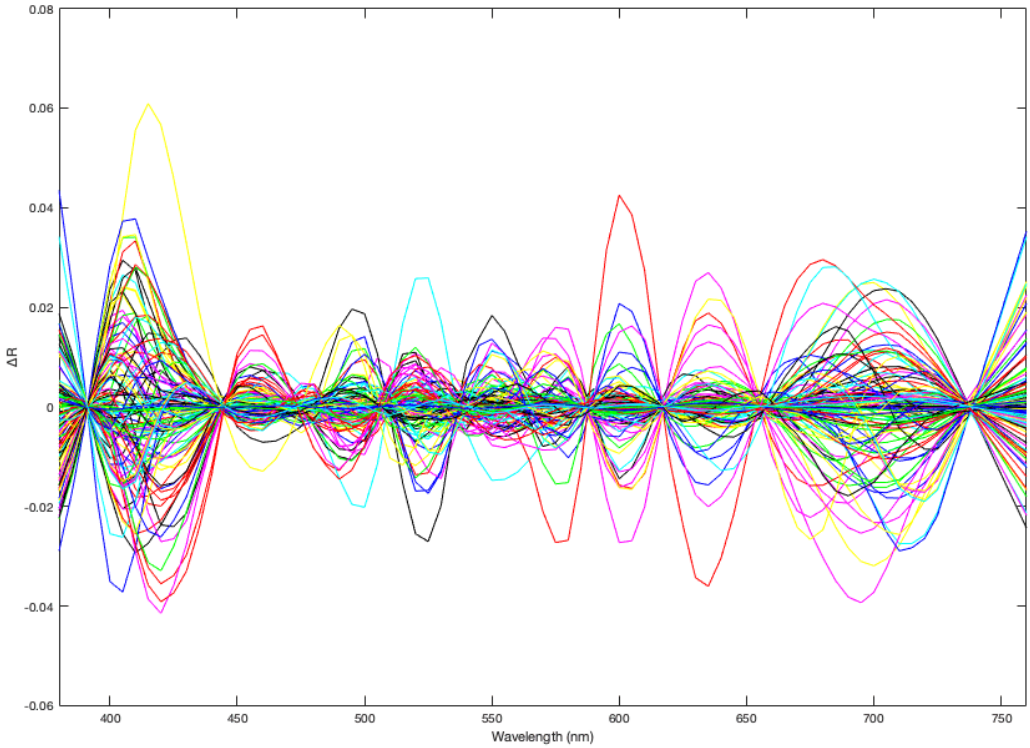

Figure 33. The difference between the measured spectra and the calculated predicted spectra from LED combination number 671.

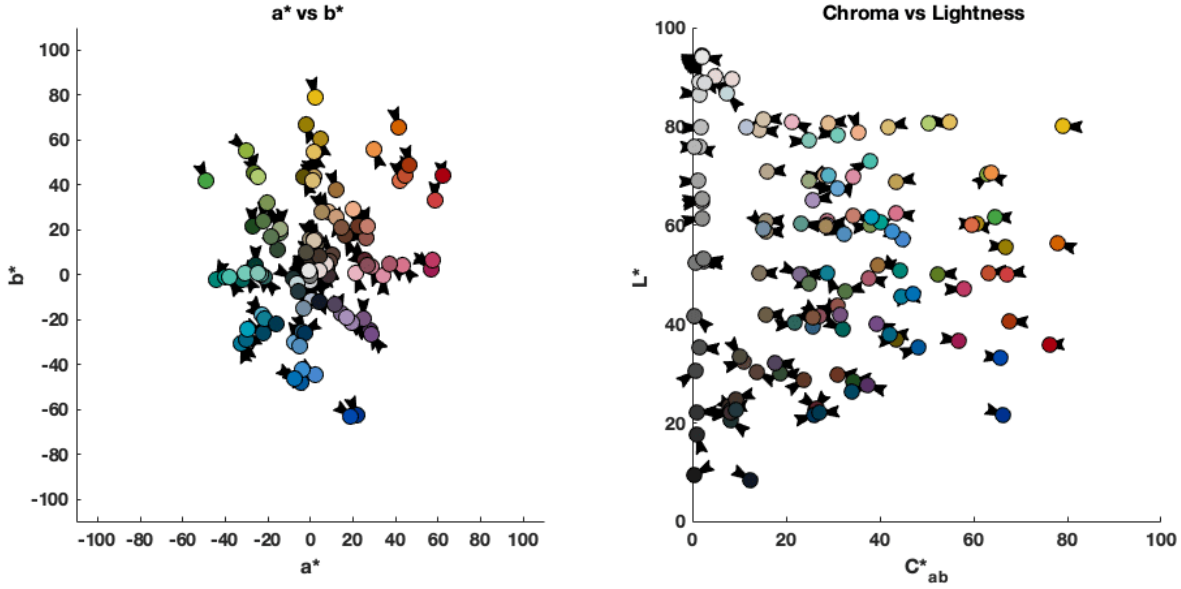

Figure 34. CIELAB a* vs. b* and L* vs. C^*_{ab} vector plots of the measured and predicted colorimetric data calculated from LED combination number 671.

4.4 Conclusions

The purpose of this chapter was to identify the optimal LED combination for multispectral imaging. In the previous chapter, the camera model was verified to be effective in predicting the camera signal. The predicted camera signal was then used to compute the tristimulus values and reflectance spectra of the target. The calculated tristimulus values and reflectance spectra were then compared to the measured tristimulus values and reflectance spectra. The Euclidean method and score ranking method were used to evaluate the Noise both in terms of total noise, *N* and noise in terms of lightness (ΔL), spectral and colorimetric accuracy of the LED combination. The GFC and Throughput were calculated as well to further evaluate the combinations. Four combinations were seen to kept recurring in the top combinations evaluated using the Euclidian method and score ranking method. All these combinations yielded excellent spectral and colorimetric accuracy and low noise (*N* and $N(\Delta L)$). Any of these combinations could be considered optimal. As such, any of the said combinations is recommended to be used in building a LED-based multispectral imaging system. If one must be chosen, the LED combination number 671 was seen to be slightly better than the other three with its ΔE_{00} (S_L=1), N (ΔL) and RMSE having slightly better values.

The results presented here were limited only to the use of a monochrome CCD camera and the LEDmotive system composed of 10 LEDs. The LEDmotive system isn't designed for multispectral imaging and was repurposed to fit that function. The camera type and number of LEDs are some factors discussed by Shrestha and Hardeberg (2014) that affect the performance of the LED-based multispectral imaging system. Furthermore, the sensors may not perform as optimal as presented here when used to capture novel surfaces. Since the target was modified to include pigments commonly used in artist's palette, the imaging system is designed to be used on multispectral imaging of artworks. A change of calibrated target is needed for other purposes. Changing the LEDs to encompass a broader wavelength spectrum could also increase its performance. The previous chapter also showed that the camera model was able to predict the color transformation noise accurately. This means that the simulation could also predict the noise due to color transformation accurately. Also, in the previous chapter, the actual camera signal incurred a lower colorimetric and spectral accuracy than the predicted camera signal; this could be from noise due to external factors during the imaging such as instrument or human error. This is important to consider in the future work involving the actual experimental testing of the optimal

combination, for which the actual LED imaging using optimum combination may not yield the exact values presented in the simulation.

Chapter 5: Conclusions and Future Research

This thesis introduced the use of LED illumination in multispectral imaging systems. The recent decade had shown vast developments in LED technology and a rise in LED manufacturing in the market. This technology can also be applied in current multispectral imaging systems replacing filter-based technology.

The thesis was subdivided into two parts. The first part dealt with the verification of a camera model capable of predicting camera signals using LEDmotive Technologies Spectra Tunelab coupled with a Finger Lakes Instrumentation panchromatic camera. The Spectra Tunelab uses 10 LEDs designed for lighting simulation. The current LED system showed a high spectral and color accuracy and relatively low color transformation noise. The camera model successfully predicted the camera signal with excellent linearity and subsequently accurately predicted the color transformation noise. As expected, external noise factored in the actual imaging process; as such it's colorimetric and spectral accuracy was slightly lower and not exactly the same as predicted. The MATLAB optimization tool *fminunc* was successful in minimizing the average color difference (ΔE_{00}) of the actual camera signal; however, the average color difference (ΔE_{00}) of the predicted camera signal stayed the same. This camera model is then used in the next portion of the research.

The choice of LEDs to be used in multispectral imaging system is an important decision when building an LED-based multispectral imaging system. The spectral and colorimetric accuracy are heavily influenced by the LED combinations used in the system. The second part of the research aimed in identifying the best LED combination among 37 LEDs available to LEDmotive Technologies. The spectral data provided by the manufacturer was used in the computational imaging simulation. An exhaustive search is computationally expensive and time consuming; thus, binning was applied to define the specific wavelength range of the LEDs. The binning substantially decreased the number of possible combinations from 348,330,136 to 110,592. The spectral reflectance Root-Mean-Square-Error (RMSE) was used as the metric to evaluate the spectral accuracy of the combinations. The top 1000 with the best RMSE value were evaluated further. In order to determine the optimum LED combination with a proper compromise among its noise and spectral and colorimetric accuracy, the Euclidean method and score ranking were both applied in evaluating the combinations. The GFC and Throughput were calculated as

well to further evaluate the combinations. The results showed four LED combinations with good spectral and colorimetric accuracy. Among the four, combination number 671 was slightly better with values of, 0.12 for average ΔE_{00}, 3.35 for total Noise, *N,* 1.22 for noise in terms of lightness (ΔL), 6.4 $x10^{-3}$ for RMSE, 0.97 for GFC and 646.85 for the total throughput. As such among all possible LED combinations, combination number 671 composed of LEDs number (and their peak wavelengths): 2(390 nm), 10(450 nm), 15(475 nm), 21(505 nm), 25(540 nm), 26(550 nm), 28(590 nm), 31(620 nm) , 33(660 nm), 37(745 nm) was chosen as the optimum LED combination.

There is still much to explore in building a LED-based multispectral imaging system. The next step involves the purchase of the LEDs chosen from the computational selection to build the LED-based multispectral imaging system and the comparison of the results from the computational imaging simulation to the actual imaging experimentation. Furthermore, other factors such as the type of camera and the target used should be explored in order to determine the best path to go in imaging using LEDs and the best LED system for specific materials may it be artworks or historical documents.

References

8 Advantages of LED Lighting. (n.d.). Retrieved February 9, 2020, from https://www.gecurrent.com/ideas/8-advantages-of-led-lighting

Abed, F. M. (2014). *Pigment identification of paintings based on Kubelka-Munk theory and spectral images.* Rochester, NY: Rochester Institute of Technology.

Berns, R. (2016). Modification of CIEDE2000 for assessing color quality of image archives. *Society for Imaging Science and Technology*, 181-185.

Berns, R. (2018). Practical UV-VIS-NIR Multispectral Imaging. *Archiving Conference* (pp. 47-52). Society for Imaging Science and Technology.

Berns, R. S. (2019). *Billmeyer and Saltzman's Principles of Color Technology.* New York: Wiley.

Berns, R. S., Imai, F. H., Burns, P. D., & Tzeng, D. Y. (1998). Multispectral-based color reproduction research at the Munsell Color Science Laboratory. *In Electronic Imaging: Processing, Printing, and Publishing in Color, 3409*, 14-26.

Berns, R., Taplin, L., & Nezamabadi, M. (2004). *Modifications of a sinarback 54 digital camera for spectral and high-accuracy colorimetric imaging: simulations and experiments.* Rochester Institute of Technology: Rochester,NY.

Berns, R., Taplin, L., & Nezamabadi, M. (2005). Spectral imaging using a commercial colour-filter array digital camera. *The Conservation Committee of the International Council of Museums (ICOM-CC)*.

Berns, Roy S. (2005). Color accurate image archives using spectral imaging. *Scientific Examination of Art: Modern Techniques in Conservation and Analysis*, 105-119.

Burns, P. D. and Berns, R. S. (1996). Analysis of multispectral image capture. *Proc. of the IS&T/SID Fourth Color Imaging Conference Color Science, Systems, and Applications* (pp. 19-22). Springfield, VA: IS&T.

Burns, P.D. (2002). Error Analysis for Digital Image Acquisition and Signal Processing. *Nippon Shashin Gakkai Nenji Taikai Koen Yoshi*, 320-321.

Burns, P.D., and Berns, R.S. (1997). Error propagation in color signal transformations. *Color Research and Application, 22*, 280–289.

Burns, P.D., and Berns, R.S. (83-85). Image noise and colorimetric precision in multispectral image capture. *IS&T/SID Sixth Color Imaging Conference.* 1998.

Burns, Peter. (1997). *Analysis of image noise in multispectral color acquisition.* Retrieved April 2020, 15, from https://scholarworks.rit.edu/cgi/viewcontent.cgi?article=5566&context=theses

Clark, R. (n.d.). *ClarkVision.com*. Retrieved April 15, 2020, from https://clarkvision.com/imagedetail/digital.sensor.performance.summary/

Coffey, Valerie C. (2012, April). *Multispectral Imaging Moves into the Mainstream.* Retrieved January 27, 2020, from https://www.osa-opn.org/home/articles/volume_23/issue_4/features/multispectral_imaging_moves_into_the_mainstream/

Cox, B. D., & Berns, R. S. (2015). Imaging artwork in a studio environment for computer graphics rendering. *International Society for Optics and Photonics, 9398*, 939803.

Dickinson, C. (2001). *Text segmentation of the Archimedes Palimpsest using remote sensing techniques.* Rochester Institute of Technology.

Easton, R. L., Christens-Barry, W. A., & Knox, K. T. (2011). Spectral image processing and analysis of the Archimedes Palimpsest. *9th European Signal Processing Conference* .

Easton, R. L., Christens-Barry, W. A., & Knox, K. T. (2011). *Ten years of lessons from imaging of the archimedes palimpsest.* Rochester,NY: Rochester Institute of Technology.

Easton, R., & Knox, K. (2004). Digital restoration of erased and damaged manuscripts. *Proceedings of the 39th Annual Convention of the Association of Jewish Libraries.* Brooklyn, NY.

Everdell N. L., Styles I. B., Claridge E., Hebden J. C., and Calcagni A. S. (2009). Multispectral imaging of the ocular fundus using LED illumination. *Novel Optical Instrumentation for Biomedical Applications IV, 7371*.

Fortunato, G. R. (2005). Old Masters' lead white pigments: investigations of paintings from the 16th to the 17th century using high precision lead isotope abundance ratios. *Analyst, 130*(6), 898-906.

Frost, J. (n.d.). *Statistics by Jim*. Retrieved March 12, 2020, from https://statisticsbyjim.com/regression/interpret-r-squared-regression/

Hansen, D. Michael. (2006). Multispectral imaging and analysis of the Archimedes Palimpsest. Rochester, New York: Rochester Institute of Technology.

Imai, F. H., & Berns, R. S. (2002). Spectral estimation of artist oil paints using multi- filter trichromatic imaging. *International Society for Optics and Photonics, 4421*, 504-508.

Imai, F. H., Rosen, M. R., & Berns, R. S. (2000). Comparison of spectrally narrow-band capture versus wide-band with a priori sample analysis for spectral reflectance estimation. *Society for Imaging Science and Technology, 2000*(1), 234-241.

Imai, F. H., Rosen, M. R., & Berns, R. S. (2001). Multi-spectral Imaging of a van Gogh's Self-portrait at the National Gallery of Art Washington DC. *PICS*, 185-189.

Imai, F.H., Rosen, M.R., &Berns, R.S. (2002). Comparative Study of Metrics for Spectral Match Quality. *Proceedings of the Conference on Colour in Graphics, Imaging, and Vision*, 492–496.

Kalajian, P. (2011). *Imaging Technique: Demystifying Flat Fields. Sky and telescope*. (Sky and Telescope) Retrieved November 12, 2019, from http://www.skyandtelescope.com/wp-content/uploads/documents/Flatfields+Mar11.pdf

Knox, K. T. (2008). Enhancement of overwritten text in the Archimedes Palimpsest. *International Society for Optics and Photonics, 6810*, 681004.

Knox, K. T., Dickinson, C., Wei, L., Easton Jr, R. L., & Johnston, R. H. (2001). Multispectral imaging of the Archimedes Palimpsest. *PICS.*

Kuniba, H., & Berns, R.S. (2008). The trade-off between color reproduction accuracy and image sensor noise. *IS&T/SID Sixteenth Color Imaging Conference.* Portland.

Kuniba, H., & Berns, R.S. (2009). Spectral sensitivity optimization of color image sensors considering photon shot noise. *Journal of Electronic Imaging, 18*, 023002-1–023002-14.

Kuzio, O., & Berns, R. S. (2019). *Color and Material Appearance Imaging and Archiving Using a Sony Alpha a7R III Camera.* Rochester, NY: Rochester Institute of Technology.

LEDMOTIVE. (n.d.). (Ledmotive Technologies) Retrieved March 29, 2020, from https://ledmotive.com/docs/DS_450003_rev05_SPECTRA_TUNE_LAB.pdf

Li, S. X. (2018). Filter Selection for Optimizing the Spectral Sensitivity of Broadband Multispectral Cameras Based on Maximum Linear Independence. *Sensors, 18*(5), 1455.

Mathworks. (n.d.). Retrieved November 15, 2019, from https://www.mathworks.com/help/ident/ref/goodnessoffit.html

MathWorks. (n.d.). Retrieved 25 March, 2020, from https://www.mathworks.com/help/gpucoder/examples/feature-extraction-using-surf.html

MathWorks. (n.d.). Retrieved April 12, 2020, from https://www.mathworks.com/help/optim/ug/fminunc.html

Multispectral and Hyperspectral Imaging. (n.d.). Retrieved February 9, 2020, from https://www.si.edu/MCIImagingStudio/Multispectral

Netz R., and Noel W. (2007). *The Archimedes Codex.* New York City: DaCapo Press.

Noise in photographic images. (2020). Retrieved April 15, 2020, from https://www.imatest.com/docs/noise/

Park, J.I., Lee M.H., Grossberg M.D.Z.D., and Nayar S.K. (n.d.). Multispectral imaging using multiplexed illumination. *IEEE International Conference on Computer Vision*.

Peery, T. R., & Messinger, D. (2018). Processes for conducting HSI and MSI pan-sharpening with 3D digital flattening. *Algorithms and Technologies for Multispectral, Hyperspectral, and Ultraspectral Imagery XXIV, 10644*, 106441W.

Peery, T. R., & Messinger, D. (2018). MSI vs. HSI in cultural heritage imaging. *Imaging Spectrometry XXII: Applications, Sensors, and Processing, 10768* , 107680G.

Peery, T. R., & Messinger, D. W. (2019). Panchromatic sharpening enabling low-intensity imaging of cultural heritage documents. *Image Sensing Technologies: Materials, Devices, Systems, and Applications VI, 10980*, 1098004.

Peery, Tyler R. (2019). *System Design Considerations for a Low-Intensity Hyperspectral Imager of Sensitive Cultural Heritage Manuscripts.* Rochester, NY: Rochester Institute of Technology.

Shrestha, R., & Hardeberg, J. Y. (2014). How are LED illumination based multispectral imaging systems influenced by different factors? *International Conference on Image and Signal Processing*, 61-71.

Shrestha, R., & Hardeberg, J. Y. (2013). LED matrix design for multispectral imaging. *The 12th International AIC Congress, 4*, 1317-1320.

Shrestha, R., & Hardeberg, J. Y. (2013). Multispectral imaging using LED illumination and an RGB camera. *Color and Imaging Conference-Society for Imaging Science and Technology, 2013*(1), 8-13.

Shrestha, R., & Hardeberg, J. Y. (2018). Assessment of two fast multispectral systems for imaging of a cultural heritage artifact-a Russian icon. *14th International Conference on Signal-Image Technology & Internet-Based Systems (SITIS).*

Shrestha, R., Hardeberg, J. Y., & Boust, C. (2012). LED based multispectral film scanner for accurate color imaging. *2012 Eighth International Conference on Signal Image Technology and Internet Based Systems* , 811-817.

Tareen, S. A. K., & Saleem, Z. (2018). A comparative analysis of sift, surf, kaze, akaze, orb, and brisk. *nternational conference on computing, mathematics and engineering technologies.*

The Archimedes Palimpsest. (n.d.). Retrieved 29 January, 2020, from http://archimedespalimpsest.org/about/

Walowit, E., Mccarthy, C. J., & Berns, R. S. (1987). An algorithm for the optimization of kubelka-munk absorption and scattering coefficients. *Color Research & Application, 12*(6), 340- 343.

Walvoord, D. J. (2008). *Advanced correlation-based character recognition applied to the Archimedes Palimpsest.* Rochester,NY: Rochester Institute of Technology.

Walvoord, D. J., & Easton, R. L. (2008). Digital transcription of the archimedes palimpsest. *IEEE Signal Processing Magazine, 25*(4), 100-104.

Wang, Y. (2016, August 2019). *Design and Construction of a Multispectral Camera for Spectral and Colorimetric Reproduction.* Retrieved from Rochester Institute of Technology.: https://scholarworks.rit.edu/cgi/viewcontent.cgi?article=10468&context=theses

Wang, Y., & Berns, R. S. (2017). Filter Selection for Multispectral Imaging Optimizing Spectral, Colorimetric and Image Quality. *Electronic Imaging, 2017*(11), 25-32.

Wong, L. and Trentelman, K. (2017). *Imaging in Conservation*. (The Getty Conservation Institute) Retrieved February 9, 2020, from httpås://www.getty.edu/conservation/publications_resources/newsletters/pdf/v32n1.pdf

Wyszecki, G. (1953). Psychophysical investigation of relationship between normal and abnormal trichromatic vision. *Farbe, 2*(39).

Yamamoto, S., Tsumura, N., Nakaguchi, T., & Miyake, Y. (2007). Development of a multi-spectral scanner using LED array for digital color proof. *Journal of Imaging Science and Technology, 51*(9), 61-69.

Zhao, Y., & Berns, R. S. (2007). Image-based spectral reflectance reconstruction using the matrix R method. *Color Research & Application, 32*(5), 343-351.

Zhao, Y., Berns, R. S., Taplin, L. A., & Coddington, J. (2008). An investigation of multispectral imaging for the mapping of pigments in paintings. *International Society for Optics and Photonics, 6810*, 681007.

Appendix A: Spectral Power Distribution of the LEDs

Table 6. LEDS in LED Bin number 1 with their corresponding Spectral Power Distribution.

Wavelength (nm)	1	2	3	4	5	6	7	8	9
380	0.5000059	0.062503	0.0057673	0.0001046	5.90E-06	4.00E-07	0	0	0
385	1	0.5000059	0.1011292	0.0057673	0.0004521	3.52E-05	3.00E-06	0	0.0013473
390	0.5000059	1	0.5639221	0.1011292	0.01314	0.0014127	0.0001447	3.00E-06	0.004679
395	0.062503	0.5000059	1	0.5639221	0.1458209	0.0249407	0.0034886	0.0001447	0.0109487
400	0.0019533	0.062503	0.5639221	1	0.6179523	0.193872	0.0414709	0.0034886	0.0293259
405	1.53E-05	0.0019533	0.1011292	0.5639221	1	0.6635578	0.243032	0.0414709	0.0695775
410	0	1.53E-05	0.0057673	0.1011292	0.6179523	1	0.7021273	0.243032	0.1675344
415	0	0	0.0001046	0.0057673	0.1458209	0.6635578	1	0.7021273	0.3792771
420	0	0	6.00E-07	0.0001046	0.01314	0.193872	0.7021273	1	0.7685958
425	0	0	0	6.00E-07	0.0004521	0.0249407	0.243032	0.7021273	1
430	0	0	0	0	5.90E-06	0.0014127	0.0414709	0.243032	0.6917063
435	0	0	0	0	0	3.52E-05	0.0034886	0.0414709	0.3521574
440	0	0	0	0	0	4.00E-07	0.0001447	0.0034886	0.1881943
445	0	0	0	0	0	0	3.00E-06	0.0001447	0.0929347
450	0	0	0	0	0	0	0	3.00E-06	0.04834
455	0	0	0	0	0	0	0	0	0.0249435
460	0	0	0	0	0	0	0	0	0.0113397
465	0	0	0	0	0	0	0	0	0.006522
470	0	0	0	0	0	0	0	0	0.0034791
475	0	0	0	0	0	0	0	0	0.0034791
480	0	0	0	0	0	0	0	0	0.0034791
485	0	0	0	0	0	0	0	0	0.0034791
490	0	0	0	0	0	0	0	0	0.0034791
495	0	0	0	0	0	0	0	0	0.0034791
500	0	0	0	0	0	0	0	0	0.0034791
505	0	0	0	0	0	0	0	0	0.0034791
510	0	0	0	0	0	0	0	0	0.0034791
515	0	0	0	0	0	0	0	0	0.0034791
520	0	0	0	0	0	0	0	0	0.0034791
525	0	0	0	0	0	0	0	0	0.0034791
530	0	0	0	0	0	0	0	0	0.0034791
535	0	0	0	0	0	0	0	0	0.0034791
540	0	0	0	0	0	0	0	0	0.0034791
545	0	0	0	0	0	0	0	0	0.0034791
550	0	0	0	0	0	0	0	0	0.0034791
555	0	0	0	0	0	0	0	0	0.0034791
560	0	0	0	0	0	0	0	0	0.0034791
565	0	0	0	0	0	0	0	0	0.0034791
570	0	0	0	0	0	0	0	0	0.0034791
575	0	0	0	0	0	0	0	0	0.0034791
580	0	0	0	0	0	0	0	0	0.0034791
585	0	0	0	0	0	0	0	0	0.0034791
590	0	0	0	0	0	0	0	0	0.0034791
595	0	0	0	0	0	0	0	0	0.0034791
600	0	0	0	0	0	0	0	0	0.0034791
605	0	0	0	0	0	0	0	0	0.0034791
610	0	0	0	0	0	0	0	0	0.0034791
615	0	0	0	0	0	0	0	0	0.0034791
620	0	0	0	0	0	0	0	0	0.0034791
625	0	0	0	0	0	0	0	0	0.0034791
630	0	0	0	0	0	0	0	0	0.0034791
635	0	0	0	0	0	0	0	0	0.0034791
640	0	0	0	0	0	0	0	0	0.0034791
645	0	0	0	0	0	0	0	0	0.0034791
650	0	0	0	0	0	0	0	0	0.0034791
655	0	0	0	0	0	0	0	0	0.0034791
660	0	0	0	0	0	0	0	0	0.0034791

665	0	0	0	0	0	0	0	0	0.0034791
670	0	0	0	0	0	0	0	0	0.0034791
675	0	0	0	0	0	0	0	0	0.0034791
680	0	0	0	0	0	0	0	0	0.0034791
685	0	0	0	0	0	0	0	0	0.0034791
690	0	0	0	0	0	0	0	0	0.0034791
695	0	0	0	0	0	0	0	0	0.0034791
700	0	0	0	0	0	0	0	0	0.0034791
705	0	0	0	0	0	0	0	0	0.0034791
710	0	0	0	0	0	0	0	0	0.0034791
715	0	0	0	0	0	0	0	0	0.0034791
720	0	0	0	0	0	0	0	0	0.0034791
725	0	0	0	0	0	0	0	0	0.0034791
730	0	0	0	0	0	0	0	0	0.0034791
735	0	0	0	0	0	0	0	0	0.0034791
740	0	0	0	0	0	0	0	0	0.0034791
745	0	0	0	0	0	0	0	0	0.0034791
750	0	0	0	0	0	0	0	0	0.0034791
755	0	0	0	0	0	0	0	0	0.0034791
760	0	0	0	0	0	0	0	0	0.0034791
765	0	0	0	0	0	0	0	0	0.0034791
770	0	0	0	0	0	0	0	0	0.0034791
775	0	0	0	0	0	0	0	0	0.0034791
780	0	0	0	0	0	0	0	0	0.0034791

Table 7. LEDS in LED Bin number 2 with their corresponding Spectral Power Distribution.

Wavelength (nm)	10	11	12	13
380	0	0	0	0
385	0	0	0	0
390	0	0	0	0
395	0	0	0	0
400	0	0	0	0
405	0.0013838	0	0	0
410	0.0057108	0.0013838	0	0
415	0.0228167	0.0057108	0.0013838	0.0017145
420	0.0562389	0.0228167	0.0057108	0.0101392
425	0.1241239	0.0562389	0.0228167	0.025979
430	0.2573025	0.1241239	0.0562389	0.0546557
435	0.4621028	0.2573025	0.1241239	0.1112471
440	0.7000729	0.4621028	0.2573025	0.1890346
445	0.9632841	0.7000729	0.4621028	0.3214791
450	0.9700176	0.9632841	0.7000729	0.5126928
455	0.6801326	0.9700176	0.9632841	0.7506241
460	0.4027936	0.6801326	0.9700176	0.9695801
465	0.2496753	0.4027936	0.6801326	0.9844903
470	0.1446285	0.2496753	0.4027936	0.7907094
475	0.0871068	0.1446285	0.2496753	0.5522635
480	0.0433631	0.0871068	0.1446285	0.3689929
485	0.0268942	0.0433631	0.0871068	0.2500286
490	0.0153022	0.0268942	0.0433631	0.1576601
495	0.0087984	0.0153022	0.0268942	0.1010864
500	0.0058467	0.0087984	0.0153022	0.0624335
505	0.0015757	0.0058467	0.0087984	0.042771
510	0.000751	0.0015757	0.0058467	0.0269646

515	0.000751	0.000751	0.0015757	0.0180559
520	0.000751	0.000751	0.000751	0.0097557
525	0.000751	0.000751	0.000751	0.0055357
530	0.000751	0.000751	0.000751	0.0021395
535	0.000751	0.000751	0.000751	0.0019487
540	0.000751	0.000751	0.000751	0.0019487
545	0.000751	0.000751	0.000751	0.0019487
550	0.000751	0.000751	0.000751	0.0019487
555	0.000751	0.000751	0.000751	0.0019487
560	0.000751	0.000751	0.000751	0.0019487
565	0.000751	0.000751	0.000751	0.0019487
570	0.000751	0.000751	0.000751	0.0019487
575	0.000751	0.000751	0.000751	0.0019487
580	0.000751	0.000751	0.000751	0.0019487
585	0.000751	0.000751	0.000751	0.0019487
590	0.000751	0.000751	0.000751	0.0019487
595	0.000751	0.000751	0.000751	0.0019487
600	0.000751	0.000751	0.000751	0.0019487
605	0.000751	0.000751	0.000751	0.0019487
610	0.000751	0.000751	0.000751	0.0019487
615	0.000751	0.000751	0.000751	0.0019487
620	0.000751	0.000751	0.000751	0.0019487
625	0.000751	0.000751	0.000751	0.0019487
630	0.000751	0.000751	0.000751	0.0019487
635	0.000751	0.000751	0.000751	0.0019487
640	0.000751	0.000751	0.000751	0.0019487
645	0.000751	0.000751	0.000751	0.0019487
650	0.000751	0.000751	0.000751	0.0019487
655	0.000751	0.000751	0.000751	0.0019487
660	0.000751	0.000751	0.000751	0.0019487
665	0.000751	0.000751	0.000751	0.0019487
670	0.000751	0.000751	0.000751	0.0019487
675	0.000751	0.000751	0.000751	0.0019487
680	0.000751	0.000751	0.000751	0.0019487
685	0.000751	0.000751	0.000751	0.0019487
690	0.000751	0.000751	0.000751	0.0019487
695	0.000751	0.000751	0.000751	0.0019487
700	0.000751	0.000751	0.000751	0.0019487
705	0.000751	0.000751	0.000751	0.0019487
710	0.000751	0.000751	0.000751	0.0019487
715	0.000751	0.000751	0.000751	0.0019487
720	0.000751	0.000751	0.000751	0.0019487
725	0.000751	0.000751	0.000751	0.0019487
730	0.000751	0.000751	0.000751	0.0019487
735	0.000751	0.000751	0.000751	0.0019487
740	0.000751	0.000751	0.000751	0.0019487
745	0.000751	0.000751	0.000751	0.0019487
750	0.000751	0.000751	0.000751	0.0019487
755	0.000751	0.000751	0.000751	0.0019487
760	0.000751	0.000751	0.000751	0.0019487
765	0.000751	0.000751	0.000751	0.0019487
770	0.000751	0.000751	0.000751	0.0019487
775	0.000751	0.000751	0.000751	0.0019487

780	0.000751	0.000751	0.000751	0.0019487

Table 8. LEDS in LED Bin number 3 with their corresponding Spectral Power Distribution.

Wavelength (nm)	14	15	16	17
380	0	0	0	0
385	0	0	0	0
390	0	0	0	0
395	0	0	0	0
400	0	0	0	0
405	0	0	0	0
410	0	0	0	0
415	0	0	0	0
420	0.0017145	0	0	0
425	0.0101392	0.0017145	0	0
430	0.025979	0.0101392	0.0017145	0
435	0.0546557	0.025979	0.0101392	0.0017145
440	0.1112471	0.0546557	0.025979	0.0101392
445	0.1890346	0.1112471	0.0546557	0.025979
450	0.3214791	0.1890346	0.1112471	0.0546557
455	0.5126928	0.3214791	0.1890346	0.1112471
460	0.7506241	0.5126928	0.3214791	0.1890346
465	0.9695801	0.7506241	0.5126928	0.3214791
470	0.9844903	0.9695801	0.7506241	0.5126928
475	0.7907094	0.9844903	0.9695801	0.7506241
480	0.5522635	0.7907094	0.9844903	0.9695801
485	0.3689929	0.5522635	0.7907094	0.9844903
490	0.2500286	0.3689929	0.5522635	0.7907094
495	0.1576601	0.2500286	0.3689929	0.5522635
500	0.1010864	0.1576601	0.2500286	0.3689929
505	0.0624335	0.1010864	0.1576601	0.2500286
510	0.042771	0.0624335	0.1010864	0.1576601
515	0.0269646	0.042771	0.0624335	0.1010864
520	0.0180559	0.0269646	0.042771	0.0624335
525	0.0097557	0.0180559	0.0269646	0.042771
530	0.0055357	0.0097557	0.0180559	0.0269646
535	0.0021395	0.0055357	0.0097557	0.0180559
540	0.0019487	0.0021395	0.0055357	0.0097557
545	0.0019487	0.0019487	0.0021395	0.0055357
550	0.0019487	0.0019487	0.0019487	0.0021395
555	0.0019487	0.0019487	0.0019487	0.0019487
560	0.0019487	0.0019487	0.0019487	0.0019487
565	0.0019487	0.0019487	0.0019487	0.0019487
570	0.0019487	0.0019487	0.0019487	0.0019487
575	0.0019487	0.0019487	0.0019487	0.0019487
580	0.0019487	0.0019487	0.0019487	0.0019487
585	0.0019487	0.0019487	0.0019487	0.0019487
590	0.0019487	0.0019487	0.0019487	0.0019487
595	0.0019487	0.0019487	0.0019487	0.0019487
600	0.0019487	0.0019487	0.0019487	0.0019487

605	0.0019487	0.0019487	0.0019487	0.0019487
610	0.0019487	0.0019487	0.0019487	0.0019487
615	0.0019487	0.0019487	0.0019487	0.0019487
620	0.0019487	0.0019487	0.0019487	0.0019487
625	0.0019487	0.0019487	0.0019487	0.0019487
630	0.0019487	0.0019487	0.0019487	0.0019487
635	0.0019487	0.0019487	0.0019487	0.0019487
640	0.0019487	0.0019487	0.0019487	0.0019487
645	0.0019487	0.0019487	0.0019487	0.0019487
650	0.0019487	0.0019487	0.0019487	0.0019487
655	0.0019487	0.0019487	0.0019487	0.0019487
660	0.0019487	0.0019487	0.0019487	0.0019487
665	0.0019487	0.0019487	0.0019487	0.0019487
670	0.0019487	0.0019487	0.0019487	0.0019487
675	0.0019487	0.0019487	0.0019487	0.0019487
680	0.0019487	0.0019487	0.0019487	0.0019487
685	0.0019487	0.0019487	0.0019487	0.0019487
690	0.0019487	0.0019487	0.0019487	0.0019487
695	0.0019487	0.0019487	0.0019487	0.0019487
700	0.0019487	0.0019487	0.0019487	0.0019487
705	0.0019487	0.0019487	0.0019487	0.0019487
710	0.0019487	0.0019487	0.0019487	0.0019487
715	0.0019487	0.0019487	0.0019487	0.0019487
720	0.0019487	0.0019487	0.0019487	0.0019487
725	0.0019487	0.0019487	0.0019487	0.0019487
730	0.0019487	0.0019487	0.0019487	0.0019487
735	0.0019487	0.0019487	0.0019487	0.0019487
740	0.0019487	0.0019487	0.0019487	0.0019487
745	0.0019487	0.0019487	0.0019487	0.0019487
750	0.0019487	0.0019487	0.0019487	0.0019487
755	0.0019487	0.0019487	0.0019487	0.0019487
760	0.0019487	0.0019487	0.0019487	0.0019487
765	0.0019487	0.0019487	0.0019487	0.0019487
770	0.0019487	0.0019487	0.0019487	0.0019487
775	0.0019487	0.0019487	0.0019487	0.0019487
780	0.0019487	0.0019487	0.0019487	0.0019487

Table 9. LEDS in LED Bin number 4 with their corresponding Spectral Power Distribution.

Wavelength (nm)	18	19	20	21
380	0.0004459	0.0004459	0.000447	0.000447
385	0.0004459	0.0004459	0.000447	0.000447
390	0.0004459	0.0004459	0.000447	0.000447
395	0.0004459	0.0004459	0.000447	0.000447
400	0.0004459	0.0004459	0.000447	0.000447
405	0.0004459	0.0004459	0.000447	0.000447
410	0.0004459	0.0004459	0.000447	0.000447
415	0.0004459	0.0004459	0.000447	0.000447
420	0.0004459	0.0004459	0.000447	0.000447
425	0.0004459	0.0004459	0.000447	0.000447

430	0.0004459	0.0004459	0.000447	0.000447
435	0.0004459	0.0004459	0.000447	0.000447
440	0.0033467	0.0004459	0.000447	0.000447
445	0.0120892	0.0033467	0.000447	0.000447
450	0.0237491	0.0120892	0.004231	0.000447
455	0.0509745	0.0237491	0.0129943	0.004231
460	0.1037313	0.0509745	0.025165	0.0129943
465	0.1689657	0.1037313	0.0549322	0.025165
470	0.2740038	0.1689657	0.1087953	0.0549322
475	0.4719999	0.2740038	0.1789894	0.1087953
480	0.6502729	0.4719999	0.2875887	0.1789894
485	0.8727617	0.6502729	0.4850407	0.2875887
490	0.9887172	0.8727617	0.6733103	0.4850407
495	0.9709666	0.9887172	0.8884704	0.6733103
500	0.8233862	0.9709666	0.9943452	0.8884704
505	0.6537129	0.8233862	0.9624869	0.9943452
510	0.4895944	0.6537129	0.8100733	0.9624869
515	0.3622022	0.4895944	0.6336116	0.8100733
520	0.2637525	0.3622022	0.4768331	0.6336116
525	0.1825603	0.2637525	0.3532429	0.4768331
530	0.1222493	0.1825603	0.2551759	0.3532429
535	0.0859725	0.1222493	0.1759361	0.2551759
540	0.0579103	0.0859725	0.1184724	0.1759361
545	0.038208	0.0579103	0.0827193	0.1184724
550	0.0254942	0.038208	0.0560734	0.0827193
555	0.0158688	0.0254942	0.0363242	0.0560734
560	0.0081198	0.0158688	0.0245901	0.0363242
565	0.0045974	0.0081198	0.0149417	0.0245901
570	0.0010751	0.0045974	0.007786	0.0149417
575	0	0.0010751	0.0042553	0.007786
580	0	0	0.0007246	0.0042553
585	0	0	0	0.0007246
590	0	0	0	0
595	0	0	0	0
600	0	0	0	0
605	0	0	0	0
610	0	0	0	0
615	0	0	0	0
620	0	0	0	0
625	0	0	0	0
630	0	0	0	0
635	0	0	0	0
640	0	0	0	0
645	0	0	0	0
650	0	0	0	0
655	0	0	0	0
660	0	0	0	0
665	0	0	0	0
670	0	0	0	0
675	0	0	0	0
680	0	0	0	0
685	0	0	0	0
690	0	0	0	0

695	0	0	0	0
700	0	0	0	0
705	0	0	0	0
710	0	0	0	0
715	0	0	0	0
720	0	0	0	0
725	0	0	0	0
730	0	0	0	0
735	0	0	0	0
740	0	0	0	0
745	0	0	0	0
750	0	0	0	0
755	0	0	0	0
760	0	0	0	0
765	0	0	0	0
770	0	0	0	0
775	0	0	0	0
780	0	0	0	0

Table 10. LEDS in LED Bin number 5 with their corresponding Spectral Power Distribution.

Wavelength (nm)	**22**	**23**	**24**	**25**
380	0	0	0	0
385	0	0	0	0
390	0	0	0	0
395	0	0	0	0
400	0	0	0	0
405	0	0	0	0
410	0	0	0	0
415	0	0	0	0
420	0	0	0	0
425	0	0	0	0
430	0	0	0	0
435	0	0	0	0
440	0	0	0	0
445	0	0	0	0
450	0	0	0	0
455	0	0	0	0
460	0	0	0	0
465	0.0034568	0	0	0
470	0.0104847	0.0034568	0	0
475	0.0190471	0.0104847	0.0034568	0
480	0.0375786	0.0190471	0.0104847	0.0034568
485	0.065009	0.0375786	0.0190471	0.0104847
490	0.1110855	0.065009	0.0375786	0.0190471
495	0.1822541	0.1110855	0.065009	0.0375786
500	0.2906023	0.1822541	0.1110855	0.065009
505	0.4401173	0.2906023	0.1822541	0.1110855
510	0.6214055	0.4401173	0.2906023	0.1822541
515	0.8377835	0.6214055	0.4401173	0.2906023

520	0.9808225	0.8377835	0.6214055	0.4401173
525	0.9842228	0.9808225	0.8377835	0.6214055
530	0.9085532	0.9842228	0.9808225	0.8377835
535	0.7456123	0.9085532	0.9842228	0.9808225
540	0.5839115	0.7456123	0.9085532	0.9842228
545	0.4448533	0.5839115	0.7456123	0.9085532
550	0.331212	0.4448533	0.5839115	0.7456123
555	0.242932	0.331212	0.4448533	0.5839115
560	0.1736391	0.242932	0.331212	0.4448533
565	0.1225225	0.1736391	0.242932	0.331212
570	0.0866046	0.1225225	0.1736391	0.242932
575	0.0595398	0.0866046	0.1225225	0.1736391
580	0.0424797	0.0595398	0.0866046	0.1225225
585	0.0287361	0.0424797	0.0595398	0.0866046
590	0.019561	0.0287361	0.0424797	0.0595398
595	0.0142208	0.019561	0.0287361	0.0424797
600	0.0093716	0.0142208	0.019561	0.0287361
605	0.0052992	0.0093716	0.0142208	0.019561
610	0.002159	0.0052992	0.0093716	0.0142208
615	0.002159	0.002159	0.0052992	0.0093716
620	0.002159	0.002159	0.002159	0.0052992
625	0.002159	0.002159	0.002159	0.002159
630	0.002159	0.002159	0.002159	0.002159
635	0.002159	0.002159	0.002159	0.002159
640	0.002159	0.002159	0.002159	0.002159
645	0.002159	0.002159	0.002159	0.002159
650	0.002159	0.002159	0.002159	0.002159
655	0.002159	0.002159	0.002159	0.002159
660	0.002159	0.002159	0.002159	0.002159
665	0.002159	0.002159	0.002159	0.002159
670	0.002159	0.002159	0.002159	0.002159
675	0.002159	0.002159	0.002159	0.002159
680	0.002159	0.002159	0.002159	0.002159
685	0.002159	0.002159	0.002159	0.002159
690	0.002159	0.002159	0.002159	0.002159
695	0.002159	0.002159	0.002159	0.002159
700	0.002159	0.002159	0.002159	0.002159
705	0.002159	0.002159	0.002159	0.002159
710	0.002159	0.002159	0.002159	0.002159
715	0.002159	0.002159	0.002159	0.002159
720	0.002159	0.002159	0.002159	0.002159
725	0.002159	0.002159	0.002159	0.002159
730	0.002159	0.002159	0.002159	0.002159
735	0.002159	0.002159	0.002159	0.002159
740	0.002159	0.002159	0.002159	0.002159
745	0.002159	0.002159	0.002159	0.002159
750	0.002159	0.002159	0.002159	0.002159
755	0.002159	0.002159	0.002159	0.002159
760	0.002159	0.002159	0.002159	0.002159
765	0.002159	0.002159	0.002159	0.002159
770	0.002159	0.002159	0.002159	0.002159
775	0.002159	0.002159	0.002159	0.002159
780	0.002159	0.002159	0.002159	0.002159

Table 11. LEDS in LED Bin number 6 with their corresponding Spectral Power Distribution.

Wavelength (nm)	26
380	0
385	0
390	0
395	0
400	0
405	0
410	0.0057703
415	0.015122
420	0.0243425
425	0.0332784
430	0.0422143
435	0.0442435
440	0.0460736
445	0.0494731
450	0.0570115
455	0.0731214
460	0.0782124
465	0.079115
470	0.0783998
475	0.0853017
480	0.0949355
485	0.1142346
490	0.1534182
495	0.2138512
500	0.3042287
505	0.4599174
510	0.5891308
515	0.7273645
520	0.8271721
525	0.9007874
530	0.9511244
535	0.9787518
540	0.9900828
545	0.997133
550	0.9987219
555	0.9923198
560	0.9784933
565	0.9616917
570	0.9374922
575	0.9089279
580	0.8710351
585	0.8324706
590	0.7964756

595	0.7598956
600	0.7101592
605	0.6572139
610	0.6185026
615	0.5699377
620	0.5213412
625	0.4786178
630	0.4373978
635	0.3902303
640	0.3527132
645	0.3197488
650	0.2872473
655	0.2560221
660	0.2275427
665	0.2008943
670	0.1789149
675	0.1598522
680	0.1428433
685	0.1258344
690	0.1106705
695	0.0962142
700	0.0829596
705	0.0725924
710	0.0631554
715	0.054966
720	0.0470934
725	0.0411355
730	0.0351776
735	0.0295951
740	0.0244634
745	0.0194651
750	0.0160467
755	0.0126283
760	0.0101844
765	0.007762
770	0.0053395
775	0.002917
780	0.0020968

Table 12. LEDS in LED Bin number 7 with their corresponding Spectral Power Distribution.

Wavelength (nm)	27	28	29	30
380	0.0028143	0	0	0
385	0.0028143	0	0	0
390	0.0028143	0	0	0

395	0.0028143	0	0	0
400	0.0028143	0	0	0
405	0.0028143	0	0	0
410	0.0028143	0	0	0
415	0.0028143	0	0	0
420	0.0028143	0	0	0
425	0.0028143	0	0	0
430	0.0028143	0	0	0
435	0.0035679	0	0	0
440	0.0045836	0	0	0
445	0.0059688	0	0	0
450	0.0069398	0	0	0
455	0.0047989	0	0	0
460	0.0041213	0	0	0
465	0.0034437	0	0	0
470	0.0028749	0	0	0
475	0.0024344	0	0	0
480	0.001919	0	0	0
485	0.0010792	0	0	0
490	0.0002394	0	0	0
495	0.0003879	0	0	0
500	0.0009305	0	0	0
505	0.001673	0	0	0
510	0.0025621	0	0	0
515	0.0037608	0	0	0
520	0.012739	0	0	0
525	0.0250201	0	0	0
530	0.037829	0	0	0
535	0.0634007	0.0002734	0	0
540	0.1005245	0.0011052	0.0003266	0
545	0.1579271	0.003089	0.0012772	0.0003266
550	0.2302895	0.0113149	0.0034296	0.0012772
555	0.3306972	0.0311228	0.012111	0.0034296
560	0.4427057	0.0576309	0.033446	0.012111
565	0.5669306	0.1041412	0.060652	0.033446
570	0.6892839	0.1844303	0.1101094	0.060652
575	0.8016381	0.3333813	0.194272	0.1101094
580	0.8896761	0.560884	0.3457644	0.194272
585	0.951932	0.8790537	0.5833463	0.3457644
590	0.982468	0.9761816	0.908087	0.5833463
595	0.9982211	0.5542415	0.9526663	0.908087
600	0.9856277	0.2053794	0.5027983	0.9526663
605	0.9608752	0.0757046	0.1800416	0.5027983
610	0.9181294	0.0282248	0.067282	0.1800416
615	0.8643704	0.009575	0.0244934	0.067282
620	0.8002715	0.0036031	0.0087375	0.0244934
625	0.7352642	0.0020223	0.0030072	0.0087375
630	0.6714974	0.0020223	0.0020094	0.0030072
635	0.6093974	0.0020223	0.0020094	0.0020094
640	0.5337334	0.0020223	0.0020094	0.0020094
645	0.4791172	0.0020223	0.0020094	0.0020094
650	0.4236659	0.0020223	0.0020094	0.0020094
655	0.3725011	0.0020223	0.0020094	0.0020094

660	0.3243902	0.0020223	0.0020094	0.0020094
665	0.2826047	0.0020223	0.0020094	0.0020094
670	0.2444315	0.0020223	0.0020094	0.0020094
675	0.2126384	0.0020223	0.0020094	0.0020094
680	0.1816026	0.0020223	0.0020094	0.0020094
685	0.1574375	0.0020223	0.0020094	0.0020094
690	0.1356272	0.0020223	0.0020094	0.0020094
695	0.1164603	0.0020223	0.0020094	0.0020094
700	0.0993245	0.0020223	0.0020094	0.0020094
705	0.0848176	0.0020223	0.0020094	0.0020094
710	0.0735504	0.0020223	0.0020094	0.0020094
715	0.0627572	0.0020223	0.0020094	0.0020094
720	0.0554329	0.0020223	0.0020094	0.0020094
725	0.0481086	0.0020223	0.0020094	0.0020094
730	0.0417924	0.0020223	0.0020094	0.0020094
735	0.0357386	0.0020223	0.0020094	0.0020094
740	0.0309034	0.0020223	0.0020094	0.0020094
745	0.0274585	0.0020223	0.0020094	0.0020094
750	0.0241366	0.0020223	0.0020094	0.0020094
755	0.0215617	0.0020223	0.0020094	0.0020094
760	0.0189869	0.0020223	0.0020094	0.0020094
765	0.0168246	0.0020223	0.0020094	0.0020094
770	0.0147554	0.0020223	0.0020094	0.0020094
775	0.0127811	0.0020223	0.0020094	0.0020094
780	0.0109053	0.0020223	0.0020094	0.0020094

Table 13. LEDS in LED Bin number 8 with their corresponding Spectral Power Distribution.

Wavelength (nm)	**31**	**32**
380	0.0009202	0
385	0.0009202	0
390	0.0009202	0
395	0.0009202	0
400	0.0009202	0
405	0.0009202	0
410	0.0009202	0
415	0.0009202	0
420	0.0009202	0
425	0.0009202	0
430	0.0009202	0
435	0.0009202	0
440	0.0009202	0
445	0.0009202	0
450	0.0009202	0
455	0.0009202	0
460	0.0009202	0
465	0.0009202	0
470	0.0009202	0
475	0.0009202	0
480	0.0009202	0

485	0.0009202	0
490	0.0009202	0
495	0.0009202	0
500	0.0009202	0
505	0.0009202	0
510	0.0009202	0
515	0.0009202	0
520	0.0009202	0
525	0.0009202	0
530	0.0009202	0
535	0.0009202	0
540	0.0009202	0
545	0.0009202	0
550	0.0009202	0
555	0.0009202	0
560	0.0009202	0
565	0.0009202	0
570	0.0009202	0
575	0.0056361	0.0017018
580	0.0181637	0.0040549
585	0.0383748	0.0073847
590	0.0764148	0.0143748
595	0.1325814	0.0247863
600	0.2095235	0.0394249
605	0.3554068	0.0721829
610	0.5472889	0.1131777
615	0.809433	0.1836537
620	0.9925338	0.2857109
625	0.8129237	0.4257162
630	0.3464567	0.6299856
635	0.136619	0.89565
640	0.0453744	0.9881243
645	0.0135816	0.6476059
650	0	0.2597937
655	0	0.1253738
660	0	0.0493517
665	0	0.0231488
670	0	0.0087275
675	0	0.0062336
680	0	0.0062336
685	0	0.0062336
690	0	0.0062336
695	0	0.0062336
700	0	0.0062336
705	0	0.0062336
710	0	0.0062336
715	0	0.0062336
720	0	0.0062336
725	0	0.0062336
730	0	0.0062336
735	0	0.0062336
740	0	0.0062336
745	0	0.0062336

750	0	0.0062336
755	0	0.0062336
760	0	0.0062336
765	0	0.0062336
770	0	0.0062336
775	0	0.0062336
780	0	0.0062336

Table 14. LEDS in LED Bin number 9 with their corresponding Spectral Power Distribution.

Wavelength (nm)	33	34
380	0.0054184	0.0054184
385	0.0054184	0.0054184
390	0.0054184	0.0054184
395	0.0054184	0.0054184
400	0.0054184	0.0054184
405	0.0054184	0.0054184
410	0.0054184	0.0054184
415	0.0054184	0.0054184
420	0.0054184	0.0054184
425	0.0054184	0.0054184
430	0.0054184	0.0054184
435	0.0054184	0.0054184
440	0.0054184	0.0054184
445	0.0054184	0.0054184
450	0.0054184	0.0054184
455	0.0054184	0.0054184
460	0.0054184	0.0054184
465	0.0054184	0.0054184
470	0.0054184	0.0054184
475	0.0054184	0.0054184
480	0.0054184	0.0054184
485	0.0054184	0.0054184
490	0.0054184	0.0054184
495	0.0054184	0.0054184
500	0.0054184	0.0054184
505	0.0054184	0.0054184
510	0.0054184	0.0054184
515	0.0054184	0.0054184
520	0.0054184	0.0054184
525	0.0054184	0.0054184
530	0.0054184	0.0054184
535	0.0054184	0.0054184
540	0.0054184	0.0054184
545	0.0054184	0.0054184
550	0.0054184	0.0054184
555	0.0054184	0.0054184
560	0.0054184	0.0054184
565	0.0054184	0.0054184
570	0.0054184	0.0054184

575	0.0054184	0.0054184
580	0.0054184	0.0054184
585	0.0054184	0.0054184
590	0.0054184	0.0054184
595	0.0054184	0.0054184
600	0.0073626	0.0054184
605	0.0128388	0.0054184
610	0.0185549	0.0073626
615	0.0324452	0.0128388
620	0.056227	0.0185549
625	0.0937729	0.0324452
630	0.1436743	0.056227
635	0.2123853	0.0937729
640	0.3331003	0.1436743
645	0.493278	0.2123853
650	0.6586787	0.3331003
655	0.8960376	0.493278
660	0.9793963	0.6586787
665	0.7510982	0.8960376
670	0.339365	0.9793963
675	0.1267948	0.7510982
680	0.0549806	0.339365
685	0.0293222	0.1267948
690	0.0124515	0.0549806
695	0.0035273	0.0293222
700	0	0.0124515
705	0	0.0035273
710	0	0
715	0	0
720	0	0
725	0	0
730	0	0
735	0	0
740	0	0
745	0	0
750	0	0
755	0	0
760	0	0
765	0	0
770	0	0
775	0	0
780	0	0

Table 15. LEDS in LED Bin number 10 with their corresponding Spectral Power Distribution.

Wavelength (nm)	**35**	**36**	**37**
380	0.0023599	0.0023599	0.0023599
385	0.0023599	0.0023599	0.0023599
390	0.0023599	0.0023599	0.0023599
395	0.0023599	0.0023599	0.0023599

400	0.0023599	0.0023599	0.0023599
405	0.0023599	0.0023599	0.0023599
410	0.0023599	0.0023599	0.0023599
415	0.0023599	0.0023599	0.0023599
420	0.0023599	0.0023599	0.0023599
425	0.0023599	0.0023599	0.0023599
430	0.0023599	0.0023599	0.0023599
435	0.0023599	0.0023599	0.0023599
440	0.0023599	0.0023599	0.0023599
445	0.0023599	0.0023599	0.0023599
450	0.0023599	0.0023599	0.0023599
455	0.0023599	0.0023599	0.0023599
460	0.0023599	0.0023599	0.0023599
465	0.0023599	0.0023599	0.0023599
470	0.0023599	0.0023599	0.0023599
475	0.0023599	0.0023599	0.0023599
480	0.0023599	0.0023599	0.0023599
485	0.0023599	0.0023599	0.0023599
490	0.0023599	0.0023599	0.0023599
495	0.0023599	0.0023599	0.0023599
500	0.0023599	0.0023599	0.0023599
505	0.0023599	0.0023599	0.0023599
510	0.0023599	0.0023599	0.0023599
515	0.0023599	0.0023599	0.0023599
520	0.0023599	0.0023599	0.0023599
525	0.0023599	0.0023599	0.0023599
530	0.0023599	0.0023599	0.0023599
535	0.0023599	0.0023599	0.0023599
540	0.0023599	0.0023599	0.0023599
545	0.0023599	0.0023599	0.0023599
550	0.0023599	0.0023599	0.0023599
555	0.0023599	0.0023599	0.0023599
560	0.0023599	0.0023599	0.0023599
565	0.0023599	0.0023599	0.0023599
570	0.0023599	0.0023599	0.0023599
575	0.0023599	0.0023599	0.0023599
580	0.0023599	0.0023599	0.0023599
585	0.0023599	0.0023599	0.0023599
590	0.0023599	0.0023599	0.0023599
595	0.0023599	0.0023599	0.0023599
600	0.0023599	0.0023599	0.0023599
605	0.0023599	0.0023599	0.0023599
610	0.0023599	0.0023599	0.0023599
615	0.0023599	0.0023599	0.0023599
620	0.0023599	0.0023599	0.0023599
625	0.0023599	0.0023599	0.0023599
630	0.0023599	0.0023599	0.0023599
635	0.0023599	0.0023599	0.0023599
640	0.0023599	0.0023599	0.0023599
645	0.0023599	0.0023599	0.0023599
650	0.0029245	0.0023599	0.0023599
655	0.0050138	0.0023599	0.0023599

660	0.0111138	0.0029245	0.0023599
665	0.0210821	0.0050138	0.0023599
670	0.0345587	0.0111138	0.0029245
675	0.0520742	0.0210821	0.0050138
680	0.0771986	0.0345587	0.0111138
685	0.1177057	0.0520742	0.0210821
690	0.1766619	0.0771986	0.0345587
695	0.2558947	0.1177057	0.0520742
700	0.3656166	0.1766619	0.0771986
705	0.4838842	0.2558947	0.1177057
710	0.6037943	0.3656166	0.1766619
715	0.7432528	0.4838842	0.2558947
720	0.892029	0.6037943	0.3656166
725	0.9981564	0.7432528	0.4838842
730	0.9098603	0.892029	0.6037943
735	0.595438	0.9981564	0.7432528
740	0.2968531	0.9098603	0.892029
745	0.1343171	0.595438	0.9981564
750	0.0645258	0.2968531	0.9098603
755	0.0295828	0.1343171	0.595438
760	0.0113171	0.0645258	0.2968531
765	0.0020931	0.0295828	0.1343171
770	0	0.0113171	0.0645258
775	0	0.0020931	0.0295828
780	0	0	0.0113171

Appendix B: Measured Camera Spectral Sensitivity

Table 16. Measured camera spectral sensitivity of the Microline ML50100 monochrome CCD camera.

Wavelength (nm)	Spectral Sensitivity
380	0.853333918614948
385	1.29662658716683
390	1.73524894764762
395	2.16912349468800
400	2.59817272291866
405	3.03779948269668
410	3.48304172472370
415	3.90327459414732
420	4.26787323611512
425	4.57054114448910
430	4.83781440401408
435	5.08831704616194
440	5.34067310240454
445	5.60330178857154
450	5.86530196318914
455	6.11631712177403
460	6.34599075984286
465	6.54265762334080
470	6.71778145704500
475	6.89569925472012
480	7.10074801013080
485	7.36670519029170
490	7.67789773279670
495	7.98448683727931
500	8.23663370337303
505	8.42625753339454
510	8.58881382673957
515	8.73976822866013
520	8.89458638440823
525	9.08528445457952
530	9.29434338688671
535	9.46292600725742
540	9.53219514161930
545	9.51393640479200
550	9.47376718377193
555	9.43359796275186
560	9.41533922592456
565	9.48310632986903

570	9.63540993804254
575	9.79575349495523
580	9.88764044511724
585	9.91736466978264
590	9.94095023060277
595	9.95649584268372
600	9.96210022113158
605	9.93891327115239
610	9.88094701630309
615	9.80559334921601
620	9.73024416252354
625	9.65205539323364
630	9.56231588554565
635	9.46961689287893
640	9.38254966865286
645	9.30661284485098
650	9.23593422874259
655	9.16204883667569
660	9.07649168499830
665	8.96880184606883
670	8.84267725452834
675	8.71089122014884
680	8.58621705270232
685	8.47619058832926
690	8.37245351572992
695	8.26393792351598
700	8.13957590029910
705	7.98106737161216
710	7.79491924310445
715	7.60727407356227
720	7.44427442177194
725	7.31315728711040
730	7.19660090657457
735	7.08390969538074
740	6.96438806874522
745	6.83599497290775
750	6.70391372807163
755	6.56828531039849
760	6.42925069604993

Appendix C: Measured Radiance of the LEDs

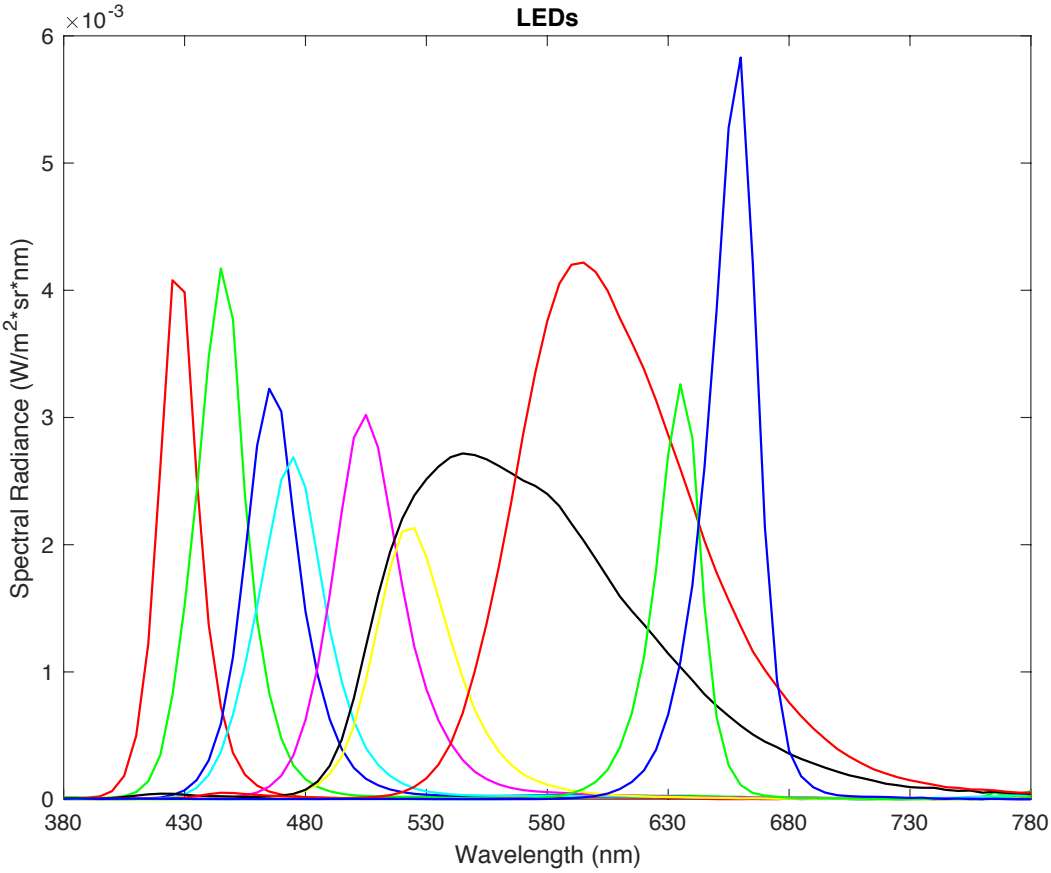

Figure 35. Actual measured radiance values of the LEDs from LEDmotive Technologies.